1-1-2010

Multidisciplinary Design Optimization Of A Helicopter Rotor Blade

Michael G. Leahy
Ryerson University

Multidisciplinary Design Optimization of a Helicopter Rotor Blade

by

Michael G. Leahy

B.Eng Ryerson University, Toronto, 2008

A Thesis

Presented to Ryerson University

In Partial Fulfillment of the

Requirements for the Degree of

Master of Applied Science

In the Program of

Aerospace Engineering

Toronto Ontario, Canada, 2010

Author's Declaration

I hereby declare that I am the sole author of this thesis. I authorize Ryerson University to lend this thesis to other institutions or individuals for the purpose of scholarly research.

Michael Leahy

I further authorize Ryerson University to reproduce this thesis by photocopying or by other means, in total or in part, at the request of other institutions or individuals for the purpose of scholarly research.

Michael Leahy

Multidisciplinary Design Optimization of a Helicopter Rotor Blade

Master of Applied Science
In the Program of
Aerospace Engineering
2010

Michael G. Leahy

School of Graduate Studies
Ryerson University

Abstract

Multidisciplinary design optimization (MDO) was performed on a helicopter rotor blade. The blade was modeled as a rigid flapping blade for dynamics; Blade Element Theory (BET) was the analysis approach to model the aerodynamic loading, and a simple linearly elastic hollowed rectangular section was the main structural component. MATLAB was used to solve the flapping differential equations and its Sequential Quadratic Programming (SQP) and Genetic Algorithm (GA) were used for the optimization. A Particle Swarm Optimization (PSO) routine was also tested. The optimization process consisted of three cases. The first case was a simple cantilever beam under centrifugal and an assumed bending loads. The optimization was performed using the SQP, GA, and PSO algorithms. The SQP resulted in the superior design with 75.45 compared to the GA's 87.1 and the PSO's 79.2, but a local minimum was present. The second case was an expansion of the first case by turning it into multidisciplinary problem. Aerodynamics was included in the design variables and objective function. Only the SQP algorithm was used and there was a reduction in hub vertical shear by 33.6%. The blade mass increased by 36.84%. The last case was an improvement of the second by creating a multiobjective problem by including the hub radial shear and the results were improved significantly by reducing the hub vertical shear by 34.06% and radial shear by 17.87% with a reduction of blade mass by 23.86%.

Acknowledgements

I would like to thank my supervisor Dr. Kamran Behdinan for his support during the process of completing this thesis. Without his guidance this thesis would not have been possible. His enthusiasm for optimization has encouraged me to continue working with optimization tools, and to pursue my Ph.D. I would also like to thank Dr. Il Yong Kim of Queen's University for his advice, and NSERC for their funding support.

I would also like to thank my parents. Their encouragement helped to keep me motivated.

Table of Contents

List of Figures

List of Tables

Nomenclature

α_e	Effective angle of attack	C_T	Thrust Coefficient
α_s	Shaft Angle	α_c	Critical Angle of Attack
θ	Geometric angle of attack	C_H	H-Force Coefficient
θ_{con}	Commanded Pitch Angle	C_Y	Y-Force Coefficient
θ_o θ_{1s} θ_{1c}	Collective, Lateral Cyclic, Longitudinal Cyclic pitch	C_{my}	Pitch Moment Coefficient
β $\dot{\beta}$	Flap Angle, Flap Rate	C_{mx}	Roll Moment Coefficient
β_o β_{1s} β_{1c}	Average, Lateral, Longitudinal Flap	C_W	Weight Coefficient
r	Non-dimensional Radial Location	C_l	2D Lift Coefficient
R	Rotor Radius	C_d	2D Drag Coefficient
N_b	Number of Blades	C_{do}	Zero Lift Coefficient
c	chord	C_P	Power Coefficient
FM	Figure of Merit	C_{Pi}	Induced Power Coefficient
C_{Pp}	Parasite Power	C_{Po}	Profile Power Coefficient
A	Rotor Disk Area or Cross-Section Area	C_{Pc}	Rotor Climb Power
U_T	Tangential Velocity	F_z	Normal Force
U_R	Radial Velocity	F_r	Radial Force
U_P	Perpendicular Velocity	F_x	Inplane Force (Drag force)
U	$\sqrt{{U_P}^2 + {U_T}^2}$	F_c	Centrifugal Force
μ	Advance Ratio	S_z	Vertical Shear
Ω	Angular Velocity	S_r	Radial Shear
I_b	Flap Inertia	$C_{l\alpha}$	Lift Curve Slope
I_R	Autorotation Inertia	ϕ	Induced Angle of Attack
W	Weight	ϕ_S	Shaft Tilt
γ	Lock Number	λ	Induced Inflow Ratio
η	Mode Shape	ψ	Azimuth Angle
ν	Rotating Natural Frequency	e	Hinge Offset
m	Blade Section Mass	σ	Solidity or Stress
z	Blade Deflection	V_∞	Flight speed
L	2D Airfoil Section Lift Force	V_i	Induced Velocity
D	2D Airfoil Section Drag Force or Fuselage Drag Force	T	Rotor Thrust Force
D_{radial}	Section Radial Drag Force	H	Rotor Drag Force
λ_c	Rotor Inflow Due to Climb	Y	Rotor Side Force
λ_o	Uniform Inflow	Q	Rotor Torque
K_x, K_y	Drees Coefficients	C_Q	Rotor Torque Coefficient
f	Fuselage Drag Coefficient	χ	Wake Skew Angle

F	Prandtl Tip Loss Correction Factor	μ_z	Advance Ratio Normal to Disk
K_β	Flap Hinge Spring Stiffness	μ_x	Advance Ratio Parallel to Disk
K_θ	Pitch Control Link Stiffness	β_p	Pre-cone Angle
I_β	Flap Inertia about Hinge	ρ	Free Stream Density or Radial Location or Material Density
E	Young's Modulus	q	Generalized Blade Deflection
I	Area Moment of Inertia	ω	Control Link Natural Frequency
I_f	Total Pitch Moment of Inertia at Hub	M_a	Section Aerodynamic Pitch Moment
I_θ	Section Pitch Moment of Inertia	x_I	Section Centre of Gravity Offset from Feathering Axis
Y_f	Fuselage Side Force	M_{yf}	Fuselage Pitch Moment
C_{yf}	Fuselage Side Force Coefficient	C_{myf}	Fuselage Pitch Moment Coefficient
h	Vertical Distance of Fuselage Centre of Gravity to Hub or Beam Height	M_{xf}	Fuselage Roll Moment
X_{cg}	Longitudinal Distance of Fuselage Centre of Gravity to Hub	C_{mxf}	Fuselage Roll Moment Coefficient
Y_{cg}	Lateral Distance of Fuselage Centre of Gravity to Hub	t_1 t_2	Section Thickness
M_F	Flap Moment	M_L	Lag Moment
I_z	Lag Area Moment Inertia	I_y	Flap Area Moment of Inertia
b	Beam Base	x	Particle Position
c_1, c_2	Cognitive and Social Parameters	H(x)	Penalty Parameter
V_∞	Forward Flight Speed		

Chapter One – Background Theory

1.1. Introduction

The helicopter plays a crucial role in a wide variety of activities such as military, recreation, and medical transport. The rotor of the helicopter has three main functions: the generation of a vertical force (thrust) in opposition to the helicopter's weight, the generation of a horizontal propulsive force for forward flight, and a means of generating forces and moments to control the attitude and position of the helicopter in 3D space (1). Unlike fixed wing aircraft where these functions are separate the helicopter rotor must provide all three functions. Rotor blades are slender, flexible beams. Even in normal operating conditions they may undergo elastic deformations in bending and torsion that can go beyond the limits of linear beam theories. Blade flexibility and related dynamic effects influence not only blade and hub stresses and fatigue life, but also influences the aerodynamic loading on the blade and because of the deformations the blades will substantially modify the effective angle of attack thus changing the aerodynamic loads. The blade structure and aerodynamics are unsteady, even in steady level flight conditions there is an imbalance of aerodynamic loads with air flow velocities ranging from transonic to low speed including stall and reversed flow. Because of these coupled interactions, the helicopter rotor design process is highly multidisciplinary in nature and requires the merging of several disciplines. Conventional design process was controlled by the designer's personal experience and trial and error methods. The purpose of Multidisciplinary Design Optimization (MDO) is to eliminate the trial and error approach to achieve superior designs. The objective of this research is to apply a MDO process to design a rotor blade. Three cases will be performed. The first case will consist of only the structural discipline. The objective of this case will be to minimize the structural mass under an assumed aerodynamic loading and to compare the Sequential Quadratic Programming (SQP), Genetic Algorithm (GA), and Particle Swarm (PS) algorithms. The second case will be a MDO problem by incorporating the aerodynamics and dynamic disciplines. The objective of this case is to reduce the hub vertical shear. The third case is intended to improve the second case by including the hub radial shear into the objective function. The current work is organized into four chapters. The first chapter will give a brief introduction to the helicopter's disciplines including aerodynamics, dynamics, structure and aeroelasticity. The second chapter will describe in detail the mathematical models being used for the optimization process, including a validation against published results. The third chapter is dedicated to the optimization

procedure and results for the three design cases. The fourth chapter will be the conclusion and recommendation.

1.2. Aerodynamics

This section will describe some basic analysis methods such as the blade element theory, each flight regime: hovering and forward flight, and each sub-discipline: wake, induced velocity, and dynamic stall.

1.2.1. Blade Element Theory

The Blade Element Theory (BET) forms the basis of most modern analyses of helicopter rotor aerodynamics because it provides estimates of the radial and azimuthal distribution of the blade aerodynamic loading over the rotor disk. The BET assumes that each blade section acts as a quasi 2D airfoil to produce aerodynamic forces and moments. The loads can be integrated over the rotor to determine rotor performance. The 2D lift and drag coefficient for the airfoil is given by C_l and C_d respectively, and the solidity $\sigma = \frac{N_b c}{\pi R}$ is the ratio between the physical total reference area of the blades and the disk area. The thrust coefficient (1) in hover can be determined from:

$$C_T = \frac{1}{2}\sigma \int_0^1 C_l r^2 dr \tag{1.1}$$

And the power coefficient can be represented by:

$$C_P = \frac{1}{2}\sigma \int_0^1 (\lambda C_l r^2 + C_d r^3) dr \tag{1.2}$$

r is the radial location which has been normalized to 1 at the blade tip. Blade element analysis is only as accurate as the assumptions made about the inflow. More accurate results require the use of vortex theory to take into consideration the conditions at the root tip and root.

1.2.2. Hover

Hover is a unique flight condition. The rotor has zero forward speed and zero vertical speed. Therefore the loading on the rotor is axisymmetric. In hover the rotor must efficiently supply a thrust

force to support the helicopter weight. A helicopter of a given weight should be designed to hover with the minimum power requirements. The hovering thrust efficiency is referred to as the figure of merit. The figure of merit is defined as the ratio of the ideal power to actual power required:

$$FM = \frac{Ideal\ Power\ Required}{Actual\ Power\ Required} < 1 \tag{1.3}$$

The power referred to as the ideal power, is entirely from the induced flow across the rotor disk since viscous effects have not been considered. The equation for induced power coefficient from momentum theory (1):

$$C_p = \frac{{C_T}^{3/2}}{\sqrt{2}} \tag{1.4}$$

The actual power required is the summation of the induced power and profile power assuming zero lift drag C_{do} coefficient is constant.

$$C_p = \frac{\kappa {C_T}^{3/2}}{\sqrt{2}} + \frac{\sigma C_{do}}{8} \tag{1.5}$$

Where κ is the induced power factor. This coefficient is derived from rotor measurements or flight tests and it encompasses a number of nonideal effects, such as nonuniform inflow and tip loss. The induced power factor typically has a value of 1.15 (1). The Figure 1 shows the figure of merit for different loading coefficients for a rectangular blade with no twist.

(Figure 1 next page)

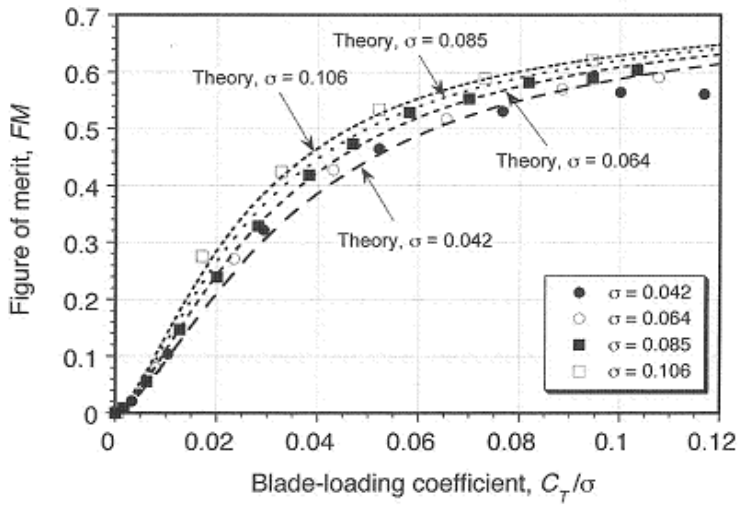

Figure 1 - Measured and predicted figure of merit versus blade loading coefficient for a hovering rotor with different solidities (1) Data source (2)

Higher values of figure of merit require higher loading coefficients. However the maximum values are limited due to flow separation. High loading coefficients demand greater blade section angle of attack and lower solidities. An effective method to improve the figure of merit is to use a blade twist and/or a taper:

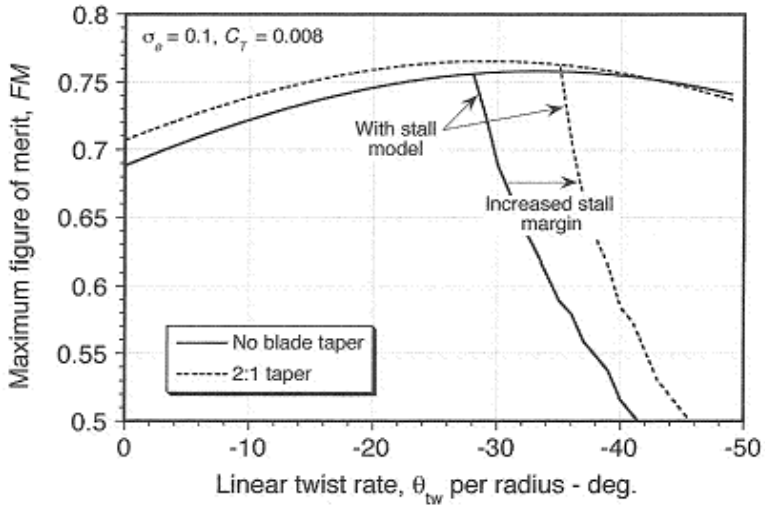

Figure 2 - Effect of blade twist and taper on figure of merit (1)

The figure of merit is plotted above against different values of linear twist and a linear tapered blade. The linear twist for a rectangular blade gives a significant improvement but stall will occur at a smaller linear twist compare to a tapered linearly twisted blade.

1.2.3. Forward Flight

Efficient hover capability is the fundamental characteristic of the helicopter but without good forward flight performance the ability to hover would be of no value (3).Forward flight is defined by the advance ratio:

$$\mu = \frac{V_\infty}{\Omega R} \tag{1.6}$$

It is the ratio of forward flight speed V and the speed of the rotor tip, Ω is the angular velocity and R is the rotor radius. A constant lifting force should be generated during steady level flight, however in forward flight there will be a force and moment imbalance. In Figure 3, ψ is the blade azimuth angle and V is the forward flight speed. The advancing side of the rotating blade moves in the same direction of forward flight. The velocity relative to the blade is larger than the local rotation speed so a sufficient amount of lift can be generated with a small angle of attack. On the retreating side the opposite happens, since the blade is moving away from the forward flight direction the relative velocity is smaller than the blade speed and in order to balance the forces and moments the blade must be at a high angle of attack.

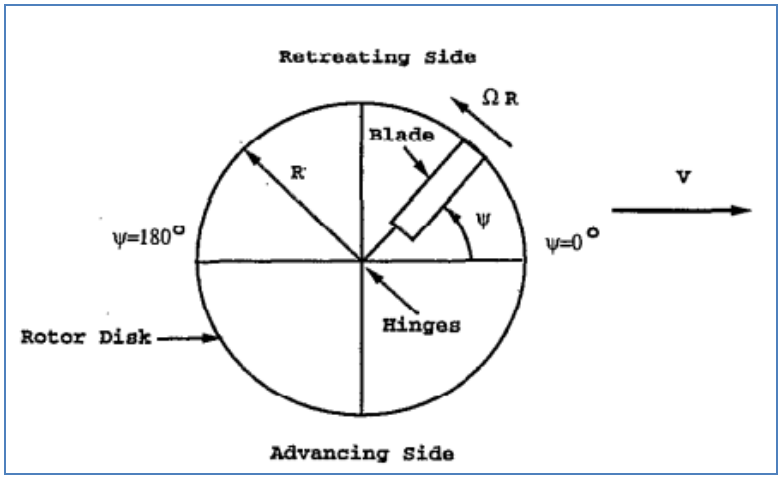

Figure 3 - rotor disk with advancing and retreating sides (4)

In forward flight the rotor blade sees a component of the helicopter forward velocity as well as its own rotation,

$$U_T = \Omega R\left(\frac{r}{R} + V_\infty \sin\psi\right) \tag{1.7}$$

This can also be written in non-dimensional form,

$$\frac{U_T}{\Omega R} = r + \mu \sin \psi \tag{1.8}$$

and r is the radial location normalized to 1 at the blade tip. There will also be a radial velocity component defined as:

$$\frac{U_R}{\Omega R} = \mu \cos \psi \tag{1.9}$$

The radial component has a strong influence on the rotors profile power. More details on forward flight will be presented in the next chapter.

1.2.4.Wake

The helicopter rotor wake is among the most complex fluid dynamic structures being three-dimensional and in many cases unsteady. The wake begins at the blade(s) where the flow can be transonic near the blade tip and undergo compressible dynamic stall. Farther down in the wake, the flow is essentially incompressible. Also, the rotor blades undergo complex unsteady motions because of the necessity to balance moments and they are elastic as well.

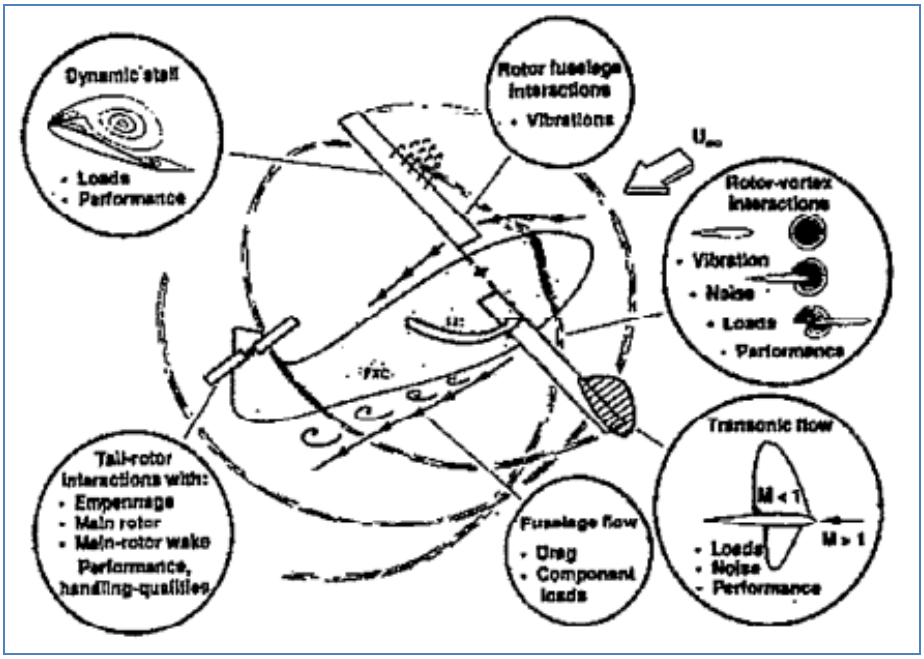

Figure 4 - summary of specific flow problems on the helicopter (4)

The flow near the rotating blade is compressible while the flow in the wake of the helicopter rotor is incompressible because of the reduction in velocity and the flow may also be locally transonic or supersonic on the advancing blade tip and shockwaves may form. On the retreating blade the angle of attack must be larger than on the advancing side and the flow may be stalled and viscous effects are important. Also, as the blade rotates the vortex shed from one of the blades may collide with the following blade; this is known as blade vortex interaction and is a major contributor to noise and vibration. In a rigid wake model, the vortex system position is specified as a function of advance ratio and trust. However this method does not take into account the contraction of the wake as is predicted with momentum theory and thus blade load calculations often disagree significantly with experiment as rotor solidity, thrust level and tip Mach number are increased (5). The prescribed wake model (5), (6) employs experimental data to locate the vortex positions and thus incorporates contraction. This method is computational efficient but it is limited since it cannot be expanded to where there is no experimental data. In the free wake method the vortex system motion is calculated directly from the effects of all the other wake components and the influence on the blade. In this method the wake is allowed to develop in time and initial value. This is the industry standard today (4).

1.2.5.Induced Inflow

BET assumes no mutual influence of adjacent blade element sections and it requires uniform or linear distribution of induced velocity over the blade, however the induced velocity field is highly nonuniform due to the vortical wakes trailed from each blade and the influence of other blades and airframe components. A lifting line method which requires the calculation of induced velocities is required. Prandtl (7) developed the Lifting Line Model for a fixed wing where an entire wing was replaced by one single line called the Lifting Line. It is a relatively simple method that is good for high aspect ratios and a wing with no sweep angle. The lifting line represents a series of bound vortices of varying strength across the wing span.

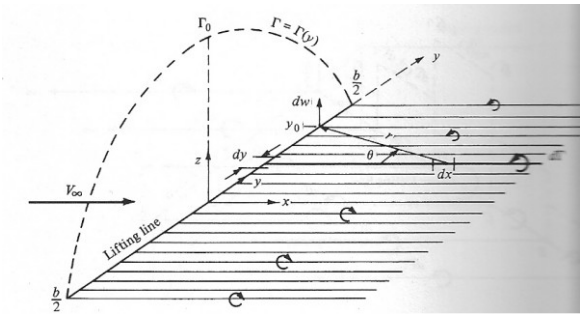

Figure 5 - Superposition of an infinite number of horseshoe vortices along the lifting line (8)

The figure above shows a simple circulation distribution of a fixed wing. Each trailing vortices represents pairs of vortices, each pair associated with a given horseshoe vortex. The trailing vortices have become a continuous vortex sheet trailing downstream of the lifting line parallel to the incoming flow. For a helicopter the wake is convected downward perpendicular to the rotor plane and unlike a fixed wing aircraft the far wake influences the bound vortices. These vortices induce a velocity V_i perpendicular to the blade which creates an induced angle of attack.

$$\lambda = \frac{V_i}{\Omega R} \tag{1.10}$$

The blade flap rate $\dot{\beta}$ due to the asymmetry of the lift also attributes to the induced velocity U_p which is the total velocity perpendicular to the blade surface.

$$\frac{U_p}{\Omega R} = \lambda + r\dot{\beta} + \beta U_R \tag{1.11}$$

The components of the tangential and perpendicular velocities create an induced angle of attack shown in Figure 6. The effective angle of attack is the difference between the geometric and induced angle of attack.

(Figure 6 next page)

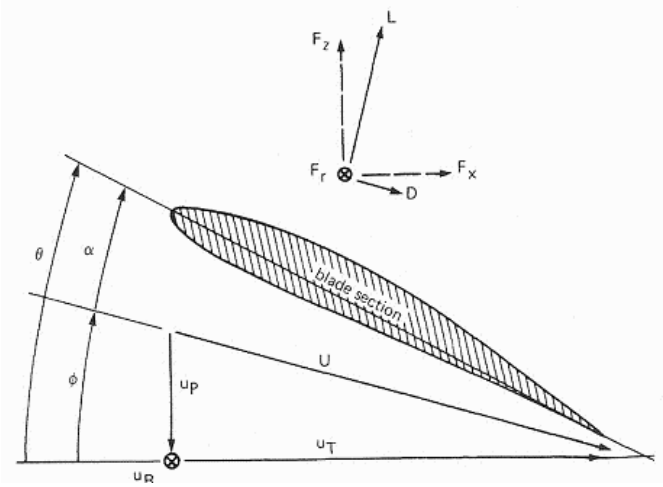

Figure 6 - Blade section aerodynamics (3)

The induced angle ϕ.

$$\phi = \tan^{-1}\frac{U_p}{U_T} \tag{1.12}$$

With the effective angle of attack defined as,

$$\alpha_e = \theta - \phi \tag{1.13}$$

Using a wake model to calculate the induced flow effects are computationally expensive and most models will use a simpler mode such as uniform inflow which is based on momentum theory. This will be discussed in the next chapter.

1.2.6. Dynamic Stall

Dynamic stall limits the performance of a helicopter, which usually occurs at high forward flight speeds or maneuvers with high load factors with the onset of torsional air loads and vibrations (1). The blade that is retreating has very high angles of attack and because of the time varying blade flapping, cyclic pitch control, and wake inflow, the blade stall is more dynamic rather than static. A typical dynamic stall angle and lift coefficient are larger compared to a static case; however there is a significant increase in the drag coefficient which degrade rotor performance. When creating a dynamic normal lift curve there are four modeling considerations to account for, attached flow, leading edge separation,

trailing edge separation, and stall. A typical curve is shown in Figure 7 and is compared to the static lift curve.

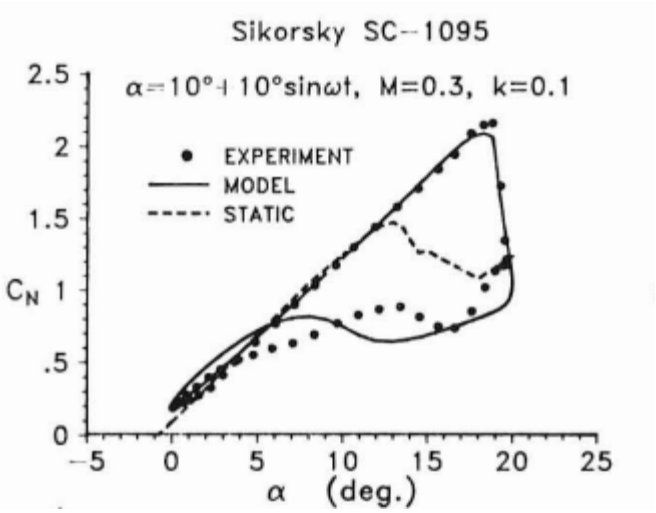

Figure 7 - Dynamic normal force coefficient for the SC-1095 airfoil (9)

1.3. Dynamics

A distinctive feature of helicopter rotors is the articulation in the form of flapping and lead lag hinges that is incorporated at the root of each blade. These may be mechanical hinges or modern rotor hub designs may use semi-rigid or hingeless flexures that allow motion about a virtual hinge location.The hinges allow for independent motion about the hub when experiencing varying aerodynamic loads. Figure 8 defines the degrees of freedom. The pitch angle or feathering angle is crucial for balanceing the forces and moments between the retreating and advancing side. The blade tip lags behind the root due to the high drag and inertial forces of the blade, this angle is refered to as the lag or lead-lag angle. The blade flaps about the root and is in equilibium when the aerodynamic loads are equal to the centrifugal loads, typically this angle is quite small. The loads experienced by the hub are dependant on the hub design. Most helicopters use a fully articulated hub, which means that there are blade hinges to account for lead-lag and flap motion as well as a feathering bearing for pitch. This design is mechincally complicated and heavy, and it also comes with a drag penalty. A hingless rotor design eliminates the hinges in favour of a flexural beam but it still uses a feathering bearing. It is a complicated design since it is not possible to completely isolate falpping motion from lead-lag motion, so there is some coupling to deal with. A hingless-bearingless hub eleminates all hinges and bearings in

favour of a flexural beam. All the motions are obtained by the twisting, bending, and flexing of the hub structure which means high stresses will be present.

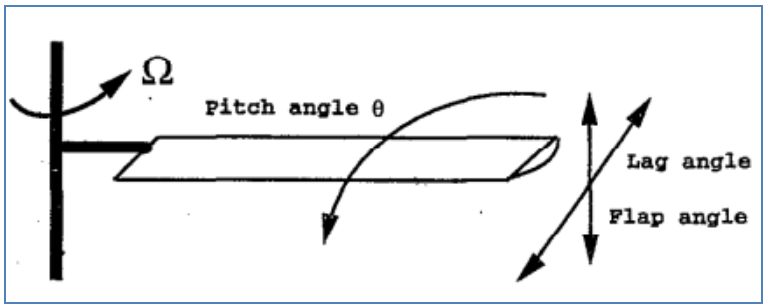

Figure 8 - Defining the pitch, lag, and flap angles (4)

The flap angle β is the degree of freedom out of the rotor plane with the flap angle being positive with vertical motion. The lag angle $\xi$is the motion in the disk plane and is defined as positive in the direction opposite to the rotor rotation. The pitch angle is produced by the rotation of the blade about a hinge or bearing at the root and is defined as positive for nose-up rotation.

For steady state conditions, the behaviour of the blades as it revolves must always be the same at a given azimuth. The blade loads are periodic with period 2π and the rotor blade has a fundamental frequency equal to the rotor speed T=2π/Ω. Periodic functions can be represented as a Fourier series,

$$f = f_o + \sum_{n=1}^{\infty} (f_{nc} \cos n\psi + f_{ns} \sin n\psi) \tag{1.14}$$

and f can represent the flap, lag, and pitch degree of freedom, with n being the harmonic number. Typically higher harmonics (n >1) can be ignored. The Fourier coefficients can be calculated from

$$f_o = \frac{1}{2\pi}\int_0^{2\pi} f\, d\psi,\ f_{nc} = \frac{1}{\pi}\int_0^{2\pi} f \cos n\psi\, d\psi,\ f_{ns} = \frac{1}{\pi}\int_0^{2\pi} f \sin n\psi\, d\psi, \tag{1.15}$$

The degree of freedom f can be described by a differential equation which is solved for periodic motion.

1.3.1.Flapping Motion

Flapping is the motion of the blade centre of mass along the shaft axis. The fundamental resonant frequency of the flapping blade is almost identical to the rotational frequency and with a zero

offset flap hinge the frequency is identical with a phase lag of 90^{o} in the rotor (10). When a hinge offset is used the resonant frequency rises. When a blade flaps down, its vertical velocity adds vectorially to the airflow to increase the angle of attack, providing more lift to oppose flapping. When flapping upwards the opposite occurs with the decrease in lift. Because of the constant flapping motion of the blade, it is self damping and no external dampers are required. Blades with zero rotation speed will droop down towards the ground due to its flexibility, however in rotation the blades will cone upwards and centrifugal stiffening will hold the blades straight. The coning angle β_o is an angle as the result of a balance between aerodynamic and centrifugal loads in hover. In forward flight it is the average part of the flapping motion that is independent of time. The centrifugal loads remain constant for a given rotor speed, the coning angle varies in magnitude around the azimuth due to the asymmetry of the aerodynamic loads. The longitudinal flapping angle β_{1c} represents the amplitude of the pure cosine flapping motion, which is a longitudinal tilt of the rotor tip path plane. The lateral flapping angle β_{1s} represents the amplitude of the pure sine flapping motion, which is a lateral tilt of the rotor tip path plane. Higher harmonics such as β_{2c} and β_{2s} can be ignored for rotor trim and performance evaluation since their values are typically small, however higher harmonics will be important for vibration analyses as well as aeroelastic stability.

1.3.2.Lagging Motion

The rotor not only has flapping motion, but motion in the plane of the disk. An articulated rotor has a lag hinge so the lag motion consists of a rigid body rotation about the hinge axis. The lag angle is the balance of drag and inertial forces about the lag hinge and the only restoring force is due to rotation. When the blade lags on the hinge the centre of mass will become closer to the rotation axis and due to the centrifugal force the centre of mass will want to be at the greatest possible radius and so there will be a restoring force. In an articulated rotor the resonant frequency is proportional to the square root of the stiffness, where the stiffness is the centrifugal force (10). The only aerodynamic damping is due to the changes in profile drag and is quite small, so a mechanical damper will often be required.

1.3.2.1. Ground Resonance

Ground resonance is a dynamic instability involving the coupling of the lag motion with the in plane motion of the rotor hub. The degrees of freedom in ground resonance are the cyclic rotor lag modes which produce a shift of the net rotor centre of mass.

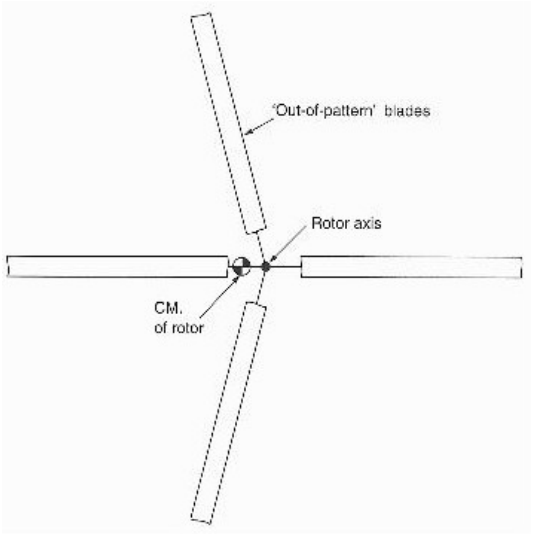

Figure 9 - Out of pattern blades shift centre of mass (CM) of the rotor (10)

This instability is characterized by a resonance of the frequency of the rotor lag motion (specifically the low frequency lag mode in the nonrotating frame) and a natural frequency of the structure supporting the rotor (3). Instability is possible at resonance if the rotating lag frequency is below 1/rev, such as for articulated rotors. The rotor aerodynamic forces have little influence on ground resonance, compared to the structural and inertial forces. Damping of the rotor and supports is either mechanical or structural.

1.3.3.Pitch Motion

In order to achieve a desired flight condition the rotor controls are adjusted to eliminate the moments about the hub while maintaining enough thrust to overcome the helicopter drag and weight. This is achieved by adjusting the collective and cyclic pitch controls iteratively until all forces and moments are balanced.

$$\theta_{con} = \theta_o + \theta_{1s} \sin\psi + \theta_{1c} \cos\psi \qquad (1.16)$$

The rotor must have a mechanical means of producing collective θ_o and cyclic $\theta_{1s}\theta_{1c}$ pitch changes. A widely used method of providing the blade pitch control is by means of a swashplate. A swashplate is a mechanical device that transmits the pilots control motion in the nonrotating frame to the blade cyclic controls in the rotating frame (3).

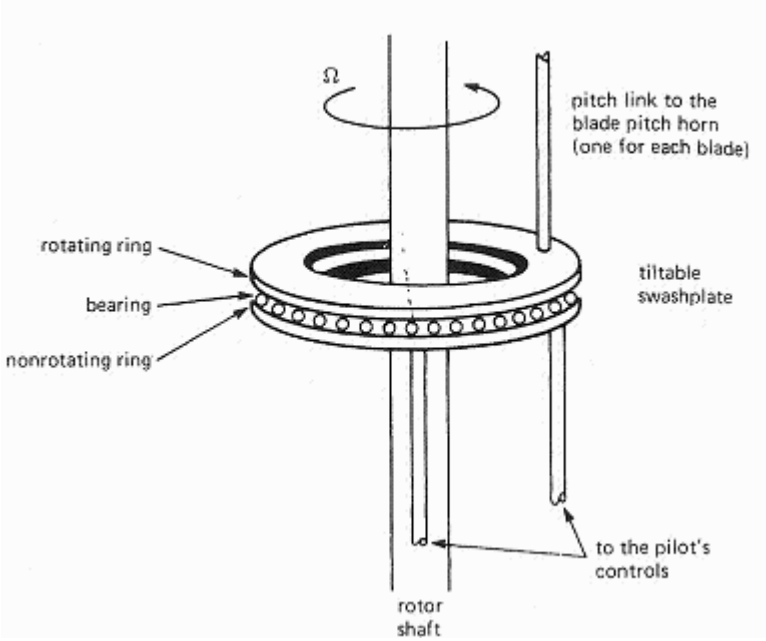

Figure 10 - Schematic of a swashplate (3)

The blade pitch links attach to the rotating ring, and the pilot controls are attached to the fixed frame ring. A vertical displacement of the stationary pilot controls will provide a vertical motion of the pitch links. The collective pitch is changed by moving all of the pitch control arms simultaneously so that all the blades will receive the same amount about their feathering axis. Movement of the cyclic stick in two axes causes the swashplate to tilt in the two axes.

1.4. Structure

The design of a rotary wing structure is similar to that of fixed wing. A typical internal structure of a blade is a box beam or a two cell D-spar design as shown in Figure 11. Fixed wings experience aerodynamic and inertial loads; however a rotating blade experiences both aerodynamic and inertial with centrifugal loads.

(Figure 11 next page)

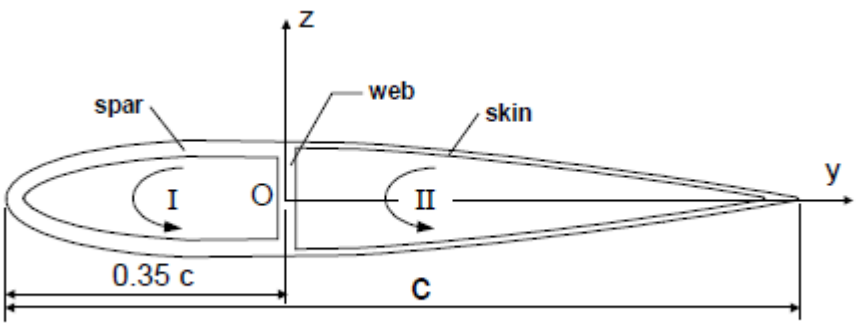

Figure 11 - Schematic of a two celled airfoil section (11)

Early blade designs were constructed out of metal, but fatigue issues required a blade change every few thousand flight hours. Modern blade designs use composite materials for their great fatigue properties which allow for an almost unlimited flight hours. Composite rotor blades are, in general, built-up structures made of different materials for the skin and spar and are normally of closed single- or multi-celled cross-sections and are thin-walled except near the root where they become thick-walled (11). The most important requirements for modeling composite blades are the capability to represent transverse shear deformation, cross-sectional warping, and elastic coupling caused by material anisotropy, in addition to an adequate representation of geometric nonlinearities (12). Another advantage to using the composite materials is the ability to tailor the ply angles and number of layers to reduce vibrations.

1.4.1.Blade Loads

Apart from aerodynamic forces such as lift, drag, and pitch moment, the rotor blades will experience centrifugal and Coriolis forces. Let's consider a blade lagging in a rotating reference frame in the figure below. When the rotating frame appears to rotate at the same angular velocity as the blade, the rotation disappears and so the component cannot be accelerating due to the rotation. The centripetal forces due to the rotation given by:

$$F_c = m\Omega^2 r \tag{1.17}$$

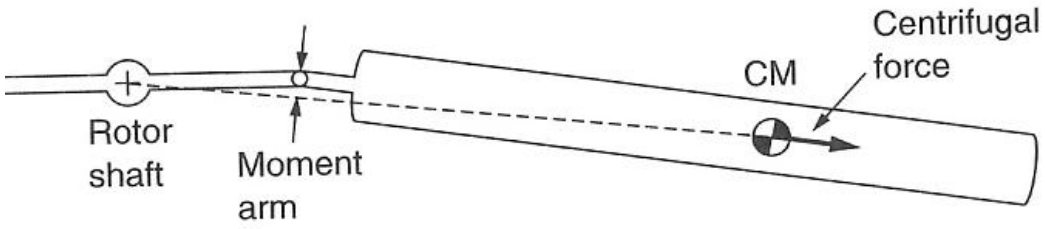

Figure 12 - Lagging blade with hinge offset (10)

A rotating body is not in equilibrium in an inertia frame of reference since there is no force to balance the centripetal force. A new virtual force is the centrifugal force which is equal in magnitude but opposite in direction. When a blade flaps or lags the centre of mass of a segment along the blade will move towards the rotation axis which will reduce its moment of inertia. Conservation of momentum requires that the reduced moment of inertia be balanced by an increase in angular velocity, therefore the blade will accelerate in the direction of rotation as the blade flaps. In the rotating frame of reference it appears that the blade is accelerating. A new force referred to as the Coriolis forces is imagined to act to explain why the blades accelerate.

1.5. Aeroelasticity

The basic problem in rotary-wing aeroelasticity is the coupled flap lag torsion of an isolated blade, which is inherently nonlinear because of the geometric nonlinearities associated with moderate (or large) deflections that must be incorporated into the structural, inertia, and aerodynamic terms associated with the aeroelastic problem (12).Coupling between bending out of plane motions (flap) and bending in plane motions (lag) and torsion is critical, and neglecting one of these degrees of freedom may result in poor results. An important aspect of rotary-wing aeroelasticity is the coupling between the trim state and the aeroelastic problem. This requires the simultaneous solution of the trim and aeroelastic problems. In addition, rotor blades have a large span to chord ratio and so significant stresses can be communicated to the hub if the blades are not permitted to flap and bend. Blades aeroelastic effects play a major role in determining helicopter performance (3).Rotor blades with swept tips, which imply both sweep and anhedral of the blade tip, experience bending-torsion and bending-axial coupling effects. Swept tips influence blade dynamics because they are located at regions of high dynamic pressure and relatively large elastic displacements. Swept tips enhance rotor performance and are effective for reducing aerodynamic noise and blade vibrations (11). Another important aeroelastic problem is the coupled rotor fuselage interaction. This is known as an aeromechanical problem.

Aeromechanical instability in helicopters occurs because of coupling between the rotor and fuselage motion. Ground and air resonance are aeromechanical problems that are caused by the interaction of lagging motion of the rotor blades with other modes of helicopter motion (pitch and roll) (13).

1.6. Trim

The purpose of trim is to find the correct aircraft controls and attitudes in order to obtain a desired steady state flight condition. Trimming a rotorcraft is more complicated than a fixed wing aircraft since it has aerodynamic components that rotate and with load asymmetry in forward flight. There are two types of trim conditions: wind tunnel and propulsive trim. Wind tunnel trim requires the elimination of the pitch and roll moments of the rotor while maintaining a specified thrust coefficient. In propulsive trim the equilibrium equations (Chapter 2) of a helicopter in steady flight are solved to balance the forces and moments. Typically the moments are taken about the hub of the helicopter. An example of a simple trim procedure is presented below:

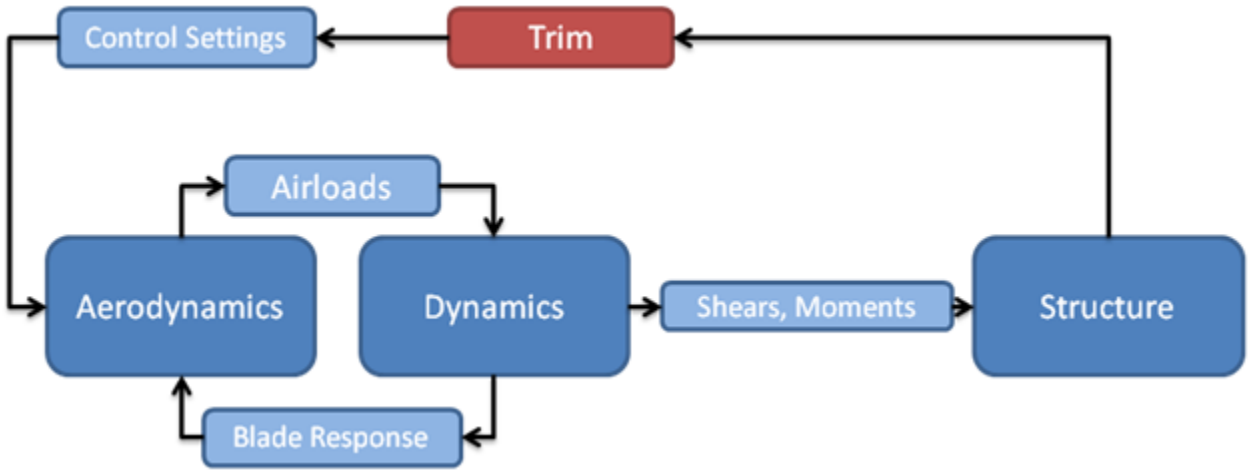

Figure 13 - Trim Procedure

The trim process begins with an initial control setting. These control inputs are then used to perform the aerodynamic and dynamic analysis. The airloads are calculated and then passed to the dynamics where the blade response is determined from the equations of motion. This is repeated until a periodic solution is obtained. Once it is obtained the shears and moments are calculated for the equilibrium equations. The process is repeated until the equilibrium equations are reduced to their target value of zero.

Chapter Two - Rotor Model

2.1. Motivation of Research

The multidisciplinary nature of the helicopter rotor blade design process involves several disciplines such as aerodynamics, dynamics, and structures. This makes it an excellent engineering problem to use Multidisciplinary Design Optimization (MDO) approach to achieve a superior design. The author's main motivation is to work with MDO, however learning more about the complex nature of the helicopter is great opportunity to learn more about aerodynamics, dynamics, and structural design. With regards to the MDO the author's interests are with optimization algorithms, specifically evolutionary. Gradient based algorithms are great for their speed compared to evolutionary, but they typically find themselves in a local minimum for nonconvex problems. For large complicated engineering problems with many disciplines the problem will never be convex. Also gradient based algorithms have been in use for decades and there is probably little room for improvement. Evolutionary algorithms such as the Particle Swarm (PS) are relatively new and advances are possible. Also to the author's knowledge no PS optimization routine has been used for helicopter optimization. A multidisciplinary helicopter optimization posed a challenge; it was a good opportunity to advance the author's knowledge of rotorcraft and MDO architecture.

2.2. Development

This section will describe in detail what equations are being used for each discipline. Most of the equations mentioned will be from ref (3). This book describes in detail several different analysis techniques for helicopter performance. Everything from aerodynamics, dynamics and aeroelasticity are included with varying degrees of fidelity. It is an excellent book and is highly recommended to anyone who wishes to learn more about rotorcraft.

2.2.1. Aerodynamic Model

The aerodynamic model which includes aerodynamic forces, the inflow, and the airfoil performance will be presented in the current section.

2.2.1.1. Aerodynamic Forces

The lift and drag of an airfoil section (3) can be represented respectively by:

$$L = \frac{1}{2}\rho U^2 c C_l \; and \; D = \frac{1}{2}\rho U^2 c C_d \tag{2.1}$$

C_l and C_d are the two dimensional lift and drag coefficient respectively and U is the velocity. The lift is perpendicular to the chord c and the drag is parallel. For the analysis it is required that the loads be expressed normal and in plane. The normal force (3) can be express as:

$$\frac{F_z}{c} = \frac{1}{2}U^2(C_l \cos\phi - C_d \sin\phi) \tag{2.2}$$

And the in plane drag force is:

$$\frac{F_x}{c} = \frac{1}{2}U^2(C_l \sin\phi + C_d \cos\phi) \tag{2.3}$$

ϕ was defined on page 9. Dimensionless quantities are being used so both sides of the equation were divided by chord and the density ρ was omitted. There are several simplifying assumptions that can be made, small angles $\cos\phi \cong 1$, $\sin\phi \cong \phi$ and $\phi = {U_p}/{U_T}$, it is also possible to assume that the lift coefficient is much smaller than the drag. Therefore the above equation for normal force reduces to:

$$\frac{F_z}{c} = \frac{1}{2}C_{la}({U_T}^2\theta - U_p U_T) \tag{2.4}$$

and the in plane force becomes:

$$\frac{F_x}{c} = \frac{1}{2}\left(\left(U_p U_T\theta - {U_p}^2\right) + \frac{C_d}{C_{la}}{U_T}^2\right) \tag{2.5}$$

The radial force which is important for rotor performance is shown below:

$$F_r = -\beta F_z + D_{radial} \tag{2.6}$$

The first term is the radial component of normal force when the blade flaps up and the second term is the radial drag force due to the component of radial flow along the blade. Using the previously mentioned assumptions and ignoring the radial flow the equation is:

$$\frac{F_r}{c} = -\beta \frac{F_z}{c} \tag{2.7}$$

The thrust T is normal to the rotor disk, the rotor drag force H is in the disk plane positive aft, the rotor Y force (side force) (3) is in the disk plane positive in the lateral direction towards the advancing side. There is also a torque Q.

$$T = N_b \int_0^R F_z \, dr \tag{2.8}$$

$$H = N_b \int_0^R (F_x \sin\psi + F_r \cos\psi) dr \tag{2.9}$$

$$Y = N_b \int_0^R (-F_x \cos\psi + F_r \sin\psi) dr \tag{2.10}$$

$$Q = N_b \int_0^R r F_x \, dr \tag{2.11}$$

With $N_b$being the number of blades. The rotor forces are obtained by integrating the blade section along the span. In dimensionless form, the thrust coefficient can be written as:

$$C_T = \frac{T}{\rho \pi R^2 (\Omega R)^2} \tag{2.12}$$

The same calculation can by done for the H and Y forces but the torque must be represented as:

$$C_Q = \frac{Q}{\rho \pi R^2 (\Omega R)^2 R} \tag{2.13}$$

The complete equations in dimensionless form that have been used for the present work are presented below (3):

$$\frac{C_T}{\sigma} = \int_0^1 \frac{F_z}{c} dr \tag{2.14}$$

$$\frac{C_H}{\sigma} = \int_0^1 \frac{F_x}{c} \sin\psi + \frac{F_r}{c} \cos\psi \, dr \tag{2.15}$$

$$\frac{C_Y}{\sigma} = \int_0^1 -\frac{F_x}{c} \cos\psi + \frac{F_r}{c} \sin\psi \, dr \tag{2.16}$$

$$\frac{C_Q}{\sigma} = \int_0^1 r \frac{F_x}{c} dr \tag{2.17}$$

The moments on the rotor hub may be obtained in a similar fashion. The pitch moment M_y and the roll moment M_x (3) are respectively:

$$M_y = -N_b \int_0^R \cos\psi \, r F_z \, dr \tag{2.18}$$

$$M_x = N_b \int_0^R \sin\psi \, r F_z \, dr \tag{2.19}$$

Then in coefficient form:

$$\frac{C_{My}}{\sigma} = -\int_0^1 \cos\psi \frac{F_z}{c} dr \tag{2.20}$$

$$\frac{C_{Mx}}{\sigma} = \int_0^1 \sin\psi \frac{F_z}{c} dr \tag{2.21}$$

These equations will be crucial for determining the equilibrium position of the rotor. Before these equations can be used with equilibrium equations it is necessary to take the average values using the operator:

$$F = \frac{1}{2\pi}\int_0^{2\pi} f d\psi \tag{2.22}$$

f represents the coefficients from above. The power required (3) of the rotor can be separated into four equations.

$$C_p = C_{pi} + C_{po} + C_{pp} + C_{pc} \tag{2.23}$$

C_{pi} is the induced power coefficient:

$$C_{pi} = \int_0^1 \lambda_i \sigma \frac{F_z}{c} dr \tag{2.24}$$

The profile power C_{po} is defined without radial flow effects:

$$C_{po} = \int_0^1 \frac{\sigma C_d}{2} U^3 \, dr \tag{2.25}$$

The parasite power C_{pp} is obtained from the drag characteristics of the fuselage

$$C_{pp} = 0.5\mu^3 \frac{f}{A} \tag{2.26}$$

The rotor climb power which is required to increase altitude:

$$C_{pc} = \lambda_c C_T \tag{2.27}$$

λ_c is the inflow ratio due to a climb velocity with a flight path angle:

$$\lambda_c = \frac{V_\infty}{\Omega R} sin\theta_{FP} \tag{2.28}$$

For the present work the profile power equation mentioned previously was replaced by the more complete profile power which includes the effects of radial flow. The radial drag force increases the rotor profile drag coefficient by 50% (3).

$$C_{po} = \int_0^1 \frac{\sigma C_d}{2} ({U_t}^2 + {U_R}^2)^{1.5} dr \tag{2.29}$$

The next section will describe the inflow model that is being implemented.

2.2.1.2. Inflow Model

The inflow model which is commonly used for optimization routines and testing of new aerodynamic models is Drees linear inflow model (14). Inflow significantly affects the rotors performance and being able to model it accurately is very important. The first representation of a linear inflow model was developed by Glauert (15).

$$\lambda_i = \lambda_o (1 + K_x r cos\psi) \tag{2.30}$$

This equation only approximates the longitudinal inflow. A variation of Glauert's result is to consider both the longitudinal and lateral variation of inflow:

$$\lambda = \lambda_o (1 + K_x r cos\psi + K_y r sin\psi) \tag{2.31}$$

The coefficients K_x and K_y are weighting factors which represent the deviation from the mean inflow. K_x is the slope of the longitudinal inflow and K_y represents the lateral slope for the inflow. The mean inflow is from the uniform inflow model (1) given by:

$$\lambda_o = \mu tan\alpha + \frac{C_T}{2\sqrt{\mu^2 + \lambda_o}} \tag{2.32}$$

This equation is dependent on the inflow λ_o which means it must be solved numerically. Using a simple fixed point iteration scheme, it converges very rapidly.

The coefficients proposed by Drees are dependent on the wake skew angle χ given as:

$$\chi = \tan^{-1}\left(\frac{\mu_x}{\mu_z + \lambda_o}\right) \tag{2.33}$$

The μ_x and μ_z terms are the advance ratio parallel and perpendicular to the rotor plane respectively. The wake skew angle as a function of advance ratio and different values of thrust are shown below.

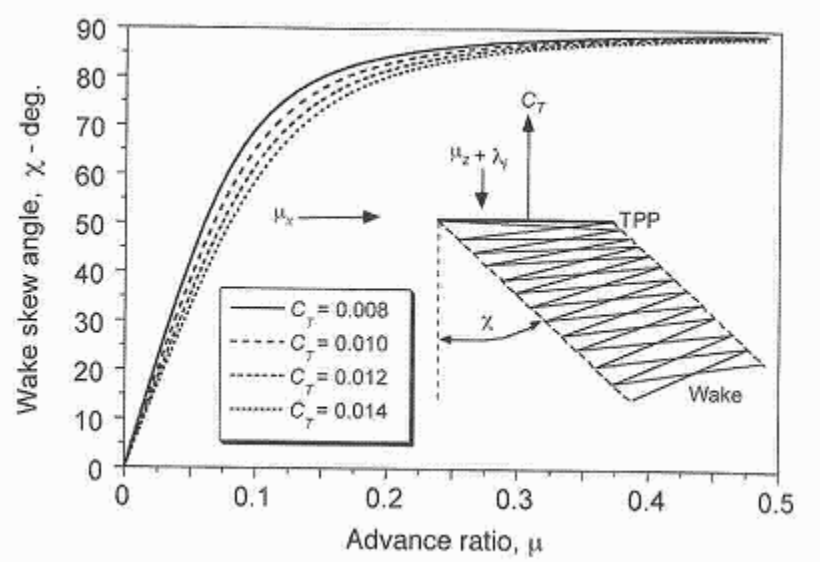

Figure 14 - Typical variation in rotor wake skew angle with thrust and advance ratio (1)

For high advance ratios the wake skew angle becomes relatively large. At advance ratios greater than 0.4, the wake almost becomes parallel to the rotor disk. With low advance ratios the skew angle reduces rapidly and the possibility of blade vortex interactions is very high.The values for the Drees coefficient are given as:

$$K_x = \frac{4}{3}\left(\frac{1 - cos\chi - 1.8\mu^2}{sin\chi}\right), \qquad K_y = -2\mu \tag{2.34}$$

The advantage of Drees model is its relative accuracy and ease of implementation. Vortex models generally give a more accurate result but are computationally expensive. In hover the advance ratio is zero and the Drees coefficients are also set to zero. The uniform inflow model reduces to

$$\lambda_o = \sqrt{\frac{C_T}{2}} \tag{2.35}$$

However the uniform inflow model for hover is good for analytical solutions and it does not take into account the nonlinear inflow and tip loss effects. An inflow model (1) which does represent nonlinear and tip loss is given by:

$$\lambda = \frac{\sigma C_{la}}{16F}\left(\sqrt{1 + \frac{32F}{\sigma C_{la}}\theta r} - 1\right) \tag{2.36}$$

This inflow model takes into account tip loss by using Prandtl's Tip Loss Correction Factor F:

$$F = \frac{2}{\pi}\cos^{-1}(\exp(-f)) \tag{2.37}$$

Where f is given in terms of the number of blades and the radial position of the blade element r:

$$f = \frac{N_b}{2}\left(\frac{1 - r}{r\phi}\right) \tag{2.38}$$

The basic effect of F is to increase the induced velocity near the tip to reduce the lift being generated. This effect is plotted in Figure 15.

(Figure 15 next page)

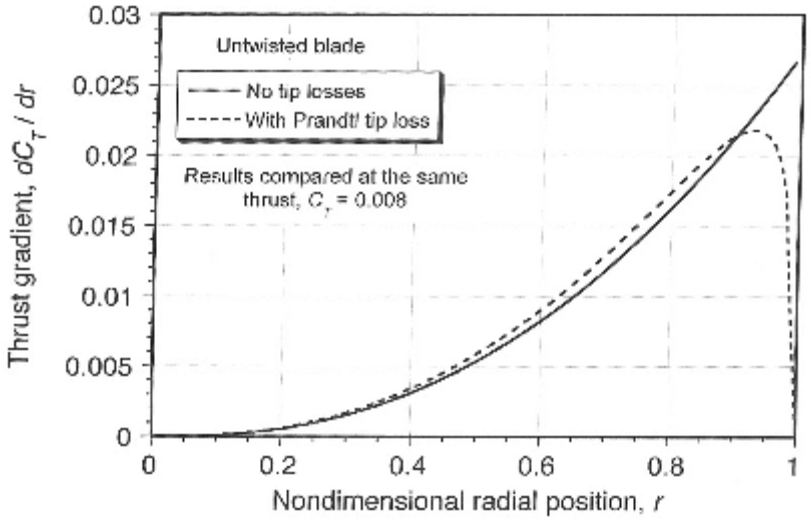

Figure 15 - Spanwise variation of thrust with tip loss effects (1)

Notice the loss of thrust near the tip region. This loss of thrust must be compensated for by increasing the blade pitch to produce the same total rotor thrust. Tip loss can also be extended to the root, however the loss in thrust coefficient is usually small due to the low dynamic pressures. The next section will describe the airfoil section data that has been implemented.

2.2.1.3. SC-1095 Airfoil

The airfoil chosen is one of two airfoils used on the UH-60 helicopter rotor blade (see section 2.4.1). For the current work only the SC-1095 airfoil will be used instead of both the SC-1095 and SC-1094R8. The lift curve slope as a function of Mach number is presented in Figure 16. The lift curve increases steadily up to Mach 0.7, but then rapidly increases to 0.84 due to compressibility. After 0.84 it drops significantly in the transonic regime.

(Figure 16 next page)

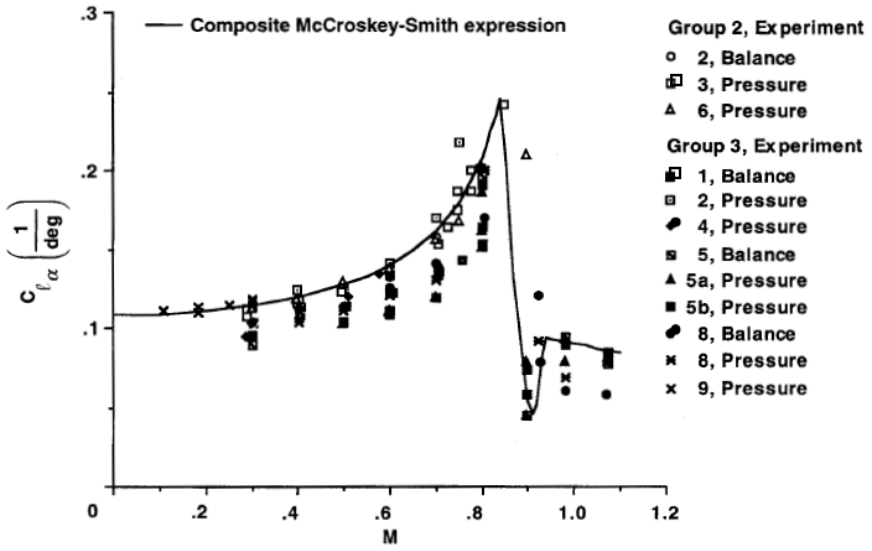

Figure 16 - Lift curve slope vs. Mach number (16)

The McCroskey-Smith expression is a mathematical model derived from experimental data. McCroskey created an expression for the naca0012 airfoil in supersonic flow (17) and Smith for subsonic (18). The expressions taken from ref (16) are presented below.

$$C_{l\alpha} = \begin{cases} C_{l\alpha_0}\left[G + \frac{t/c}{1+t/c}\left[G(G-1) + 0.25(\Gamma+1)(G^2+1)^2\right]\right] & M \le 0.84 \\ C_{l\alpha_{0.84}} - \frac{dC_{l\alpha}}{dM}(M - 0.84) & 0.84 < M \le 0.93 \\ 0.055\left((\Gamma+1)M^2\, t/c\right)^{-1/3} & 0.93 < M < 1.1 \end{cases} \quad (2.39)$$

And the constants are defined as:

$$G = \frac{1}{\sqrt{1-M^2}}, t/c = 0.095, C_{l\alpha_0} = \frac{0.11}{deg},$$

$$\Gamma = 1.4, \frac{dC_{l\alpha}}{dM} = 5.4$$

To incorporate some element of stall into the airfoil model, the following equation was used to approximate static stall characteristic:

$$C_l = \alpha C_{l\alpha} e^{-\left(\frac{\alpha-\alpha_c}{0.1}\right)} \tag{2.40}$$

The above equation is for stall with a positive angle of attack. The negative stall curve is defined as:

$$C_l = \alpha C_{l\alpha} e^{\left(\frac{\alpha+\alpha_c}{0.01}\right)} \tag{2.41}$$

The critical angle of attack α_c was obtained from static wind tunnel data (19). The lift curve for a different mach numbers from ref (19) are presented in the appendix. Unfortunately there is insufficient data for the positive and negative stall so the above equations were arbitrarily chosen.

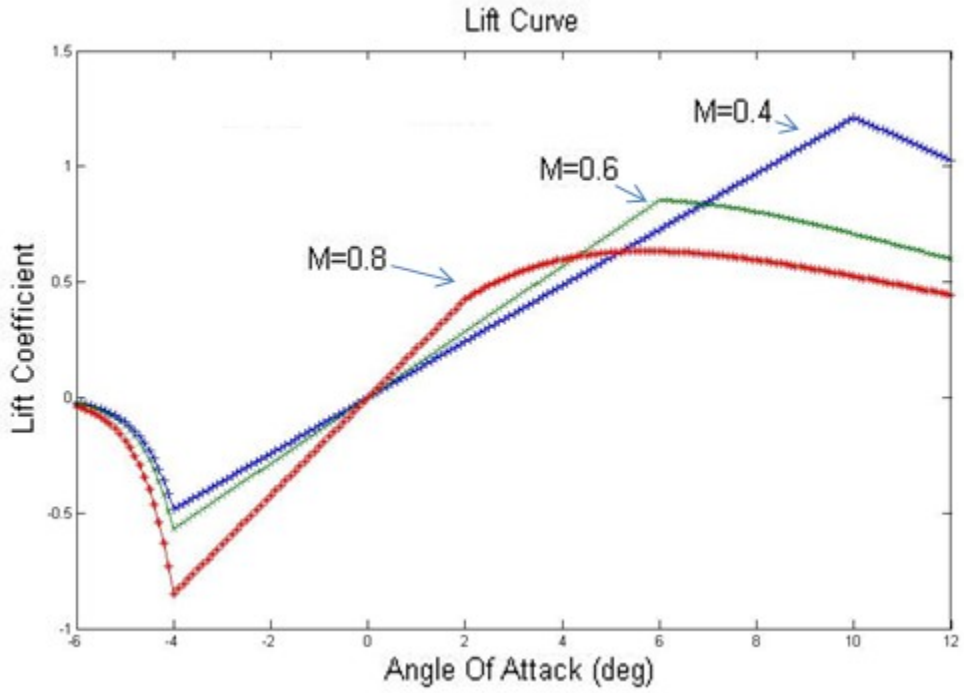

Figure 17 - Lift Coefficient vs. Angle of Attack at three different Mach numbers

On close inspection the static stall plot above resembles the naca0012 normal lift coefficient curve in Figure 18 on the next page. At low mach numbers there is a rapid decrease in lift after the critical angle of attack. For mid range mach numbers (0.4-0.7) the stall characteristic is a more gradual decrease in lift.

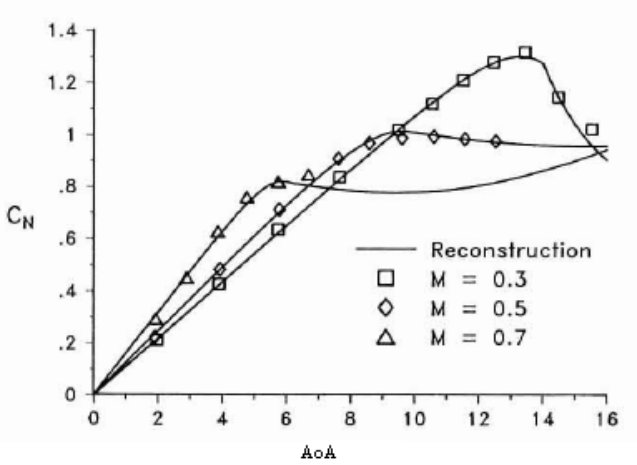

Figure 18 - Normal force coefficient versus angle of attack for different mach numbers (9)

Similar expressions for the zero lift drag coefficient are available from ref (16).

$$C_{d0} = \begin{cases} c_f\left[S_A\frac{L}{c}(1+\frac{c_s}{c_f}+\frac{K[0.01745|\alpha_{ZL}|]^{2.7}}{c_f}\right] & M \le 0.8 \\ C_{d0(0.8)}+\frac{dC_{d0}}{dM}(M-0.8) & 0.84 < M \le 1 \\ C_{d0(<0.8)}+5(t/c)^{5/3}[(\Gamma+1)M^2]^{-1/3} & 1 < M < 1.1 \end{cases} \quad (2.42)$$

With the constants defined as:

$$c_f = \frac{0.455}{[\log(R_{N0}\frac{1}{2}\frac{L}{c}\sqrt{S_A}]^{2.58}} \quad (2.43)$$

$$\alpha_{ZL} = -0.3^o, S_A = 1.14, \frac{L}{c} = 2.022,$$

$$\frac{c_s}{c_f} = 0.02, R_{N0} = 6e^6, K = 2.12$$

The above expressions agree very well with experimental data as shown on the next page.

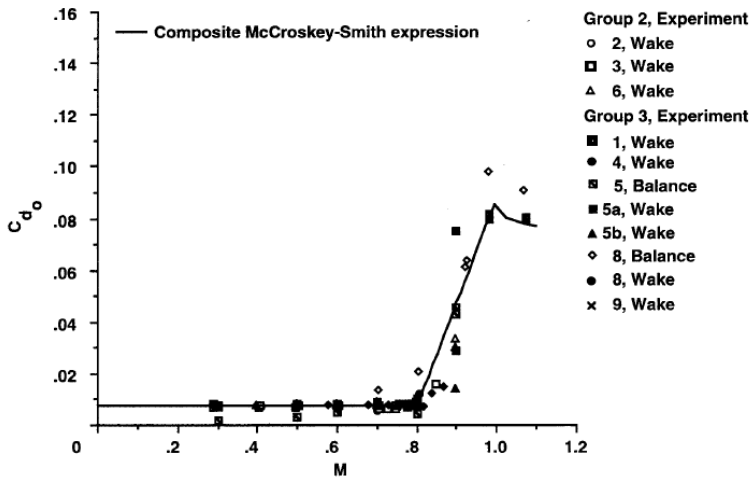

Figure 19 - SC1095 zero lift drag coefficient at different Mach numbers (16)

Up to the drag divergence Mach number of 0.8 the zero lift drag remains constant at approximately 0.008. However after drag divergence there is a rapid increase. This high drag will be located at the blade tip. The next section will go into more detail about the dynamic models that are being implemented.

2.2.2.Dynamic Model

The forces on the rotor blade are dependent on the dynamic motion of the blade and vise versa. From the total induced inflow equation on page 8 this coupling is demonstrated since the inflow is dependent on the flapping characteristics of the blade.

2.2.2.1. Rigid Flapping Blade

This section will describe in detail the rigid blade characteristics. The derivation of the equation of motion is in the rotating frame. Figure 20 on the next page shows a flapping blade with a hinge offset e.

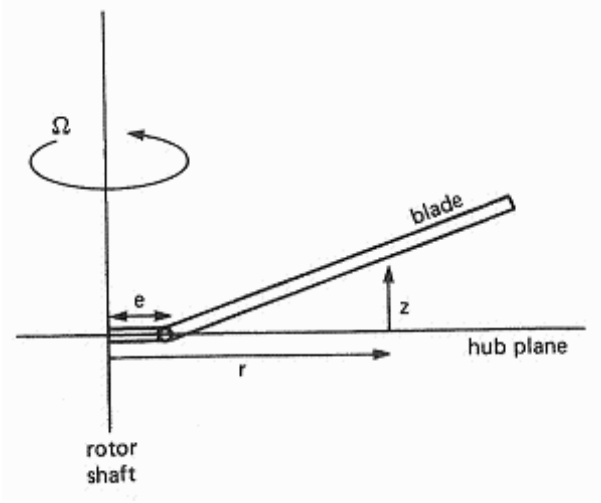

Figure 20 - Flap motion with hinge offset (3)

The out of plane deflection is represented by z at the radial station r. the radial station is measured from the centre of rotation and the vertical deflection is defined as:

$$z = \beta\eta \tag{2.44}$$

Rigid rotation about a hinge offset corresponds to a general mode shape represented as η:

$$\eta = k(r - e) \tag{2.45}$$

The mode shape is in dimensional form but it is convenient to express the dynamics in non-dimensional form. With the non-dimensional constant $k = (1 - e)^{-1}$ the mode shape is now non-dimensionalized to unity at the blade tip. Since we are normalizing the mode to unity at the tip the degree of freedom β is the angle between the disk plane and a line extending to the tip.

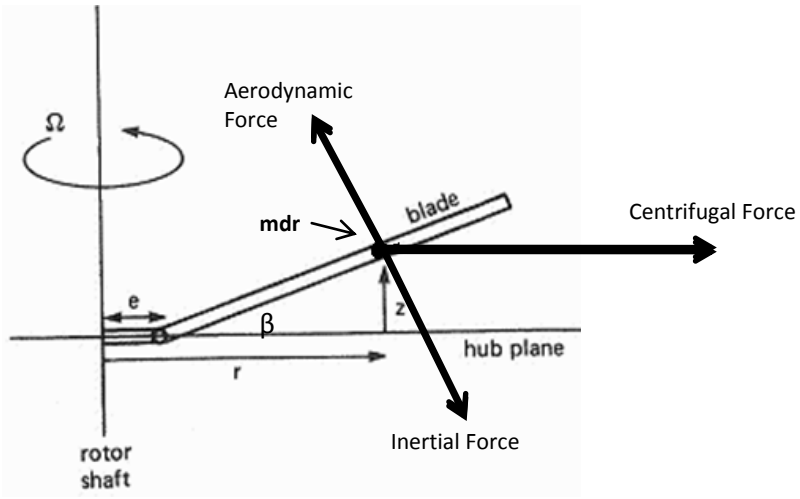

Figure 21 - Equilibrium forces acting on a blade section, modified from ref (3)

The equilibrium forces acting on a blade section comprise aerodynamic, inertial, and centrifugal forces. The aerodynamic force F_z acts perpendicular to the blade surface with a moment arm of (r-e). The inertial force $m\ddot{z}$ opposes the aerodynamic force by acting in the opposite direction. Substituting the expression for z the inertial term now becomes $m\eta\ddot{\beta}$ and has a moment arm of (r-e). The centrifugal force $m\Omega^2 r$ is parallel to the disk plane with moment arm z. There will also be a spring moment at the flap hinge $K_\beta(\beta - \beta_p)$, where β_p is the precone angle of the blade. Blade equilibrium is achieved when the aerodynamic moment balances with centrifugal and inertial moments. The equation in dimensional form with a general mode η is (3):

$$\int_e^R \eta(r-e)mdr\ddot{\beta} + \int_e^R \eta rmdr\beta\Omega^2 + K_\beta(\beta - \beta_p) = \int_e^R (r-e)F_z dr \qquad (2.46)$$

Using dimensionless quantities the equation reduces to:

$$\int_e^1 \eta^2 mdr\ddot{\beta} + k\int_e^1 \eta rmdr\beta\Omega^2 + \frac{K_\beta k}{\Omega^2}(\beta - \beta_p) = \int_e^1 \eta F_z dr \qquad (2.47)$$

After some more manipulation and rearrangement of the above equation it reaches its final form as:

$$I_\beta{}^*\left(\ddot{\beta}+\nu^2\beta\right)=\frac{K_\beta}{I_b\Omega^2(1-e)}\beta_p+\frac{\rho cR^4}{I_b}\int_e^1\eta\frac{F_z}{c}dr \tag{2.48}$$

I_b is the flap moment of inertial about the centre of rotation represented as:

$$I_b=\int_0^R r^2 m dr \tag{2.49}$$

$I_\beta{}^*$ is the ratio of the generalized mass of the flap mode I_β to the flap moment of inertia I_b.

$$I_\beta{}^*=\frac{I_\beta}{I_b} \tag{2.50}$$

With I_β defined as:

$$I_\beta=\int_e^1\eta^2 m dr \tag{2.51}$$

The equations of motion are often written in the form below with the lock number γ:

$$I_\beta{}^*\left(\ddot{\beta}+\nu^2\beta\right)=\frac{K_\beta}{I_b\Omega^2(1-e)}\beta_p+\gamma\int_e^1\eta\frac{F_z}{C_{l\alpha}c}dr \tag{2.52}$$

The lock number is the ratio of aerodynamic to inertial forces:

$$\gamma=\frac{\rho C_{l\alpha}cR^4}{I_b} \tag{2.53}$$

Common values for helicopter blades are between 5 and 16. For the current work the lock number is invalid since it assumes the lift curve slope to be constant in the radial direction. The rotating natural frequency ν with a hinge offset is:

$$\nu^2 = 1 + \frac{e}{1-e}\frac{\int_e^1 \eta m dr}{\int_e^1 \eta^2 m dr} + \frac{K_\beta}{I_\beta \Omega^2 (1-e)} \tag{2.54}$$

The rotating natural frequency for an articulated blade is typically between 1.02 and 1.08, since there is no hinge spring. For hingeless blades values of 1.1 to 1.15 are common. The equation has been non-dimensionalized by dividing both sides by Ω^2. With a hinge offset of zero the rotating natural frequency is 1, which is the resonance condition. For an articulated rotor with no hinge spring, K_β is simply zero.

The pitch and roll moment of the rotor can be expressed using the flapping response. The hub moment for a rotor with a hinge offset can be written in the form (3):

$$M = -(\ddot{\beta} + \beta)\int_e^1 m\eta r dr + \int_e^1 r F_z \tag{2.55}$$

Using the flapping equation and substituting for $\ddot{\beta}$ ref (3) has shown that after some simplification the hub moment reduces to:

$$M = I_b(\nu^2 - 1)\beta \tag{2.56}$$

In an inertial frame with N_b blades the pitch and rolling moments are respectively:

$$\frac{C_{My}}{\sigma} = \frac{-C_{l\alpha}(\nu^2 - 1)}{2\gamma}\beta_{1c} \tag{2.57}$$

$$\frac{C_{Mx}}{\sigma} = \frac{C_{l\alpha}(\nu^2 - 1)}{2\gamma}\beta_{1s} \tag{2.58}$$

The equations in this section are for a rigid flap motion only. The flexible blade motion will be described in the next section.

2.2.2.2. Flexible Flapping Blade

The highly complex and unsteady aerodynamic environment in which rotor blades operate causes significant elastic blade motion. The elastic blade motion, in turn, changes the aerodynamic and structural loading along the blade (20). The equations of motion are derived considering the equilibrium of aerodynamic, inertial, and centrifugal forces at a radial station r. The blade deflection is now a function of radial location z(r). The forces acting at radial station ρ have a moment arm about the radial station r.

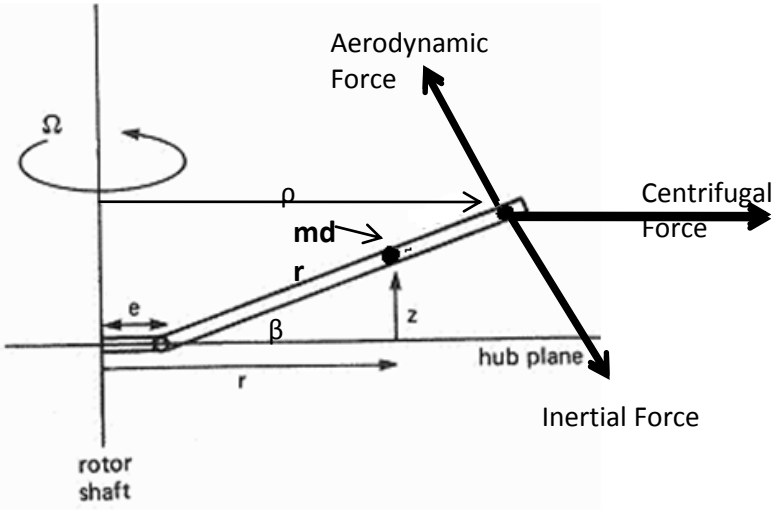

Figure 22 - Equilibrium forces acting on a flexible blade section, modified from ref (3)

The inertial $m\ddot{z}(\rho)$ and aerodynamic force has a moment arm of (ρ-r) about radial station r. The centrifugal force $m\Omega^2\rho$ has a moment arm z(ρ)-z(r). The moment about the radial section r is defined as (3):

$$M(r) = \int_r^R \left[(F_z - m\ddot{z})(\rho - r) - m\Omega^2\rho\big(z(\rho) - z(r)\big)\right]d\rho \qquad (2.59)$$

From engineering beam theory this is related to the beam curvature:

$$M(r) = EI\frac{d^2z}{dr^2} \qquad (2.60)$$

EI is the bending stiffness of the blade, E is the modulus of elasticity and I is the second area moment of the blade cross-section. Combining the above two equations yields the equilibrium equation about radial station r:

$$EI\frac{d^2z}{dr^2}+\int_r^R m\Omega^2\rho\big(z(\rho)-z(r)\big)d\rho+\int_r^R m\ddot{z}(\rho-r)d\rho=\int_r^R F_z(\rho-r)d\rho \tag{2.61}$$

The second derivative of the equation will give the out of plane deflection:

$$\frac{d^2}{dr^2}EI\frac{d^2z}{dr^2}-\frac{d}{dr}\left[\int_r^K m\Omega^2\rho d\rho\frac{dz}{dr}\right]+m\ddot{z}=F_z \tag{2.62}$$

The boundary conditions for an articulated rotor are zero moment and shear at the blade tip and since an articulated blade has a hinge at the root there will be zero displacement and moment at the root. The partial differential equation will be solved by separation of variables which will lead to an ordinary differential equation (3). It will be expanded by a series of normal mode shapes representing beam deflection. The bending deflection z is expanded as a series in the rotating natural mode shapes (3):

$$z(r,t)=\sum_{k=1}^{\infty}\eta_k(r)\,q_k(t) \tag{2.63}$$

q_k represents the angle from the hub plane made by a line from the centre of rotation to the tip of the kth mode. Substituting this expression into the partial differential equation yields:

$$\sum_k\left\{\left(\frac{d^2}{dr^2}EI\frac{d^2\eta_k}{dr^2}\right)-\frac{d}{dr}\left[\int_r^K m\Omega^2\rho d\rho\frac{d\eta_k}{dr}\right]\right\}q_k+\sum_k m\,\eta_k\ddot{q}_k=F_z \tag{2.64}$$

In a vacuum the aerodynamic forcing term in the partial differential equation is set to zero and with a substitution for z being $z=\eta_k e^{ivt}$ (since we are expecting an oscillatory motion with frequency ν), the equation becomes:

$$\nu_k m\eta_k = \frac{d^2}{dr^2} EI \frac{d^2\eta_k}{dr^2} - \frac{d}{dr}\left[\int_r^K m\Omega^2 \rho d\rho \frac{d\eta_k}{dr}\right] \tag{2.65}$$

ν_k and η_k represent the rotating natural frequency and mode shape of the kth mode. Rearranging the differential equation:

$$\sum_{k=1}^{\infty} m\eta_k(\ddot{q_k} + \nu^2{}_k q_k) = F_z \tag{2.66}$$

Operating on the equation with $\int_0^K (\ldots)\,\eta_k dr$ and transforming into dimensionless form

$$I_{q_k}{}^*(\ddot{q_k} + \nu^2{}_k q_k) = \frac{\rho c R^4}{I_b}\int_0^1 \eta_k \frac{F_z}{c} dr \tag{2.67}$$

And $I_{q_k}{}^*$ is given by:

$$I_{q_k}{}^* = \frac{\int_0^K \eta_k{}^2 m dr}{I_b} \tag{2.68}$$

The above differential equation is for the kth bending mode with a rotating natural frequency of

$$\nu^2{}_k = \frac{K_\beta[\frac{d\eta_k}{dr}(e)]^2 + \int_0^R [EI\frac{d^2\eta_k}{dr^2}^2 + \int_r^R m\Omega^2\rho d\rho \frac{d\eta_k}{dr}^2]dr}{\int_0^R \eta_k{}^2 m dr} \tag{2.69}$$

To determine the dimensionless frequency it is necessary to divide by Ω^2. The mode shapes for the present work will be calculated from ANSYS. The first three modes for an articulated blade are presented in the figure below with unit deflection at the tip.

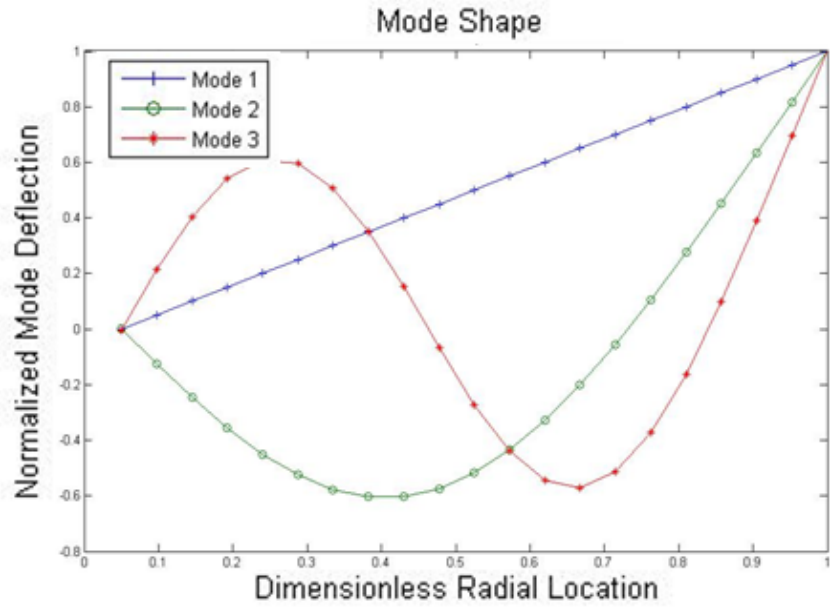

Figure 23 - Mode Shapes for flap with unit deflection at the tip

The first mode shape shows the rigid deflection and the second and third are the elastic modes. Typical rotating natural frequencies for the first elastic flap are between 2.6/rev and 2.8/rev (3), the second elastic flap could be somewhere around 4.8/rev (20).

2.2.2.3. Rigid Flap Rigid Pitch

A blade section with a centre of gravity offset from the pitch axis will experience a coupled pitch-flap motion. The centre of gravity offset will be represented as x_I, which will be positive aft of the pitch axis. A diagram is presented below:

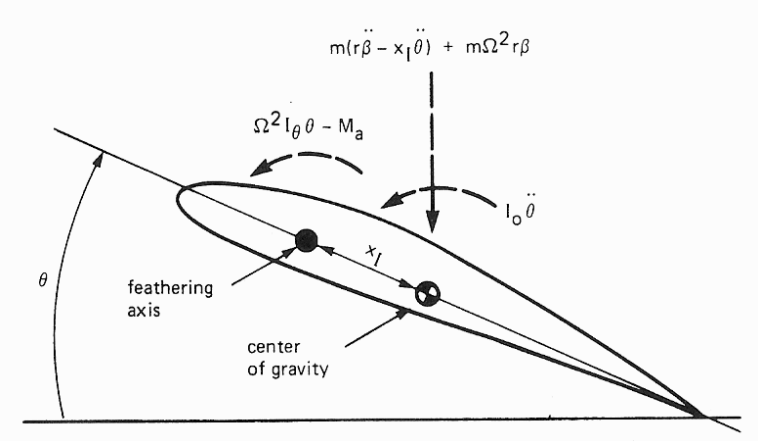

Figure 24 - Blade section pitch moments (3)

The arrows in the diagram represent the positive direction. The equation of motion above is found by the equilibrium of moments about the hinge. For the flapping motion, the inertial force of $m\ddot{z}$ is opposed by the pitching inertial force $mx_l\ddot{\theta}$ about the feathering axis and has a moment arm r. The centrifugal force $\mathrm{m}\Omega^2 r$ acts on the centre of gravity with a moment arm $z - x_l\theta$. The aerodynamic force F_z remains the same with moment arm z. With $z = r\beta$ and a hinge spring the equation of motion is:

$$\int_0^K m(r\ddot{\beta} - x_l\ddot{\theta})rdr + \int_0^K m\Omega^2 r(r\beta - x_l\theta)dr + K_p\beta = \int_0^K rF_z \tag{2.70}$$

The flap natural frequency is the same as the rigid flap only case on page 34. Using dimensionless values and assuming no flapping hinge, the equation reduces to:

$$\left(\ddot{\beta} + \nu^2\beta\right) - I_x^*\left(\ddot{\theta} + \theta\right) = \frac{\rho cR^4}{I_b}\int_0^1 \eta\frac{F_z}{c}dr \tag{2.71}$$

The flap equation is now dependent on the pitch angle and the pitch apparent mass term with the introduction of centrifugal and inertial terms. I_x^* defined as:

$$I_x^* = \frac{\int_0^1 x_l\eta m dr}{I_b} \tag{2.72}$$

The pitch equation of motion is obtained from the equilibrium of moments about the feathering axis. There will be an inertial moment $I_o\ddot{\theta}$ about the centre of gravity and an inertial force $m(\ddot{z} - x_l\ddot{\theta})$ acting on the centre of gravity with a moment arm of x_l. The propeller moment $I_\theta\Omega^2\theta$ about the pitch axis, acts to oppose the pitch motion of the airfoil. With $I_\theta = I_o + x_l{}^2 m$ being the section moment of inertia. The propeller moment occurs when the centrifugal force acting on a mass section which is offset perpendicularly from the pitch axis has a chordwise component. This chordwise component will have a moment arm of $x_l\theta$. The flapping centrifugal force $m\Omega^2 r\beta$ which is normal to the surface will have a moment arm of x_l. There will also be an aerodynamic pitching moment M_a. The equation of motion then becomes:

$$\int_0^R [I_o\ddot{\theta} - (r\ddot{\beta} - x_l\ddot{\theta})x_l m + I_\theta\Omega^2\theta - m\Omega^2 r\beta x_l]dr + K_\theta(\theta - \theta_{con}) = \int_0^R M_a dr \qquad (2.73)$$

K_θ is the stiffness of the control system and θ_{con} was defined on on page 13. The control system has some flexibility and has a restoring moment $K_\theta(\theta - \theta_{con})$. The final equation of motion in dimensionless form:

$$I_f{}^*(\ddot{\theta} + (\omega^2 + 1)\theta - I_x{}^*(\ddot{\beta} + \beta) = \frac{\rho c R^4}{I_b}\int_0^1 \eta\frac{M_a}{c}dr + I_f{}^*\omega^2\theta_{con} \qquad (2.74)$$

The natural frequency $\omega^2$is the ratio of control system stiffness to the total moment of inertia which has also been dived through by Ω^2:

$$\omega^2 = \frac{K_\theta}{I_f\Omega^2} \qquad (2.75)$$

With I_f as the total moment of inertia:

$$I_f = \int_0^R I_\theta dr \qquad (2.76)$$

And $I_f{}^*$ is just the ratio of the pitch moment of inertia to flap inertia:

$$I_f{}^* = \frac{I_f}{I_b} \qquad (2.77)$$

The natural frequency typically has values occurring between 3/rev and 5/rev (3). A stiff control system occurs when $K_\theta \to \infty$ therefore $\theta \to \theta_{con}$. The pitch degree of freedom is now just a control input.

2.2.3.Structure Model

The structure can be modeled in two different methods. The simplest method is to use a general stiffness. With a constant Young's Modulus the area moment of inertia is allowed to vary with no specific structural dimensions. The second approach is to model the cross-section of the section and

calculate its properties such as the area moment, area, and centre of gravity. The material choice was aluminum, and its properties are listed in Table 1.

Table 1 - Material properties

Aluminum 2014-T6	
Young's Modulus	73.1 GPa
Poisson Ratio	0.35
Density	2770 kg/m^3
Yield Limit	416 MPa

2.2.4.Trim Procedure

The trim process is the most computationally intensive part of the current work. The equations of motion are initial value problems which are solved iteratively until a periodic solution is found. The condition for periodicity with period 2π is defined as:

$$f(0) = f(2\pi), \dot{f}(0) = \dot{f}(2\pi) \tag{2.78}$$

Finding the periodic motion is the first step in the trimming process. After determining a periodic state the results are used to calculate the forces and moments required for the helicopter equilibrium equations.

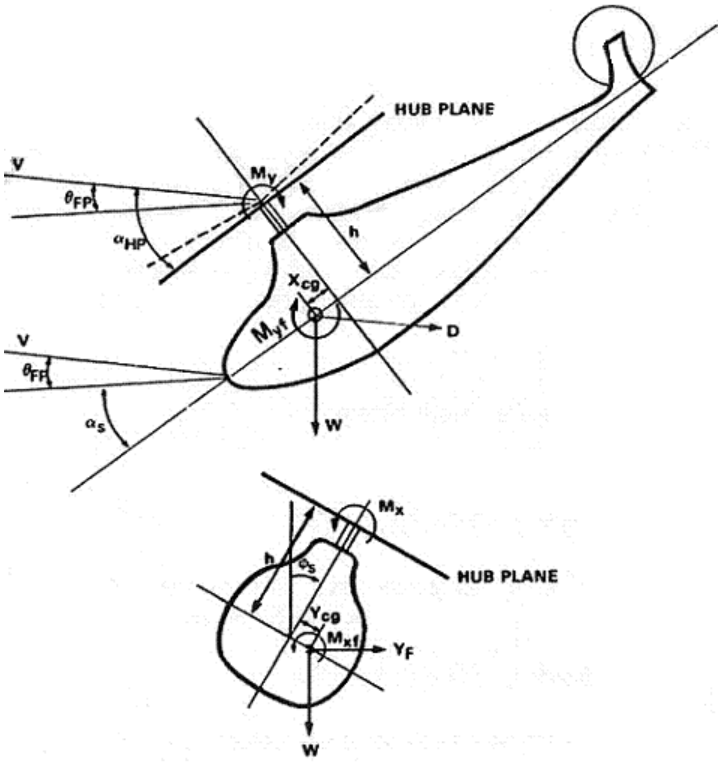

Figure 25 - Free Body Diagram of equilibrium forces and moments (21)

The flight path angle θ_{FP} is the angle of the incoming flow with the horizontal. Some helicopters will have a lateral tilt ϕ_s of the shaft (or roll angle). The angle of attack of the hub plane α is the summation of the flight path angle and the shaft angle of attack α_s.

The vertical force equilibrium is achieved by summing the force components in the vertical direction with positive being downward.

$$W - Tcos(\alpha - \theta_{FP})cos\phi_s + Dsin\theta_{FP} - Hsin(\alpha - \theta_{FP}) + Ysin\phi_s = 0 \qquad (2.79)$$

The thrust must overcome the drag vertical component of the helicopter and the weight. If lateral lilt of the shaft exists the Y force from the rotor will force an increase in thrust. The drag of the fuselage is defined as:

$$D = 0.5\rho {V_\infty}^2 f \qquad (2.80)$$

f is the drag coefficient which is assumed to be equivalent to a flat plate and is determined experimentally (see section on Validation) and V_∞ is the forward flight speed. The equation can also be written in non-dimensional form by dividing the equation by $\rho A(\Omega R)^2$:

$$C_W - C_T cos(\alpha - \theta_{FP}) cos\phi_s + 0.5\mu^2 \bar{f} sin\theta_{FP} - C_H sin(\alpha - \theta_{FP}) + C_Y sin\phi_s = 0 \quad (2.81)$$

The drag force in the non-dimensional form is obtained by substituting the advance ratio equation in for V_∞ and with $\bar{f} = {}^{f}/_{A}$, drag becomes:

$$D = 0.5\mu^2 \bar{f} \quad (2.82)$$

The horizontal or longitudinal force equilibrium equation is:

$$Dcos\theta_{FP} + Hcos(\alpha - \theta_{FP}) - Tsin(\alpha - \theta_{FP}) = 0 \quad (2.83)$$

For steady flight condition the thrust longitudinal component is used for propulsion and must have enough force to equal the drag of the fuselage and the rotor H force in steady flight. In coefficient form the equation is simply:

$$0.5\mu^2 \bar{f} cos\theta_{FP} + C_H cos(\alpha - \theta_{FP}) - C_T sin(\alpha - \theta_{FP}) = 0 \quad (2.84)$$

For the lateral force equilibrium:

$$Y_f + Ycos\phi_s - Tsin\phi_s = 0 \quad (2.85)$$

The trust component with a roll angle must balance with the rotor Y force and the fuselage Y_f side force. Also in coefficient form:

$$C_{Yf} + C_Y cos\phi_s - C_H sin\phi_s = 0 \quad (2.86)$$

The moment equilibrium equations will be summed about the rotor hub; this is easier than trying to find the moments about the helicopter centre of gravity since the hub forces do not need to be separated into components. The pitch equilibrium equation is defined as:

$$M_y + M_{yf} - D(h\cos\alpha + X_{cg}\sin\alpha) - W(X_{cg}\cos\alpha_s - h\sin\alpha_s) = 0 \qquad (2.87)$$

Pitching moment of the rotor M_y and the fuselage M_{yf} must balance with the weight and drag components. The perpendicular distance from the hub plane to the centre of gravity will be represented by h. The longitudinal offset of the centre of gravity is X_{cg} (the positive direction is towards the front of the helicopter). In coefficient form:

$$C_{My} + C_{Myf} - 0.5\mu^2\bar{f}(\bar{h}\cos\alpha + \overline{X_{cg}}\sin\alpha) - C_W(\overline{X_{cg}}\cos\alpha_s - \bar{h}\sin\alpha_s) = 0 \qquad (2.88)$$

$\bar{h}$ and X_{cg} represent values normalized by R.The final equilibrium equation is the roll moment:

$$M_x + M_{xf} + Y_f h\cos\phi_s + Y_f Y_{cg}\sin\phi_s + Wh\sin\phi_s - WY_{cg}\cos\phi_s = 0 \qquad (2.89)$$

The rolling moment of the rotor M_x ,fuselage M_{xf}, with the fuselage side force Y_f components and, with the lateral component of weight must balance with the weight component that acts parallel to the shaft axis. The centre of gravity is offset laterally represented by Y_{cg}. In coefficient form:

$$C_{Mx} + C_{Mxf} + C_{Yf}\bar{h}\cos\phi_s + C_{Yf}\overline{Y_{cg}}\sin\phi_s + C_W\bar{h}\sin\phi_s - C_W\overline{Y_{cg}}\cos\phi_s = 0 \qquad (2.90)$$

The most common method to solve the above equations is to use Jacobian scheme to minimize the error between the value desired by the user and the calculated value. For the equations above the desired value was zero. Using an assumed initial condition for the flight controls $\theta_0, \theta_{1s}, \theta_{1c}$, flight path angle, and induced velocity λ_o the solution iterates until the equilibrium equations are within a specified tolerance. The equilibrium equations presented are for a propulsive trim case. For a wind tunnel trim the equations are simplified. For vertical force equilibrium the thrust must balance with the weight

component, and the pitch and roll moments of only the rotor must be set to zero. Wind tunnel trim is computationally a lot faster. This approach will be used for the optimization procedure.

2.3. Solution Method

MATLAB will be the coding language used for the mathematical model. To solve the flap ordinary differential equation (ODE), an ODE solver is required. MATLAB's ode113 is the selected solver. The ode113 is a variable order Adams-Bashforth-Moulton PECE solver. It may be more efficient than a Runge-Kutta 45 algorithm at stringent tolerances and when the ODE file function is particularly expensive to evaluate. The ode113 is a multistep solver it normally needs the solutions at several preceding time points to compute the current solution (22). The equilibrium equations are solved using MATLAB's fsolve function. This function solves a system of nonlinear equations.

2.4. Validation

For the purpose of validation the results of the author's performance and trim code will be compared to published values of the UH-60 (23). The reason for selecting the UH-60 is due to the widely available published values.

2.4.1. UH-60 Helicopter

The UH-60 Black Hawk is a four-bladed, twin-engine, medium-lift utility helicopter manufactured by Sikorsky Aircraft. The rotor blade consists of two airfoils, the SC1095 and the SC1094 R8, and is divided into three sections.

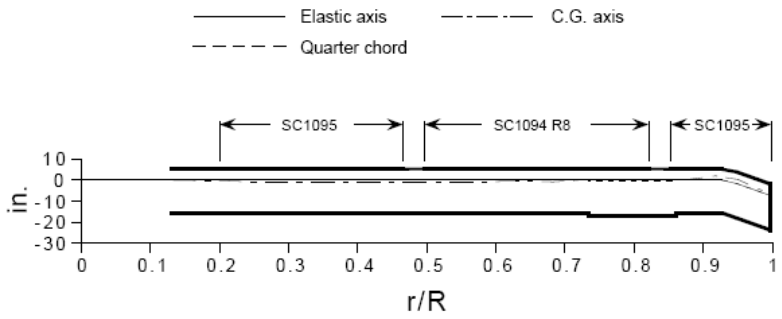

Figure 26 - UH-60 standard blade layout (23)

The standard blade has a swept tip and a nonlinear twist distribution. For the current work only the SC1095 airfoil will be used and the swept tip will be removed to simplify the blade. The centre of gravity

axis is coincident with the elastic and quarter chord axis. The specifications for the rotor and fuselage are presented below.

Table 2 - UH-60 rotor and fuselage specifications (24)

Parameter	Value
Radius	8.18 m
Chord	0.527 m
Solidity	0.0821
Lock	8.1936
Shaft Tilt	3 deg
Rotation Speed	270 rpm
Hinge Offset	0.04659 %Radius
Longitudinal Centre of Gravity (x-dir) wrt Hub	-0.487m
Lateral Centre of Gravity (y-dir) wrt Hub	0
Vertical Centre of Gravity (z-dir) wrt Hub	1.722 m (below hub)

The drag of the helicopter which is based on an equivalent flat plate is defined as:

$$\frac{D}{q}(ft^2) = 35.14 + 0.016(1.66\alpha_s)^2 \tag{2.91}$$

This equation is from ref (23). q is the dynamic pressure in pounds per square foot, and α_s is the pitch attitude of the helicopter. In order to find the nondimensional drag $\bar{f}$, the above equation must be converted to SI units and divided through by the disk area. For small pitch attitudes the drag is approximately $\bar{f} = 0.0155$. The UH-60 incorporates a nonlinear aerodynamic twist of the blade, however a -16deg linear twist is a suitable approximation, as shown in Figure 27. The solid line is the local twist angle taken at the mean chord line of the blade section and the dashed line is a linear best fit to estimate an equivalent linear twist.

(Figure 27 next page)

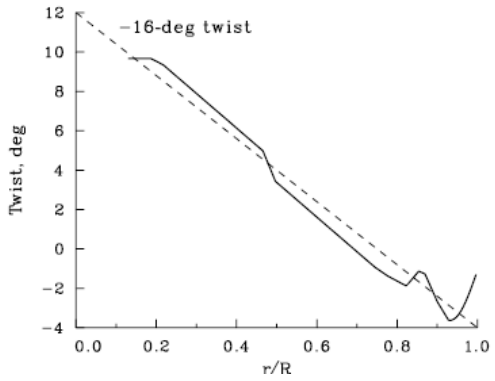

Figure 27 - Aerodynamic twist of the UH-60A blade based on mean chord line (25)

The pitching moment of the fuselage (24)contributes to the trim equations:

$$\frac{M_{yf}}{q}(ft^2) = 2.37925\alpha_s + 728.026\sin(2\alpha_s) + 426.76\sin(\alpha_s)^2 + 348.072\alpha_s - 510.581\cos(\varphi)^3 + 56.11$$

φ is the sideslip angle and will be assumed zero for the current work. Ref (24) describes equations for lift, lateral force, roll, and yawing moments. It will be assumed that no lift from the fuselage will contribute to the equilibrium equations; the zero side slip assumption will reduce the rolling and yawing moment, and lateral force equations to zero.

2.4.2.Results

The results section includes a comparison between rigid and flexible blade loads and response. A validation for a simple trim and hover model will be conducted, and finally the performance and trim results will be compared to the UH-60.

2.4.2.1. Assumptions

There are some key assumptions that need to be stated before going into detail about the results. The first assumption made is that the aerodynamics can be represented by quasi-steady theory with static stall characteristics. Tip loss effects have also been neglected. Reverse flow has been assumed to be minimal with advance ratios less than 0.5 (3). The aerodynamic force equations assume small angles. Also the blade weight has been assumed to be negligible compared to the coriolis forces. For the trim procedure no lateral tilt of the shaft exists and there is no side slip. For dynamics it will be assumed that the control system is rigid and the pitch motion is entirely from the control system.

2.4.2.2. Blade Loads and Response

This section will present the blade loads and response at different flight conditions for both rigid and flexible blades. The blade dimensions are the same as the UH-60. The figure on the next page shows a contour plot of the Mach number for an advance ratio of 0.3.

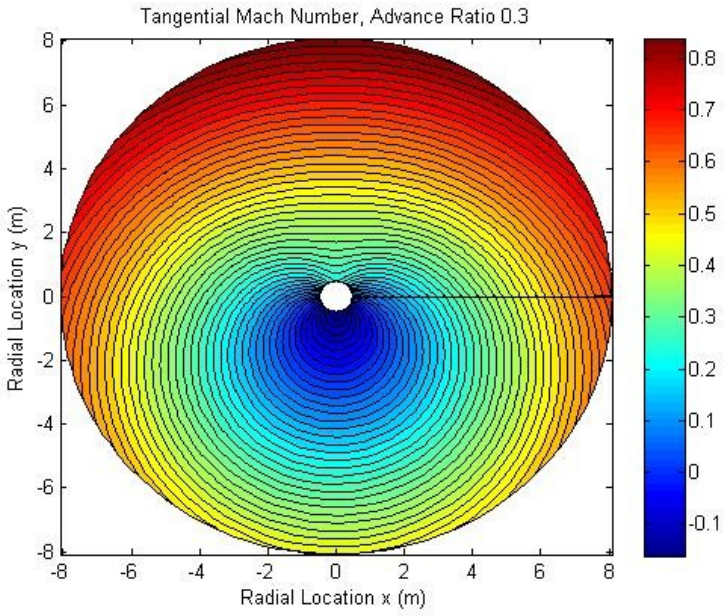

Figure 28 - Mach number contours

The forward velocity is coming from the left side and the blade rotates counter-clockwise. The tangential velocity is greatest on the advancing side which is the upper semicircle of the disk. On the retreating side the velocity reverses close to the blade root. With larger advance ratios the flow reversal will become more severe and the blade tip on the advancing side will approach sonic speed. For the current work the advance ratio will be kept under 0.325.

The aerodynamic and dynamic disciplines are both highly coupled. The blade flap response is dependent on the aerodynamic loading and the loading is dependent on the flapping rate. The flap angles for a rigid blade are plotted for different advance ratios in Figure 29. (Figure 29 next page)

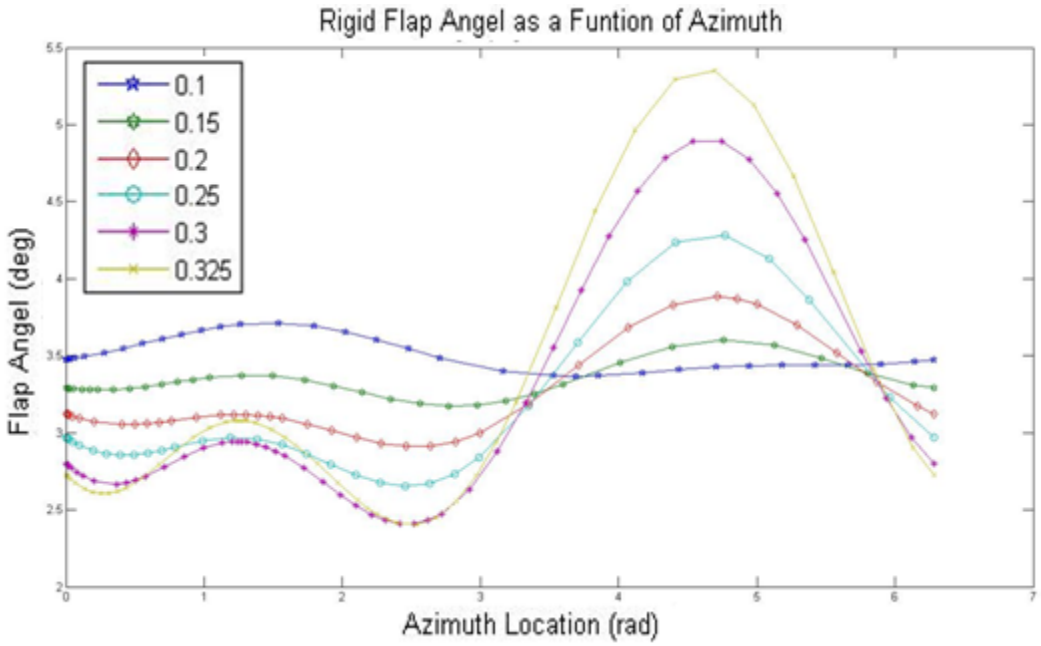

Figure 29 - Flapping Response for different advance ratios

The flap angle is plotted versus the azimuth angle. The flapping response for advance ratios greater than 0.1 demonstrate higher harmonic flapping due to the presence of two peaks a 0.5π and 1.5π. Higher harmonics of blade motion are strongly influenced by nonuniform inflow and elastic blade bending (3). A trimmed helicopter requires a balance of the forces and moments. Up to 0.5π the blade flaps up slightly in order to reduce the lift on the advancing side. At 1.5π there is a very large peak for higher advance ratios caused by the rise in the commanded pitch of the blade to increase the lift. An example plot of the pitch for an advance ratio of 0.325 is show below.

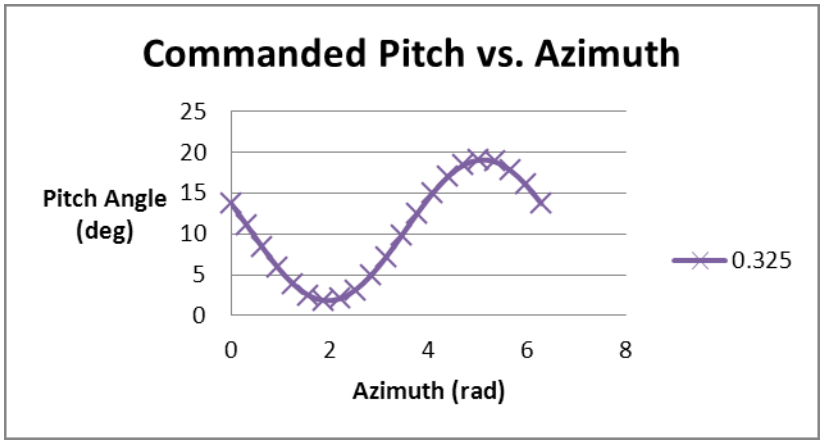

Figure 30 - Commanded pitch angle required to trim rotor at and advance ratio of 0.325

Notice the rapid increase of pitch for the retreating side in order to increase the lift. A comparison between the blade loads and response for both flexible and rigid will now be made. In Figure 31 below, the flexible deflections of the blade are plotted against the radial location at different azimuth angles. At a low advance ratio of 0.1, it is evident that there is little deflection of the blade

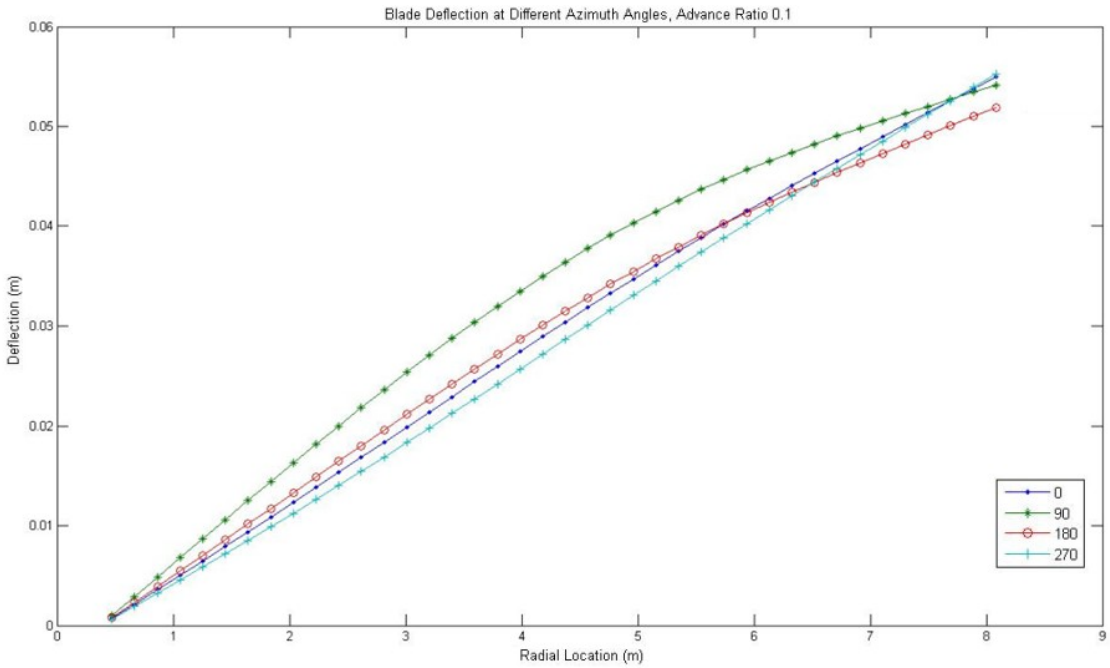

Figure 31 - Blade deflection at different azimuth angles across the span

By comparing the contour plots of both rigid and flexible, there is no significant difference between a flexible blade and rigid. Therefore a rigid blade approximation would be suitable for low advance ratios.

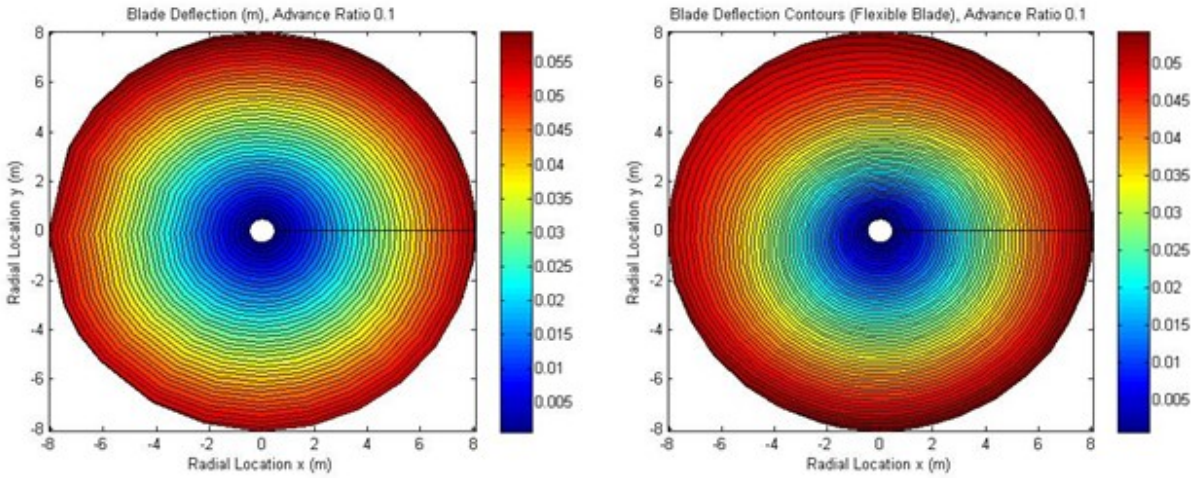

Figure 32 - Defection contours for both rigid and flexible blades at an advance ratio of 0.1

At higher advance ratios the flexible nature of the blade becomes more significant. For an advance ratio of 0.3, in the figure below, there is a considerable bend in the blade on the advancing side.

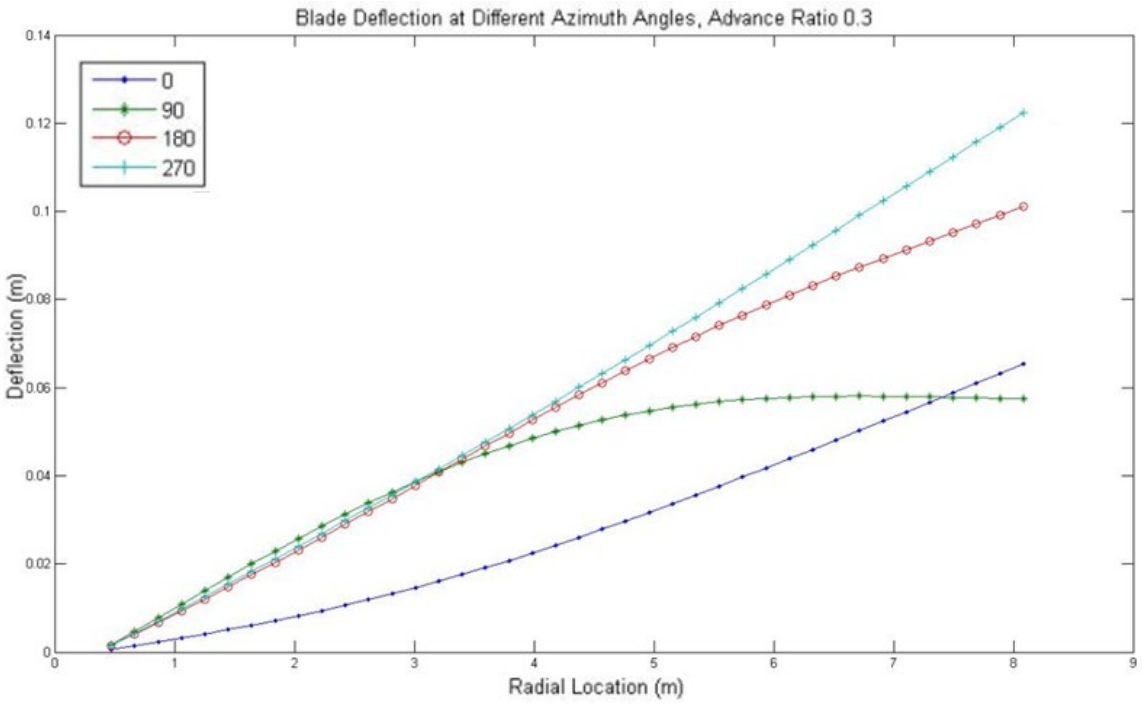

Figure 33 - Blade deflection at different azimuth angles across the span at an advance ratio of 0.3

By comparing the contours in Figure 34 of both the rigid and flexible, it is clear that the blade displacements are considerably different. The flexible blade has a much lower flap deflection than the rigid on the advancing side. Also the deflection peak on the retreating side occurs at approximately 250 deg for the flexible blade compared to the 270 deg for the rigid. This dissimilarity can be explained using the deflection rate in Figure 35.

(Figure 34 and Figure 35 next page)

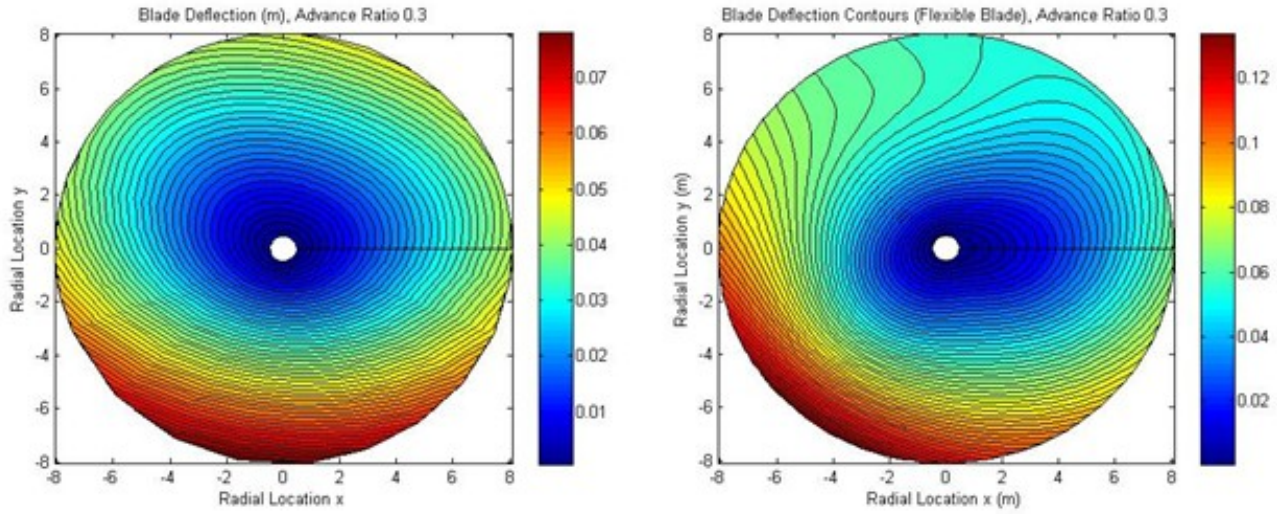

Figure 34 - Blade deflection contours

The deflection rate for the rigid blade is linear in the radial direction; with its maximum value a few degrees after the advancing/retreating threshold. The flexible blade has a nonlinear contour. The deflection rate is greatest at the threshold at the front of the disk. From Figure 33 above, the blade is considerably deformed, this deformation contains high potential energy, which is transformed into kinetic energy at the tip when the blade flexes back to its rigid shape.

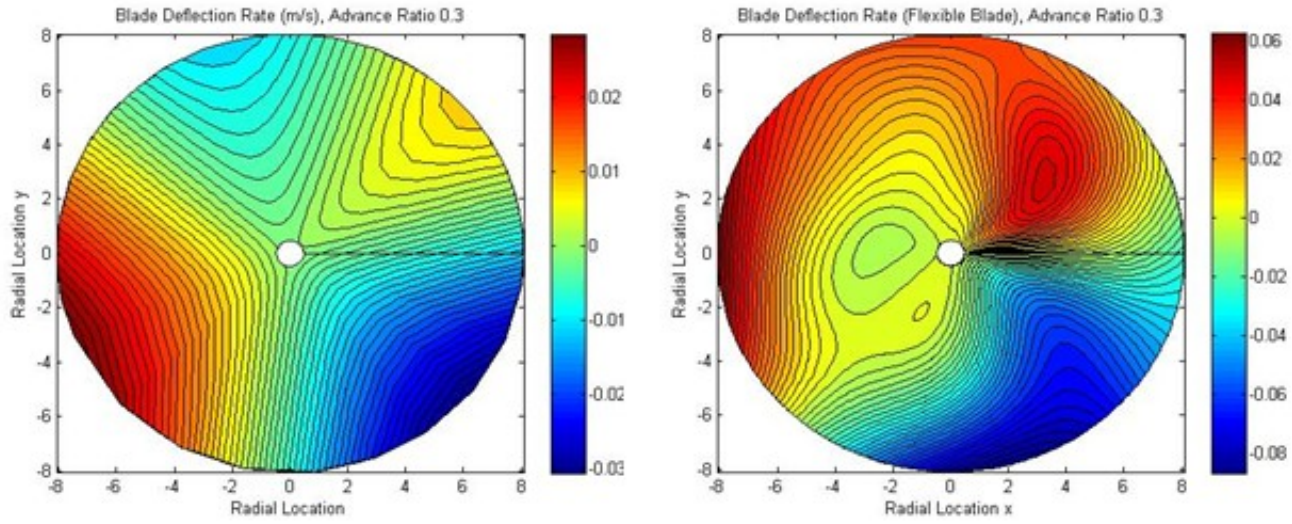

Figure 35 - Blade deflection rate contours

The induced angle of attack is directly related to the flap rate of the blade. For an advance ratio of 0.1 the induced angle of attack in degrees for both flexible and rigid blades are very similar as shown in Figure 36 (next page). The white spot in the centre are values of very high induced angles of attack. With

the induced angle of attack $\phi = {U_p}/{U_T}$ the tangential velocity of the root is very small; this forces ϕ to become very large. For clarity the very high angle are omitted from the plot.

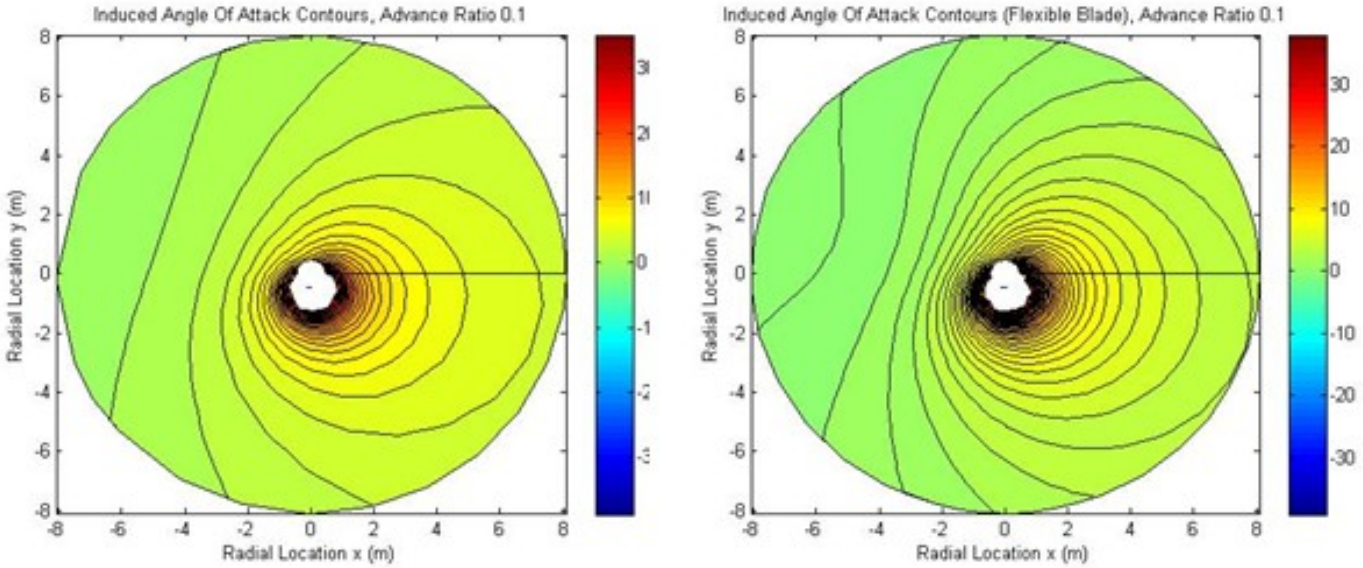

Figure 36 - Induced angle of attack contours for both flexible and rigid blades at an advance ratio of 0.1

At higher advance ratios the difference between rigid and flexible blades becomes more pronounced as shown in Figure 37. The induced angle of attack is greatest for the aft section of the rotor area due to the flapping downward motion. This is more prominent for the flexible blade due to the greater flap rate.

(Figure 37 next page)

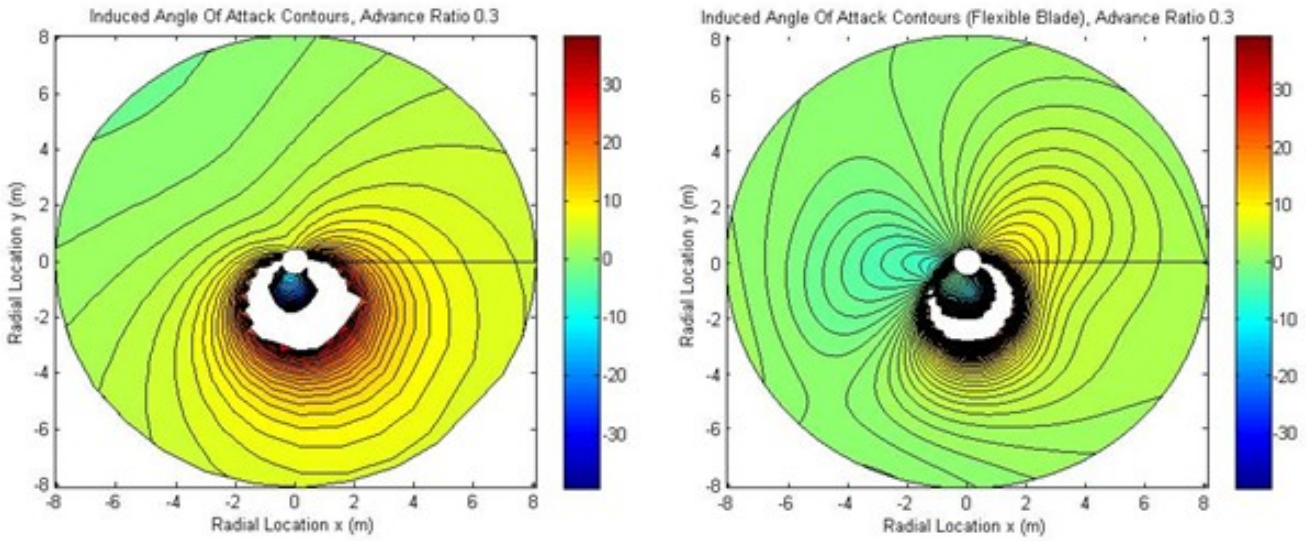

Figure 37 - Induced angle of attack contours for both flexible and rigid blades at an advance ratio of 0.3

In Figure 38 there is a plot of the lift coefficients at three different radial locations (50%, 75%, 99% radial locations). The lift coefficient is greatest at the mid span due to the high geometric angle of attack. The blade tip at 0.5π shows a negative coefficient. This is caused by the pitch control. The pitch angle is lowest on the advancing side to reduce the amount of lift being generated. Also by including a large negative twist the geometric angle of attack at the tip will be reduced even further.

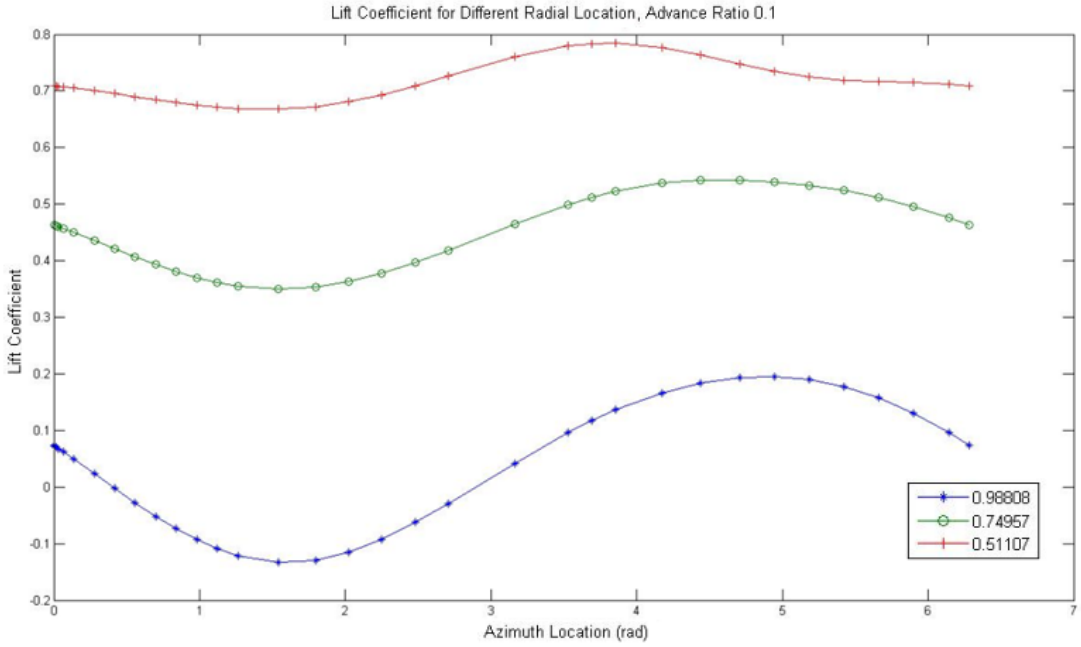

Figure 38 - Lift coefficient for different radial locations at an advance ratio of 0.1 for a rigid blade

At a low advance ratio, the flexibility of the blade in flap does not influence the aerodynamic loads significantly as evident in Figure 39. The loads are reduced slightly on the advancing side blade tip, since the blades will flex more with the higher loading, but the difference is minimal.

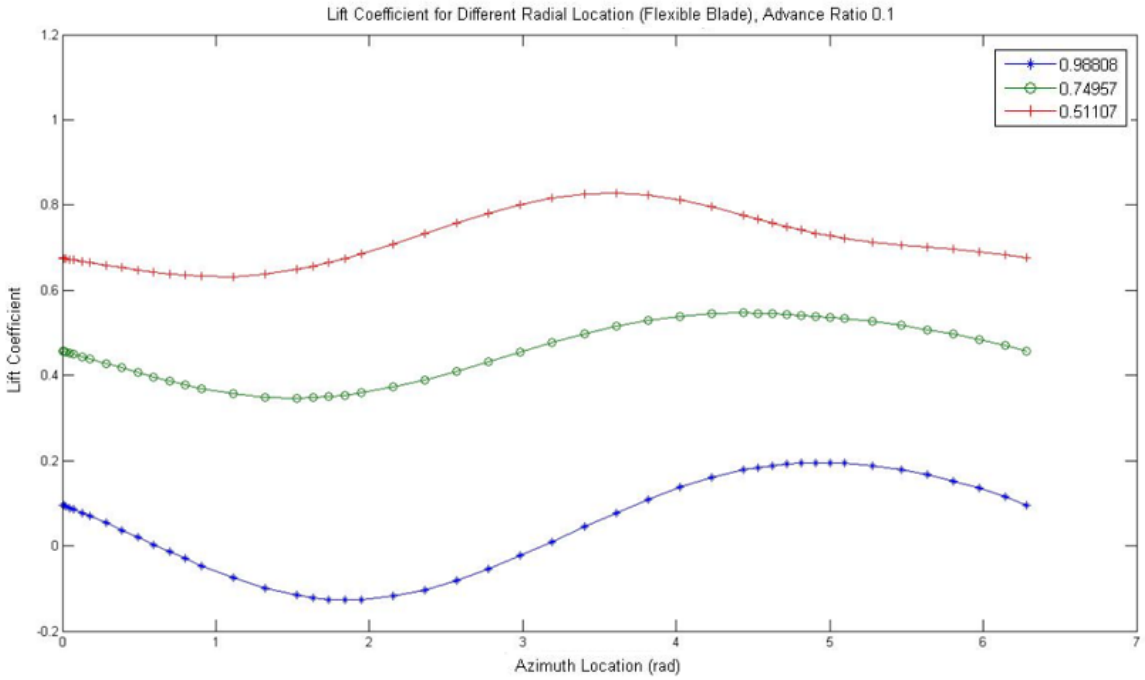

Figure 39 - Lift coefficient at different radial locations at an advance ratio of 0.1 for a flexible blade

At higher advance ratios there is a real possibility of stall. This is evident in Figure 40. The flap response shown in Figure 29 previously, shows an increase in flap angle at 0.5π. This increases in lift stalls the blade tip in the negative region. At mid span there is a rapid decrease in the lift which is caused by the large induced angle of attack gradients; this forces a small effective angle of attack.

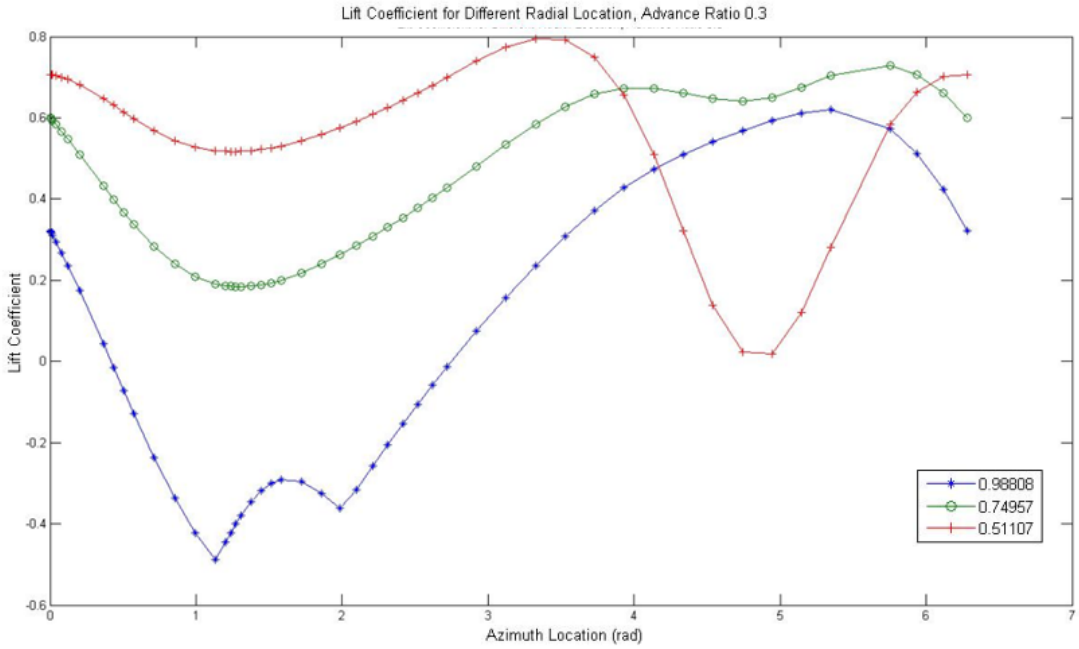

Figure 40 - Lift coefficient for different radial locations at an advance ratio of 0.3

The flexible blade has numerous stall points at the tip and mid span locations.

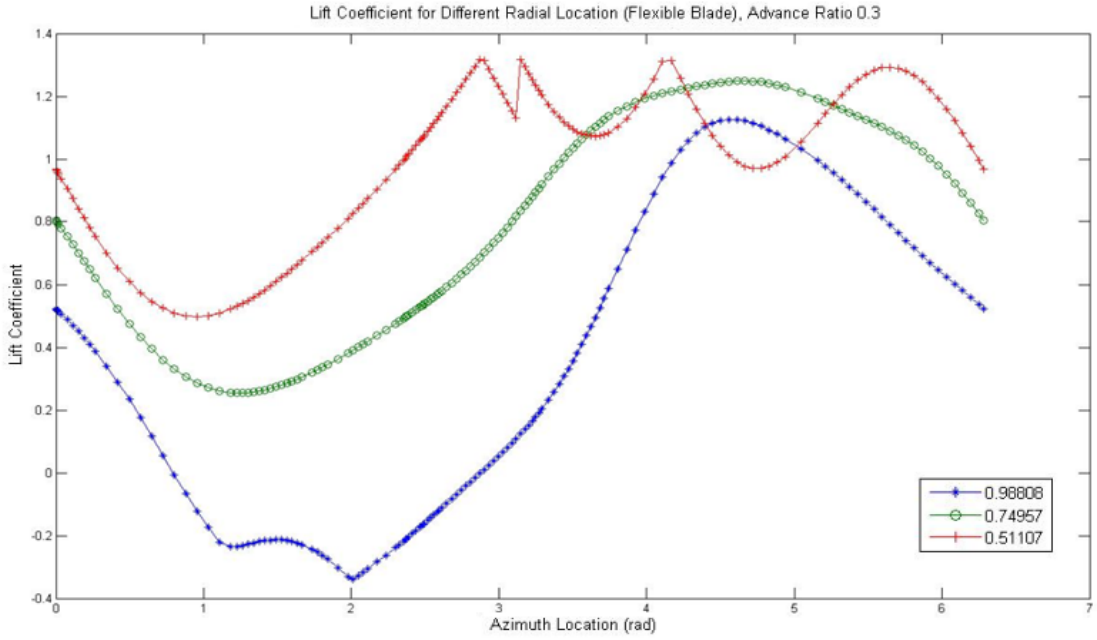

Figure 41 - Lift coefficient for different radial locations of a flexible blade at an advance ratio of 0.3

The advancing side stalls in the negative region and there are three stall points on the retreating side at the mid span. This high lift is caused by the increase in the commanded pitch in combination with the large deflection rate due to the elastic restoring energy.

Another important degree of freedom is the pitch motion and its influence on the blade response. Working under the assumption of a rigid control system the influence of pitch is entirely from the commanded control input. For a low advance ratio with three different centre of gravity offsets are plotted in Figure 42. The rigid blade deflection with a centre of gravity aft (positive direction) of the pitch axis, is larger than the baseline with no offset.

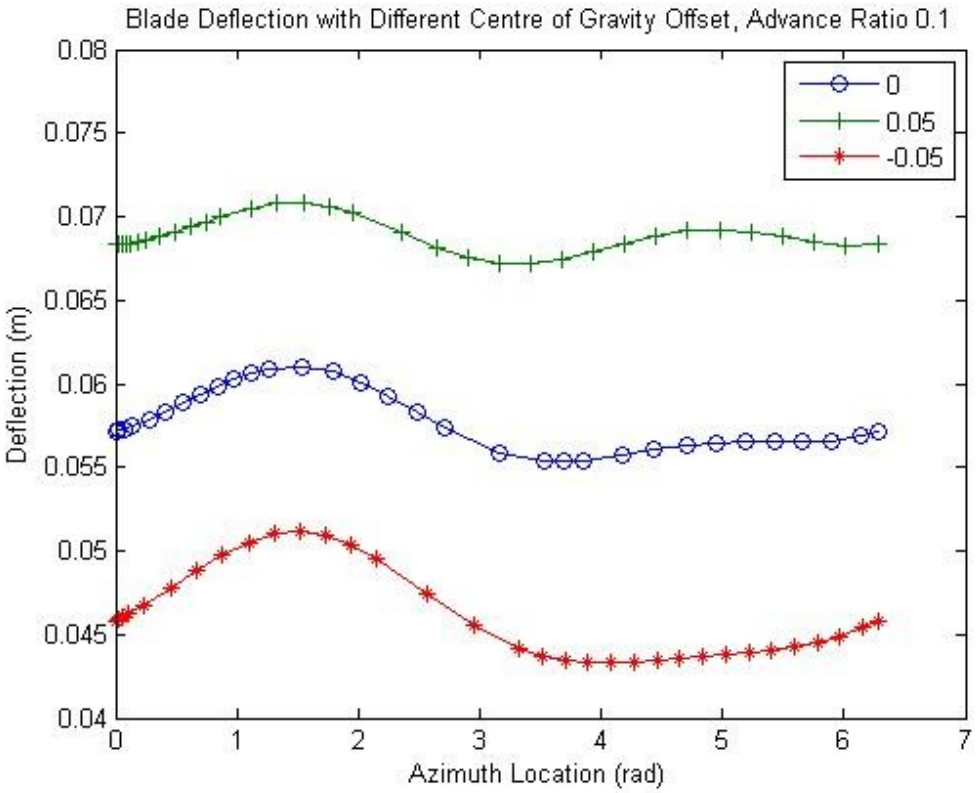

Figure 42 - Centre of gravity influence on blade deflection with different offset values. Offset values are a percentage of the chord length

The pitching inertia of an aft placed centre of gravity opposes the flapping inertia. This lower net inertia forces an increase in flap deflection. With a fore placed centre of gravity, the pitch inertia adds to the flap inertia which reduces the flap deflection. The next section will compare the results to published values. First the results for trim and hover will be compared to a simple model, and then the results will be validated against the UH-60.

2.4.2.3. A Simple Validation

This section will validate the trim code under different blade geometries. The first case to be presented is an untwisted blade with a constant lift curve slope of 5.73/rad, a zero lift drag coefficient of

0.01, a fuselage drag coefficient of 0.01, a lock number of 5, a solidity of 0.05, a weight coefficient of 0.005, and a rigid flap frequency of 1.15/rev. The published results for this case are from ref (21). For their mathematical model they used a coupled flap-lag-torsion rigid ordinary differential equation. The blade has coincident flap and lag hinges with a spring for each degree of freedom. Also there were two springs used to model the flexibility of the hub in the flap and lag directions. The results of the current work and from ref (21) are presented in Figure 43.

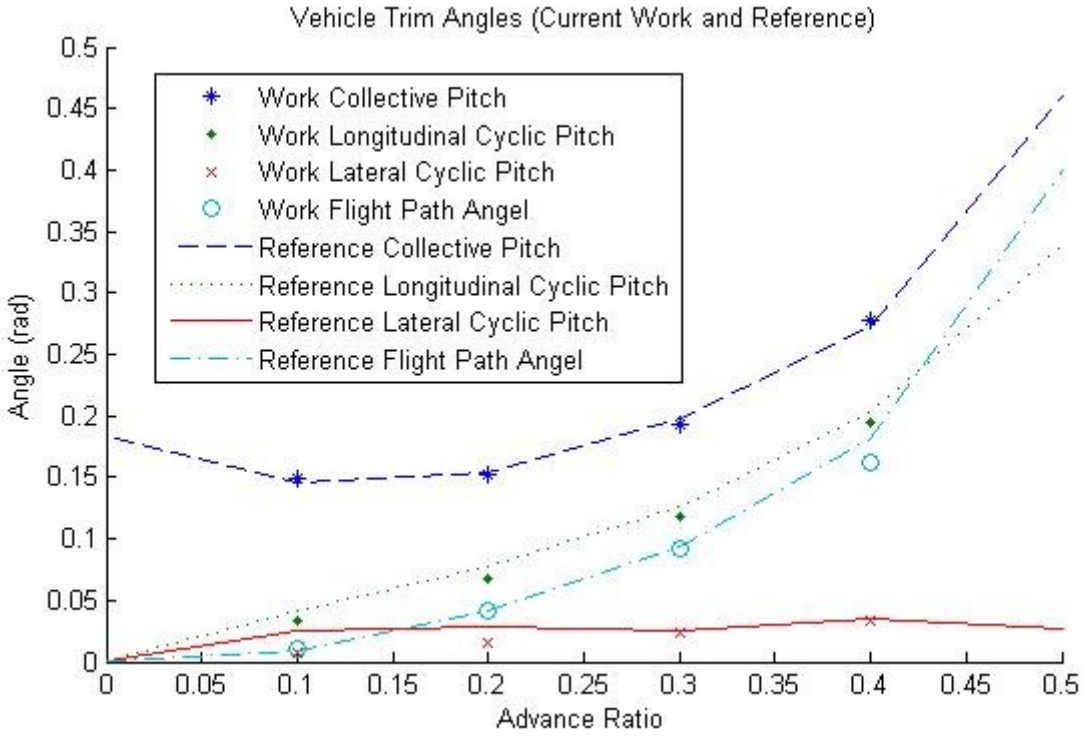

Figure 43 - Control and attitude angles comparing the current work to ref (21)

The results correlate fairly well. The largest discrepancy is due to the lateral cyclic pitch angle. At an advance ratio of 0.3 and 0.4 the results correlate very well however at 0.1 and 0.2 the results differ slightly. At the low advance ratios the moments at the hub are small so it is expected that the control angles be small as well. In ref (21) they included a lateral tilt of the shaft will force the weight coefficient to contribute to the roll moment equations, this could be the main reason for the difference in result. At higher advance ratios the roll moment from the rotor will be larger compared and will hence influence the trim rolling moment equation more than the weight.

For hover the performance in terms of power coefficient, thrust coefficient and figure of merit will be compared to results from ref (1). Figure 44 below shows the variation of power coefficient with

different collective pitch angles for different solidities. The results correlate well with Figure 73 in the appendix. The power coefficient agrees well for higher solidities with low pitch angles. At higher pitch angles the difference in theory and experiment becomes more apparent.

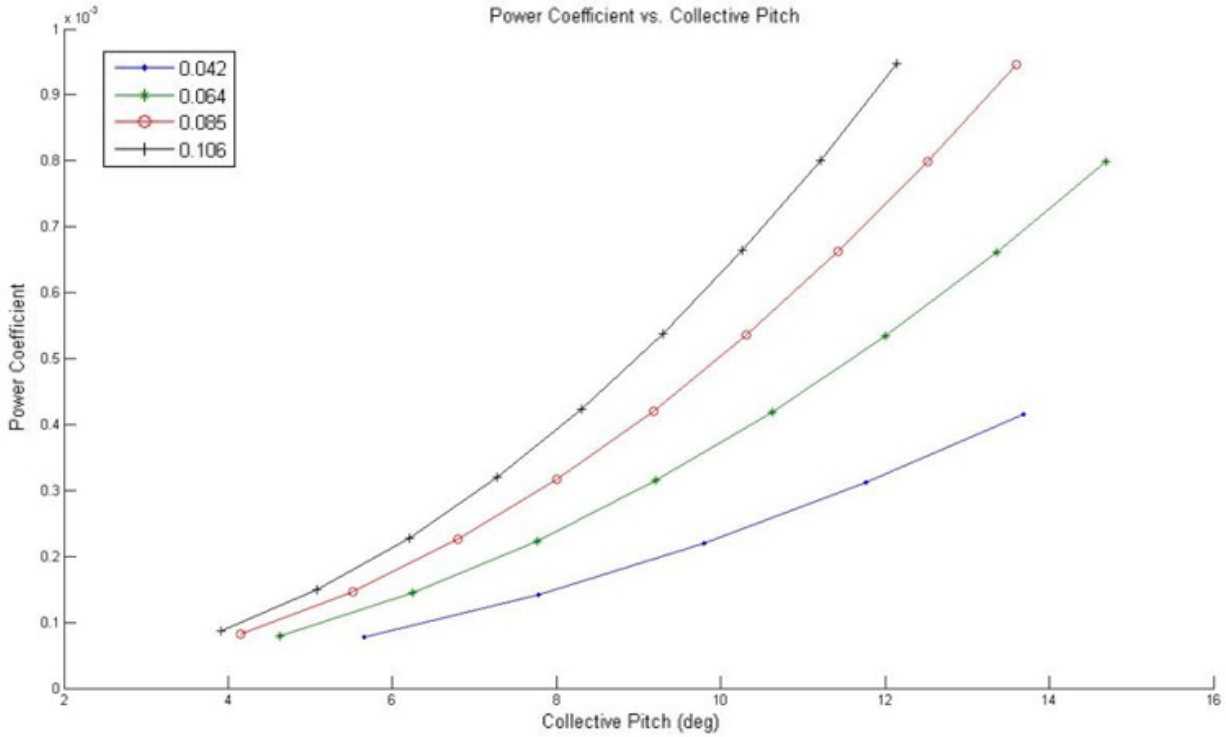

Figure 44 - Power coefficient in hover vs. collective blade pitch for different solidities

Figure 45 shows the variation in thrust coefficient with collective pitch for different solidities. There is a slight over prediction for larger solidities for a collective pitch lower than 13 deg when compared to Figure 74 in the appendix.

(Figure 45 next page)

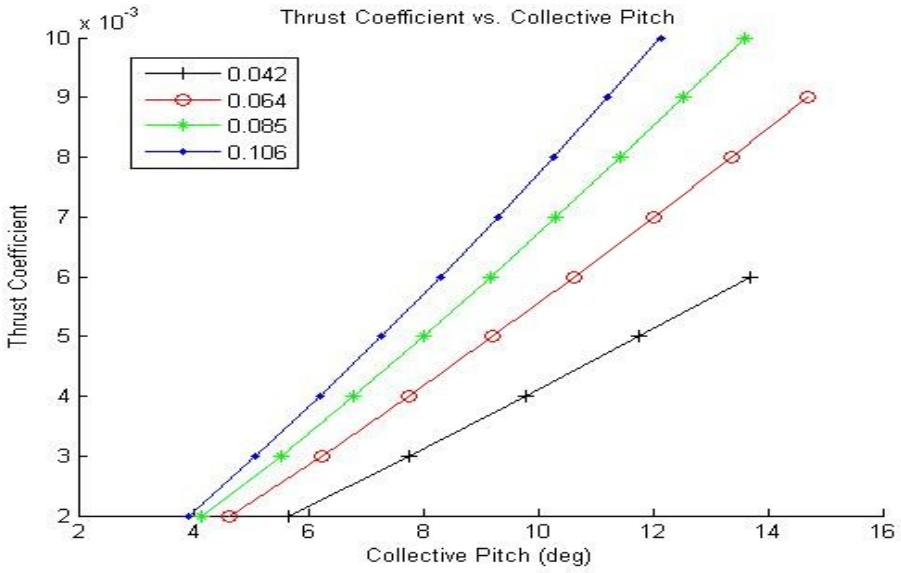

Figure 45 - Thrust coefficient in hover vs. collective blade pitch for different solidities

2.4.2.4. Work vs. UH-60

This section will compare the rotor performance, trim control settings, and blade response to ref (23). Ref (23) compares the results from CAMRAD II (26) to that of flight test (FT) (27)data. CAMRAD II has the ability to model a rotor blade with advanced numerical methods. The wake is modeled using a free wake approach. In the free wake approach, the wake consists of a finite number of filaments emanating from the blade. The goal of this approach is to find the trajectories of the wake filaments due to the self-induced effects in the wake (28) and its influence on blade. It also has the capability to solve the aerodynamic loads using a dynamic stall model from ref (9). CAMRAD (29) and CAMRAD II are different programs, however for the current work CAMRAD II will be referred to as CAMRAD only.

The power coefficient for forward flight under different weight coefficients will be compared to published results. The power coefficients have been calculated for four different weight coefficients (0.0065, 0.0074, 0.0083, and 0.0091). Only the first and last cases will be compared here. The other two will be in the appendix. The first case to be presented is the low thrust case with a weight coefficient of 0.0065. In Figure 46 below there is a plot of the power coefficient for different advance ratios. The CAMRAD model is coincident with the flight test. The current work shows decent correlation for advance ratios up to 0.25. At low advance ratios there is a slight under prediction. At larger advance ratios there is a large over prediction.

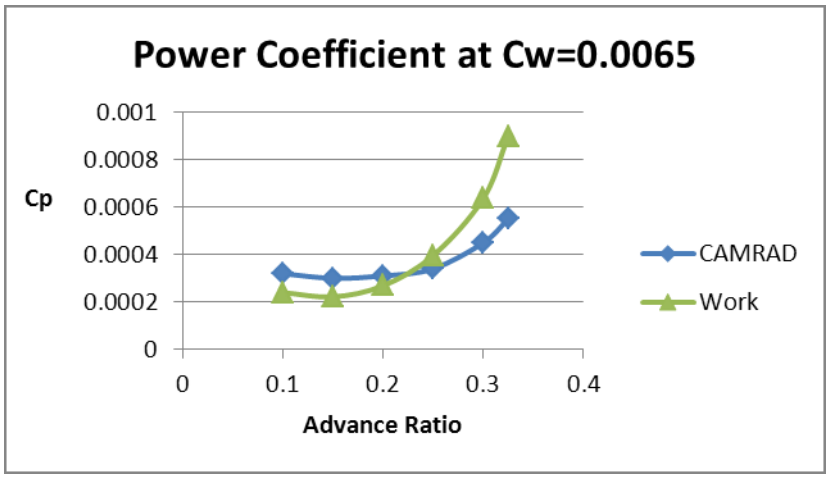

Figure 46 - Power coefficient for low thrust of 0.0065 at different advance ratios

A medium thrust case of 0.0091 is presented below for three advance ratios. For the lower advance ratios the power coefficient is slightly under predicted but at 0.3 the result is very close. To achieve better results it would be necessary to include a drag polar plot at different mach numbers with a 2D-Table look up procedure. An attempt was made to incorporate the drag polar however the computational time was substantial compared to the simple zero lift drag coefficient approach described earlier. The current model uses a rectangular blade, whereas the UH-60 has a swept tip. This could explain the discrepancy at advance ratios greater than 0.25.

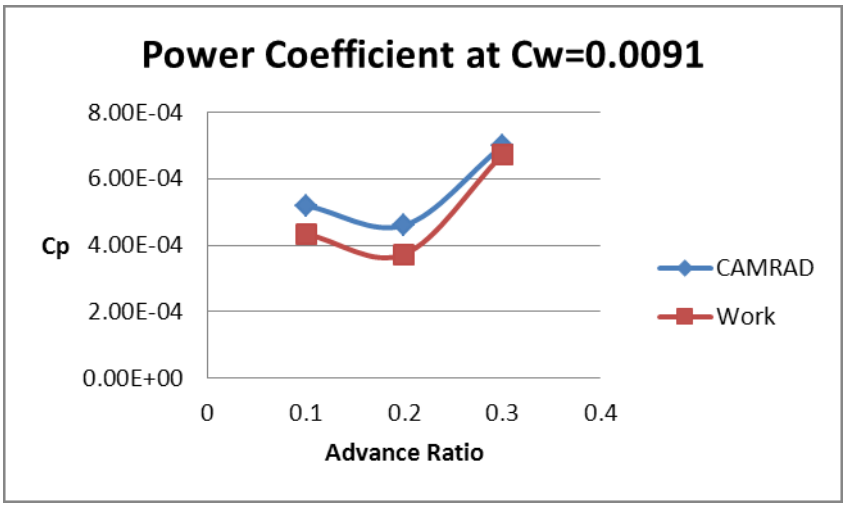

Figure 47 - Power coefficient for medium thrust of 0.0091 at different advance ratios

The trim process with was performed with a weight coefficient of 0.0065. The first comparison will be made with the collective pitch against the results from CAMRAD II and FT. The collective pitch is being measured at the 75% radial location.

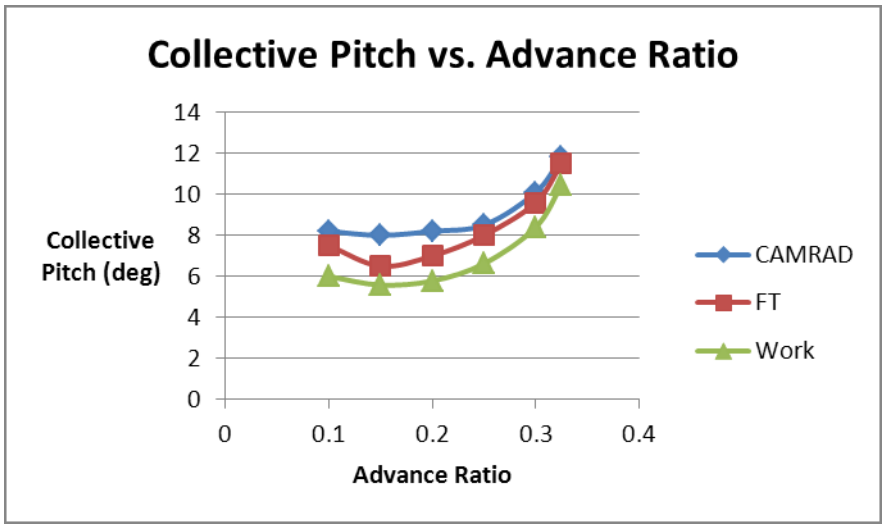

Figure 48 - Collective pitch θ_0 comparison at different advance ratios

The collective pitch has been under predicted again, most likely due to the absence of the lag and pitch degree of freedom. Also the inflow model being linear is a simplification of the induced velocity. In reality the induced velocity is nonuniform. However the plot does follow the general trend of the pitch with a higher collective pitch for the low advance ratio compared to the intermediate advance ratios. After 0.25 the collective pitch climbs rapidly. The next plot to be analyzed is the lateral cyclic pitch.

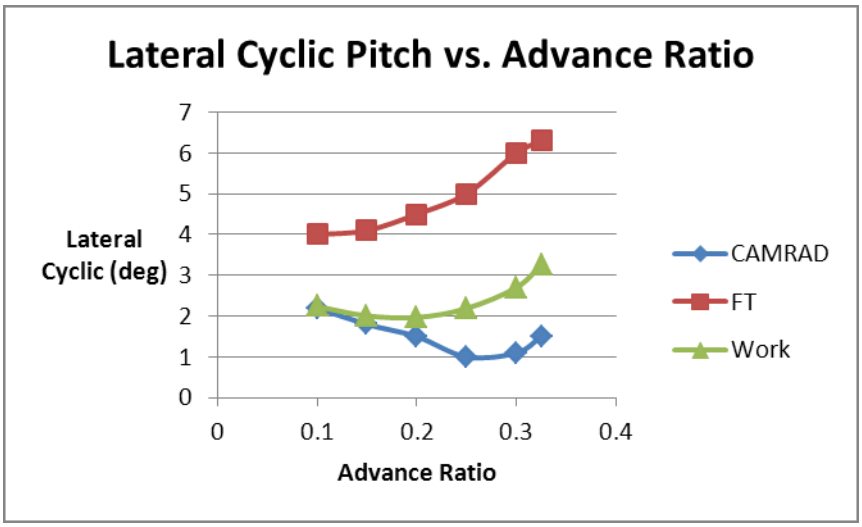

Figure 49 - Lateral cyclic θ_{1s} pitch comparison at different advance ratios

It is quite clear there is a large difference between the current work and the FT, however the results agree slightly better than CAMRAD. The flight data were obtained for a zero roll angle, that is, no steady lateral acceleration on the pilot. To accomplish this, the pilot tends to fly with a small amount of sideslip and uses the aircraft's static dihedral to zero the roll angle (23). This small amount of sideslip will create

a rolling moment of the fuselage as shown in the rolling moment equation in ref (24). This will force an increase in the lateral cyclic pitch. The assumption of zero sideslip previously stated will produce zero roll moment, therefore only the influence of the rotor's rolling moment is the contributor to the rolling moment equilibrium equation. The longitudinal cyclic pitch control is presented in Figure 50.

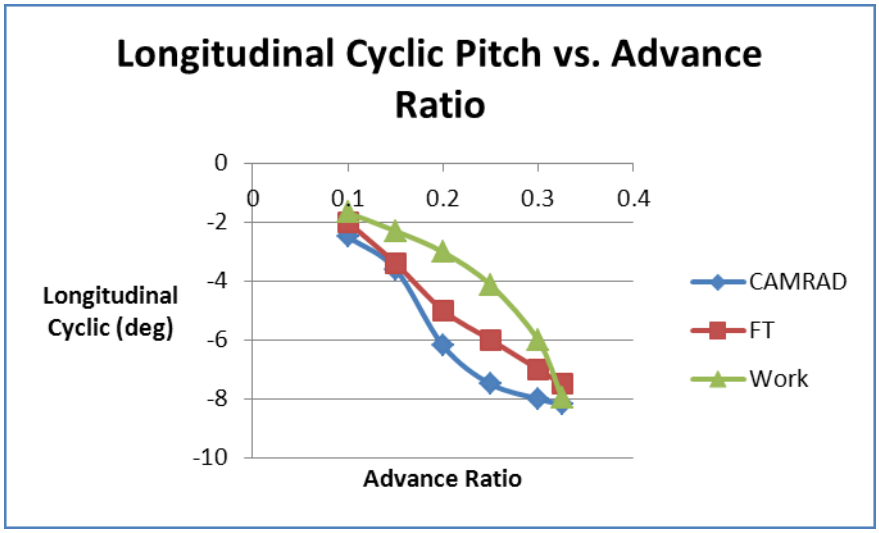

Figure 50 - Longitudinal cyclic θ_{1c} pitch comparison at different advance ratios

There is decent correlation for the low and high advance ratios but the values for the moderate advance ratios are slightly under predicted. The FT data was measured with an angle for the horizontal stabilator. The same angle was used for the CAMRAD model in ref (23). The equilibrium equations used for the current work ignore the influence of fuselage control systems. The flight path angle is presented in Figure 51.

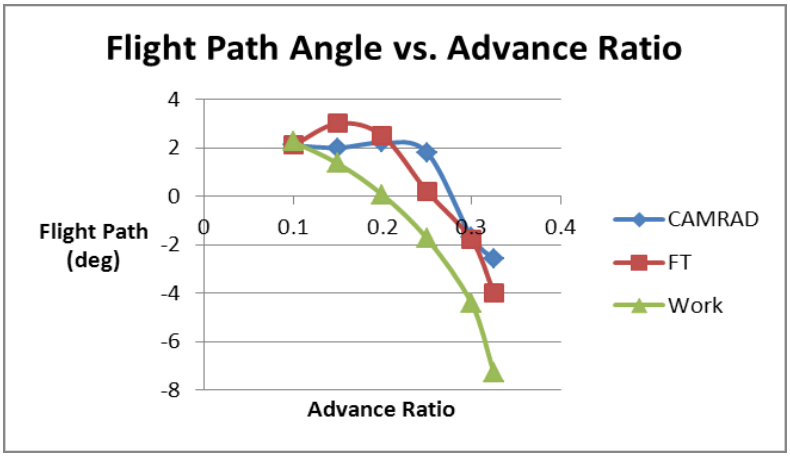

Figure 51 - Flight path angle for different advance ratios

The flight path angle defined as the angle of the hub plane with respect to the incoming flow contributes to the induced velocity over the disk. Also it significantly influences the equilibrium equations. The flight

path angle is over predicted slightly but follows the general trend for advance ratios greater than 0.2. This discrepancy could also explain the sudden rise of the power coefficient presented earlier. The flap response of the blade in terms of the coning angle with lateral and longitudinal tilt will be analyzed next.

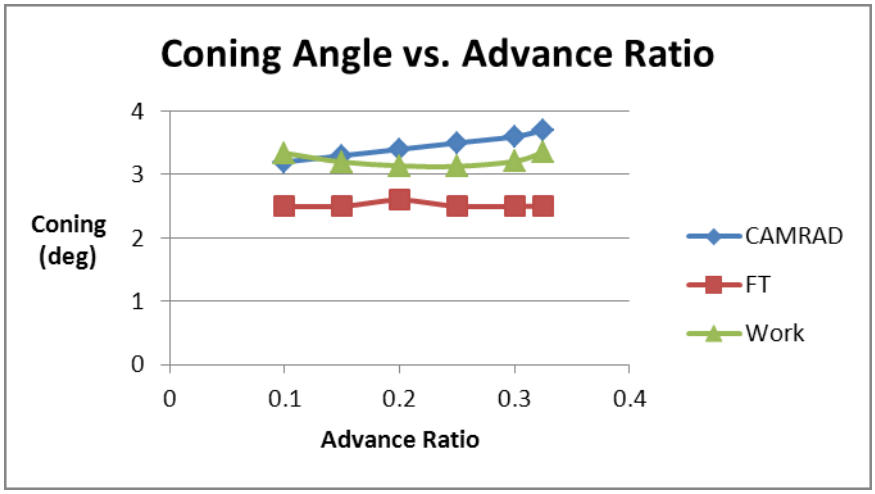

Figure 52 - Coning angle for different advance ratios

The coning angle agrees well with CAMRAD model but moderately over predicts the FT. Ref (23) identifies that a measurement bias in the FT data which could explain the difference in results between CAMRAD and FT. The results for lateral and longitudinal flapping have a poor correlation.

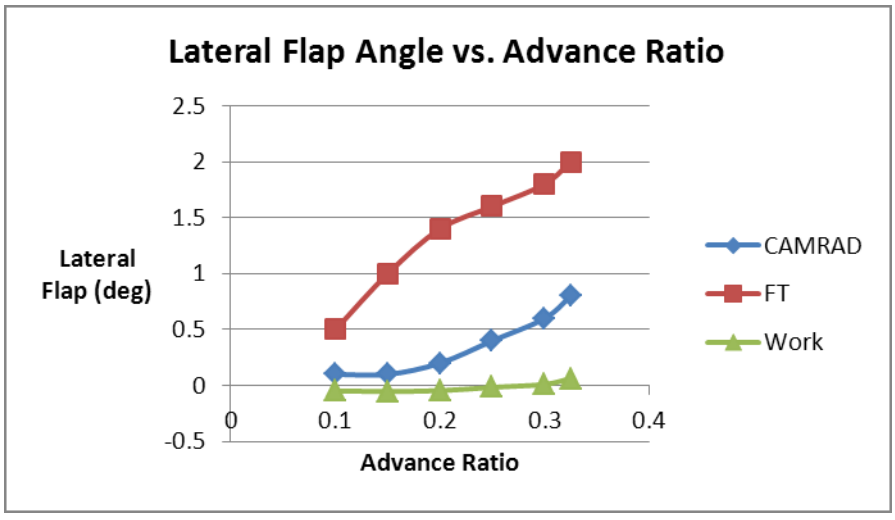

Figure 53 - Lateral flap angle β_{1s} for different advance ratios

It is quite clear that the results above are in error. However this result was expected. Under the assumption of zero sideslip and zero roll angle yields zero roll moment of the fuselage and the only

contributor to the roll equilibrium equation is the rolling moment of the rotor. Referring back to the rotor rolling moment equation on page 34, by forcing β_{1s} to zero the rolling moment also becomes zero.

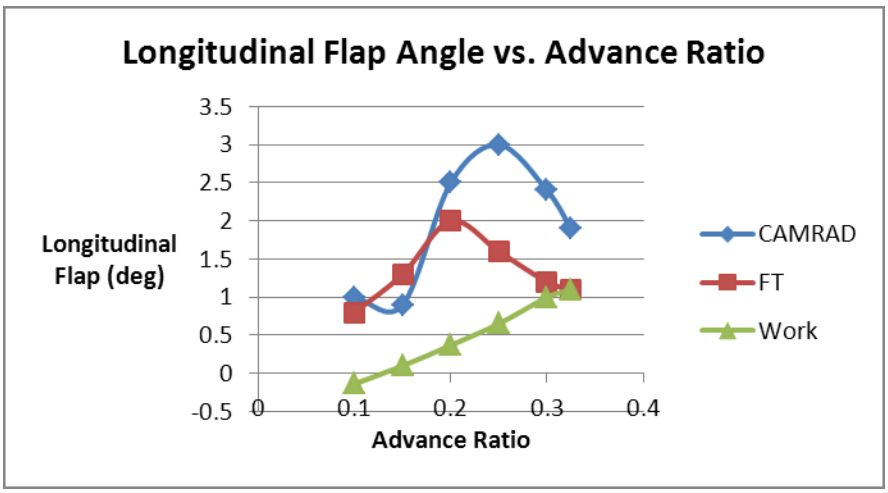

Figure 54 – Longitudinal flap angle β_{1c} for different advance ratios

There is a large discrepancy for the longitudinal flap angle as well. The difference in the results could be explained by the fuselage characteristics. Ref (24) was published in 1980 for the UH-60 and the results used for the validation were published in 2002 for the UH-60A helicopter. The two rotors are almost identical but the fuselage design could be different. For example ref (24) the fuselage drag performance was shown to be slightly different compared to the equations used by ref (23). The centre of gravity location and pitching moment could also be different. To summarize the results above, all correlations varied from poor to fair, even CAMRAD II, which is considered to be one of the best codes for rotorcraft, had discrepancies. The most likely cause for the difference in results is the relative simplicity of the aerodynamic/dynamic models. The reason for choosing the model being implemented is for is relatively low computational cost. A more accurate model will be required which should take into account flexible flap/lag/torsion degrees of freedom as well as unsteady aerodynamics with a wake model that can model the nonlinearities of the inflow along the blade. Such a model will be more computationally expensive. Even with the poor to fair results the model does trim and is able to capture some of the trends exhibited from CAMRAD II and FT, therefore it should be sufficient for an optimization process.

Chapter Three - Optimization

3.1. Introduction

Multidisciplinary Design Optimization, MDO, *"can be described as a methodology for design of complex engineering systems that are governed by mutually interacting physical phenomena and made up of distinct interacting subsystems"* (30). In other words, MDO utilizes optimization techniques to solve problems that feature various disciplines. These discipline platforms are incorporated simultaneously and an optimal solution is provided. Since the interaction between disciplines is taken into consideration, the multidisciplinary solution is superior when compared to the individual optimization of each discipline. The complexity of engineering problems has sparked a growing interest in multidisciplinary optimization. Rotorcraft is interdisciplinary because the flexibility of the main rotor blades couples with aerodynamics, dynamics, and control systems. In addition interaction between rotor and the fuselage further complicates helicopter system predictions (13).

3.2. Literature Review

The multidisciplinary nature of the helicopter of the helicopter engineering problems has led researchers to investigate formal optimization methods for the design process (13). The first optimization studies for rotorcraft begin in the 1980's. Early design optimizations were primarily gradient based since computer power was more valuable than it is today.

Chattopadhyay and Walsh (31)performed a structural optimization to reduce the blade weight. Constraints were imposed of multiple coupled flap-lag natural frequencies, autorotation inertia and centrifugal stresses. The design variables used were the box beam cross sectional dimensions (wall thicknesses), the magnitude of nonstructural masses, and the blade taper ratio. To decrease the computational time analytical derivatives of the objective function, autorotation, and the stress constraint were used. A central differencing scheme was used to find the gradients of the frequency constraints. They performed their analysis on a rectangular blade and a tapered blade with different design variables and constraints. Three different constraint cases were presented. The first case imposed constraints on the first three lag frequencies and the first two flap frequencies, autorotation inertia, and stress. The second case removed the stress constraint and the last case only constrained the first lag and flap frequency with autorotation inertia. The first optimization result for the rectangular blade only considered the box beam thicknesses as the design variables and for each constraint case

there was a reduction in blade weight. The third constraint case yielded the best improvement. With the addition of a non-structural mass the weight was reduced even further since the autorotation inertial was no longer dependent only on the structural mass. This allowed for a reduction in structural dimensions by increasing the weight outboard of the blade. The tapered blade shows a further reduction of the weight due to the decrease in structural mass, compared to the rectangular blade, the non-structural mass at the tip is greater to satisfy autorotation. In another paper by the same authors (32) they extended their work to include an integrated dynamic and aerodynamic model used for structural optimization. Blade weight and 4/rev vertical shear are minimized in the presence of airloads under forward flight conditions using both single and multiple objective functions formulations. Constraints are imposed on the first four coupled natural frequencies, the blade autorotational inertia and the centrifugal stress. They used a global criteria approach which combines both of the objective functions into one function.

$$F = \left(\frac{f_1 - f_1^*}{f_1^*}\right)^2 + \left(\frac{f_2 - f_2^*}{f_2^*}\right)^2 \tag{3.1}$$

This equation represents the sum of the squares of the deviations from the reference blade. The approach yields a design in which the blade weight is lower than that obtained by using the blade weight as the single objective function. The hub vertical shear is somewhat higher than that obtained by using the hub vertical shear as the single objective function. The optimum blades are all tapered in contrast to the reference blade which is rectangular. In all three optimization formulations studied the center of mass of the blade remains forward of the quarter chord point. Inspection of the airload distributions for the initial and the optimum designs indicate that optimization significantly reduces the amplitude and alters the distributions favorably to help achieve the goal of low vibration.

Chattopadhyay and MaCarthy (33) performed an integrated optimization procedure for rotor blades with coupling of blade dynamics, aerodynamics, aeroelasticity and structures. The objective was to reduce vibratory shear forces at the blade root with constraints imposed on radial and inplane shear, flapping and torsional moments, power coefficient, thrust, weight, autorotation inertia, and aeroelastic stability which involve constraining the centre of gravity forward from the elastic axis. The blade was modeled as a doubled celled box beam, with the thicknesses at different spanwise locations as the design variables. Blade root 4/rev vertical shear and 4/rev lagging moments were reduced. A Minimum Sum β (34) approach was used to formulate the multiobjective problem. McCarthy and Chattopadhyay

(35) extended their work to include a blade that was modeled as a composite box beam with nonlinear chord and twist distribution. Ply thicknesses and non-structural weights were also design variables. The multiobjective function was formulated as a Kreisselmeier-Steinhauser (K-S) function (36). This approach combines both the objectives and constraints into a single objective function. For their work they tested three cases: the first case used only aerodynamic design variables, the second comprised only structural, and the third combined both aerodynamic and structure. Their results indicate that the structural design variables were most effective in reducing the vertical shear and the aerodynamic variables were effective in reducing the power coefficient. A combined approach yielded the smoothest convergence and was most effective for the overall integrated problem.

He and Peters (37) performed a combined structural, dynamic and aerodynamic optimization of rotor blades using a simple box beam model to represent the structural component of the blade. The blade performance was optimized using the power required in hover as the objective function and constraints were imposed on natural frequencies, blade stress, and fatigue life. However an assumed blade loading was used and the optimization decoupled into two levels. The problem was addressed sequentially, the hover performance was improved first then the natural frequencies. Walsh et al (38) described a fully integrated aerodynamic/dynamic optimization. The procedure combines power required in hover, forward flight, and maneuver with vibratory hub shear. Similar design variables mentioned from other papers such as nonstructural masses were used. Some unique constraints were imposed on airfoil section stall, drag divergence Mach number, and trim iterations. Designs from an integrated and sequential (performance was optimized first then dynamics) approach were compared. The integrated approach produced superior results.

The mentioned sources above were all gradient based optimizations. They used CONMIN (39) which is a constraint minimization general purpose optimization code, with CAMRAD (29) as the principal aerodynamic/dynamic solver. These early studies focused on reducing rotor induced vibrations, performance improvement, and weight reduction. The primary design variables were nonstructural mass magnitudes and their locations, stiffness properties, taper, and twist. Autorotation inertia, stability, and stress were common constraints.

Non gradient methods in engineering are becoming popular because of their ability to find a global optimum and permitting the use of integer and discrete design variables. Lee and Hajela (40) applied a Genetic Algorithm (GA) to a rotor design problem. They found that the design space for rotor design was often nonconvex and design variables for cross section design were continuous, integer, or

discrete. The nonconvexity of the design space will make it a challenge for any gradient optimizer to find a global minimum. The objective was to design a blade geometry and structure to minimize a weighted sum of the rotor hub shear force and bending moments for a hingeless rotor in forward flight. The problem was divided into a set of subproblems, where they were solved in parallel. Fanjoy and Crossley (41) used a GA to design helicopter rotor airfoils. The objective was to maximize the lift to drag ratio of the airfoil as the blade passed the 90, 180, and 270 azimuth locations. Constraints were imposed in order to aim the new airfoil to be as good as or better than the NACA0012 airfoil. The analysis was performed with an invsicid panel method with a boundary layer method for drag estimation. The result returned an airfoil that was better than the NACA0012. Simulated Annealing (SA) is another evolutionary based algorithm but it has not be as widely used as the GA. The Particle Swarm algorithm is another evolution based code but to the authors knowledge it has not yet been used by the rotorcraft industry.

3.3. Algorithm

This section will describe the optimization algorithms that will be used. The Sequential Quadratic Programming method will be described briefly. More emphasis of the section will be placed on evolutionary algorithms such as the Genetic Algorithm and Particle Swarm.

3.3.1. Sequential Quadratic Programming (SQP)

The Sequential Quadratic Programming (SQP) is one of the most widespread algorithms employed in nonlinear continuous optimization. SQP is characterized as being efficient and greatly reliable. Its deterministic nature computes gradients by differentiation and finds the optimal step size. The sequential quadratic programming algorithm is most excellent at solving continuous variable problems. SQP's computational time is admirable when compared to robust GAs because it converges rapidly. On the other hand, SQP has its disadvantages. Its optimal result could be only a local minimum which endangers the problem solution. As shown in Figure 55, the two local minimums are not an acceptable solution. Since it is gradient based, it needs direction and the bottom of the slope could possibly be identified as a global minimum, causing it to be converged prematurely. At the same time, SQP assumes that the objective function and constraints are smooth function.

(Figure 55 next page)

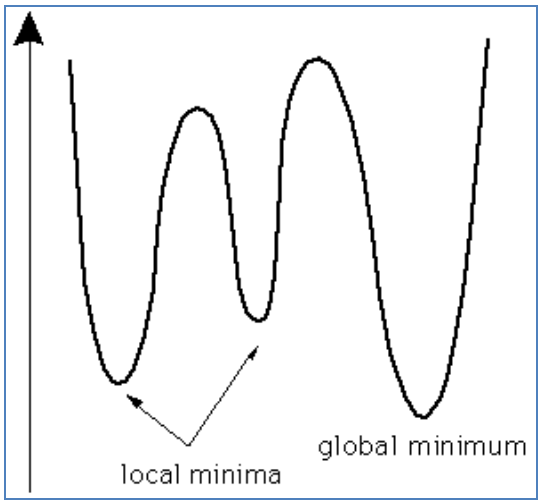

Figure 55 – A sample plot showing the difference between global and local minimum

$$\min \ f(x)$$
$$\text{s.t. } b(x) \geq 0$$
$$c(x) = 0$$

- function f(x) to be minimized
- non-equality constraint
- equality constraint

The above problem presents a typical optimization problem. Function f(x) is called to be minimized while satisfying the constraints b(x) and c(x). These constraints are of non-equality and equality natures, respectively. At each step, a local model of the optimization problem is constructed and solved, yielding a step towards the solution of the original problem. In unconstrained minimization, only the objective function must be approximated, and the local model is quadratic. An SQP method uses a quadratic model for the objective function and a linear model of the constraint. A nonlinear program in which the objective function is quadratic and the constraints are linear is called a Quadratic Program (QP). An SQP method solves a QP for each iteration. At each major iteration, an approximation is made of the Hessian of the Lagrangian function using a quasi-Newton updating method. This is then used to generate a QP subproblem whose solution is used to form a search direction for a line search procedure (22).

3.3.2.Genetic Algorithm (GA)

Genetic Algorithm is a stochastic optimization method which is based on Darwin's theory of evolution and natural selection. Just like in genes, the essential principle supports the idea of the "survival of the fittest". For each iteration, a requested population is generated for each design variable.

Afterwards, the design variables are paired up with one another and provide different solutions. Only the pairings that provide adequate best fit solutions are selected. The population evolves for many generations until a superior design is reached. It also incorporates mutation and migration which are random events to ensure a superior design is reached. The GA can handle both continuous and discrete variables. It is evolutionary based so no direction is needed. However, the computational time of a genetic algorithm when compared to an SQP is much more severe. It is less prone to premature convergence unlike the SQP algorithm. The genetic algorithm performs at a very robust manner, and it is mostly utilized to find exact or approximate solutions. However the GA is highly sensitive to the diversity of the initial population. If the range of the design variables is too large, a less than optimal solution will be the result.

3.3.3.Particle Swarm (PS)

Particle Swarm Optimization (PSO) was developed by Kennedy and Eberhart (42) as a stochastic optimization algorithm based on social simulation models. The algorithm employs a population of search points that moves stochastically in the search space. The best position ever obtained by a particle is held in memory. This is then communicated to part or the whole population, trying to encourage the other particles to move towards the most promising regions.

The population of N individuals or particles is referred to as the swarm S.

$$S = \{x_1, x_2, \dots x_N\} \tag{3.2}$$

Each particle has a location i.e. design variables defined as:

$$x_i = (x_{i1}, x_{i2}, \dots x_{iN})^T \; i = 1,2, \dots, N \tag{3.3}$$

The particles move within a search space by adjusting their position with a velocity

$$v_i = (v_{i1}, v_{i2}, \dots v_{iN})^T \; i = 1,2, \dots, N \tag{3.4}$$

Early variations of PSO used the following equation to determine the velocity of the i^{th} particle with the j^{th} location:

$$v_{ij}(t+1) = v_{ij}(t) + c_1 R_1 \left(p_{ij}(t) - x_{ij}(t)\right) + c_2 R_2 \left(p_{gj}(t) - x_{ij}(t)\right) \tag{3.5}$$

The velocity is updated based on the information from previous time steps. c_1 and c_2 are the cognitive and social parameters respectively supplied by the user. If c_1 is less than c_2 then the particles will be attracted to the global best solution. This global best position may not be the objectives global minimum solution, a premature convergence is possible depending on termination criteria. R_1 and R_2 are random numbers between 0 and 1. p_i is the best position the of the particle that it has ever visited. In other words it is the best position or combination of design variables that yielded the best objective. In addition to the personal best position there is a global best p_i. This represents the best position out of all of the N particles. After the new velocity is determined the position is updated:

$$x_{ij}(t+1) = x_{ij}(t) + v_{ij}(t+1) \tag{3.6}$$

After the position has been updated it is necessary to find the new personal best and global best. If the personal best is greater than the previous personal best then the personal best is updated to the current value. Otherwise the personal best is not updated. Each value of the particles new personal best is compared to the previous global best. If the new particle's personal best is greater than the global a new global is created.

To confine the particles within a specific search domain typically a hard domain boundary condition is employed:

$$x_{ij}(t+1) = f(x) = \begin{cases} LB, & x_{ij}(t+1) < LB \\ UB, & x_{ij}(t+1) \geq UB \end{cases} \tag{3.7}$$

This simply states that if the particles find themselves on the outside of the bounds, their positions will be clipped to equal the bounds. LB is the lower bound and UB is the upper. Two other boundary conditions are the reflection and absorbing boundary conditions. The reflection condition changes the sign of the velocity of the particle if the particles position is out side of the bounds. The absorbing

condition is similar but it sets the velocity to zero. Another issue faced by PSO is referred to as swarm explosion. This occurs when there is an uncontrolled increase in the magnitudes of the velocity. A simple solution to use is to clip the velocity at some user defined maximum value. Another issue with particle swarm is the concentration of particles around the best solutions. Searching in promising regions required strong attraction of the particles towards them with small position shifts. A new parameter called the inertial weight was introduced (43) (44) (45).

$$v_{ij}(t+1) = v_{ij}(t)w + c_1R_1\left(p_{ij}(t) - x_{ij}(t)\right) + c_2R_2\left(p_{gj}(t) - x_{ij}(t)\right) \quad (3.8)$$

The new parameter w reduces the perturbations that shift the particles away from the best position. The above velocity equations are for the standard PSO algorithm. The current work will use a Unification Particle Swarm Optimizer (UPSO). This method is explained with a MATLAB code in ref (46). The PSO has two main phases, exploration and exploitation. Exploration is responsible for detecting the most promising regions in the design space and the exploitation phase promotes converges around the best solution. The UPSO algorithm uses the concept of a neighborhood. The main idea is the reduction of global information exchange scheme to a more local one, where information is only passed to small parts of the swarm at each iteration. Instead of the particles communicating their best positions to the whole swarm, they only communicate their best positions to their neighbors. The global variant of a particle swarm converges faster toward the overall best position than the local one; therefore it has good exploitation capabilities. The opposite is true for the local variant. It is good for its exploration capabilities since only its position is communicated to its neighbors. The UPSO was created to combine the two variants. The global variant velocity update is given by:

$$G_{ij}(t+1) = \chi(v_{ij}(t) + c_1R_1\left(p_{ij}(t) - x_{ij}(t)\right) + c_2R_2\left(p_{gj}(t) - x_{ij}(t)\right)) \quad (3.9)$$

And the local variant velocity update is given by:

$$L_{ij}(t+1) = \chi(v_{ij}(t) + c_1R_1\left(p_{ij}(t) - x_{ij}(t)\right) + c_2R_2\left(p_{lj}(t) - x_{ij}(t)\right)) \quad (3.10)$$

χ is referred to as the constriction coefficient with a value of 0.729. The velocity of the particle is a weighted combination of global and local variants.

$$v_{ij}(t+1) = uG_{ij}(t+1) + (1-u)L_{ij}(t+1) \tag{3.11}$$

The parameter u is the unification factor. The unification factor can take values between 0 and 1. With a value of 0, the velocity equation reduces to the local variant permitting exploration. With a value of 1, the velocity equation reduces to the global variant permitting exploitation (the velocity update is reduced to the standard PSO algorithm). The value for u can be a quantized value or a dynamic value. For the current work a unification factor that linearly increases with iteration was used. In the early stages of optimization, exploration is essential to find the best positions in the swarm. Exploitation is desirable when the solution starts to converge.

Everything up to this point has assumed that only side constraints exist for the design variables. To implement nonlinear constraints a penalty function approach will be implemented. The penalty function (47)to be used is defined as:

$$f_p(x) = f(x) + H(x) \tag{3.12}$$

$f(x)$ is the original objective value and $f_p(x)$ is the new penalized objective value. With H(x) defined as:

$$H(x) = w_1 H_{NVC}(x) + w_2 H_{SVC}(x) \tag{3.13}$$

$H_{NVC}(x)$ is the number of violated constraints and $H_{SVC}(x)$ is the sum of violated constraints. w_1 and w_2 are weight coefficients that were set to 1e9 for the current work. The sum of the violated constraints is defined as:

$$H_{SVC}(x) = \sum_{i=1}^{k} max\{0, C_i(x)\} \tag{3.14}$$

This penalty function selected was selected for its ease of implementation. It works well with both the GA and PSO algorithms. An example is presented in the appendix.

3.4. Optimization Structure

The following section will present the architecture of the optimization procedure including the organization, design variables, and constraints.

3.4.1. Multidisciplinary Feasible Method

Multidisciplinary Feasible Method is a design strategy which can be employed in for various multidisciplinary analysis problems. Its application is intended for large-scale distributed analysis. Initially, a complex problem is partitioned into a number of sub problems. Each of these sub-problems is treated as a discipline of analysis and they are interconnected with one another by means of a system-level coordination process. As shown in Figure 56, the disciplines are executed individually, but they also pass certain outcomes to each other. Ultimately, the optimizer generates inputs which slowly start converging the outcome, and satisfy the constraints of each discipline.

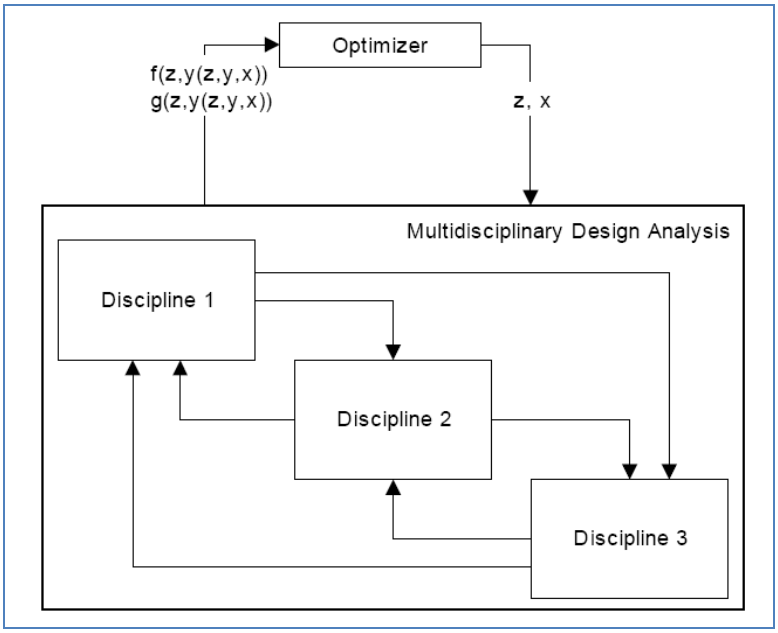

Figure 56 - MDF Block Diagram (48)

When compared to traditional solution architectures, the Multidisciplinary Feasible Method has more advantages. The above diagram demonstrates that MDF maintains a level of disciplinary independence

and permits parallel optimization. Furthermore, MDF reduces the amount of information passed between disciplines, which consequently reduces computational time. The employment of such optimization strategy allows for the removal of large iteration loops.

3.4.2.Design Variables

The importance of each design variable to the performance of the rotor will be examined. The first design variable to be introduced is the blade twist. Blade twist can significantly improve the figure of merit of the rotor. A negative twist of the blade will redistribute the airload over the blade to reduce the induced power.

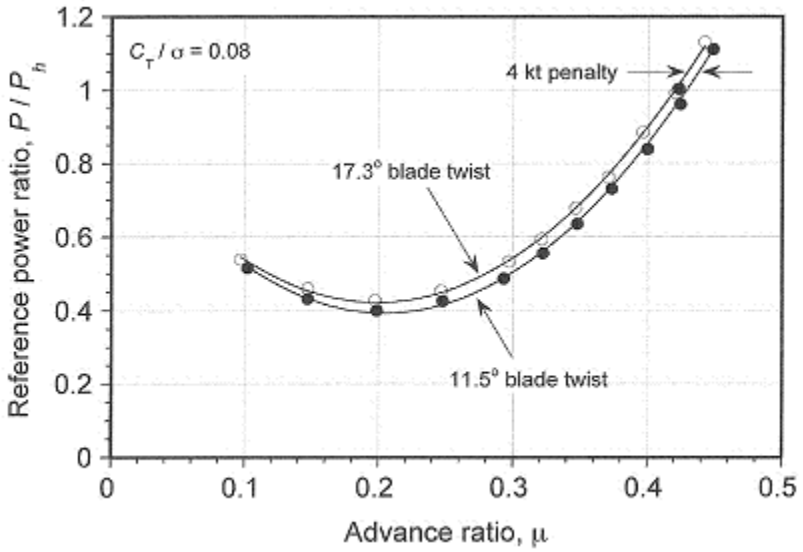

Figure 57 - A loss of performance with highly twisted blades may be expected in forward flight (1). Data source (49)

High degrees of twist in forward flight may suffer some performance loss. High negative angles of attack near the blade tip on the advancing side will experience a negative lift thus reducing the thrust for propulsion. A trade off will be required for hover and forward flight. Most helicopters will have a twist of -12 to -16 deg. This high degree of twist is made possible with advanced construction materials such as composites. More advanced rotors will have a nonlinear twist or a double linear twist. For the current work a linear twist will be used.

The rotor chord length is another aerodynamic design variable. The chord influences the rotor solidity $\sigma = N_b c/\pi R$ for a rectangular blade. The chord is directly related to the lift being generated by the blades. In hover a smaller solidity will improve the figure of merit since the drag induced by the lift

will be reduced, however to maintain vertical thrust with a small chord will require a larger angle of attack and stall may be of concern. With respect to forward flight, a small solidity will require more tilt of the disk plane and higher collective pitch to generate enough thrust to over come drag. Dynamic stall on the retreating side is highly possible.

The first dynamic design variable are the nonstructural masses. A nonstructural mass or tuning mass helps to improve the flapping characteristics of the blade. For example the vertical shear force:

$$S_z = \int_0^R (F_z - m\ddot{z})dr \tag{3.15}$$

This is the reaction of the net force of lift and inertia on the hub in the rotating frame. To reduce the shear force at the hub an increase is blade mass would be required. The nonstructural mass also contributes to the rotor's autorotation inertia, which will be explained in the next section.

The blade section centre of gravity is another variable that influences the dynamics of the rotor. From the previous equation for flapping on page 39 it is evident that the offset will provide some influence to the flap rate due to the pitching motion of the blade. Also the non-structural mass offset is another design variable that will influence the flap motion by changing the blade section centre of gravity. The nonstructural mass will be offset between the pitch axis and leading edge.

Another dynamic design variable is the bending stiffness. The bending stiffness can be represented in two different ways. The first method which has been used frequently in early design optimizations (50)and (51) is to use a general stiffness bounded in a certain range. The second approach is to model the internal structure of the blade section.

3.4.3.Constraints

Constraints are necessary to ensure that the design is in a safe operating environment or to maintain a certain level of performance. The first constraint to be presented is the frequency placements. This constraint is common to all published articles the author has reviewed on design optimization for rotor blades. The frequency constraints bound the flexible natural frequencies of the blade to be within a certain range. This range is to ensure that the rotating natural frequencies are an integer multiple away from the blade rotation speed. Resonance of the blade must be avoided.

$$b_i = \frac{f_k}{f_{ku}} - 1 \leq 0 \; and \; b_i = 1 - \frac{f_k}{f_{kl}} \leq 0 \tag{3.16}$$

k is the frequency and u and l are the upper and lower bounds respectively. For example the first flexible flap frequency is constrained between a lower bound 2.1 and an upper bound 2.9.

Another constraint to be used for dynamics is the blade weight.

$$b_i = \frac{W}{W_{max}} - 1 \leq 0 \tag{3.17}$$

W is the total blade weight and W_{max} is the maximum allowable weight. Typically the maximum weight will be equal to the reference blade.

Due to the large mass of the blade with a high rotation speed, the blade is subjected to high centrifugal stresses.

$$\sigma = \frac{m\Omega^2 r_{cg}}{A} \tag{3.18}$$

A is the cross sectional area of the blade and r_{cg} is the radial location of the blade's centre of gravity. The centrifugal stress must be constrained below the yield limit with a factor of safety.

$$b_i = \frac{\sigma FS}{\sigma_{yield}} - 1 \leq 0 \tag{3.19}$$

The last dynamic constrain to be imposed is the autorotation inertia. The autorotation is a self-sustained rotation of the rotor without the application of any shaft torque from the engine due to power loss. The power to drive the rotor comes from the relative upstream of air as the rotor descends through the air. Considering the case of vertical descent the buildup rate of decent is (1):

$$V_d(t) = gt\left(\frac{t}{t+\tau}\right) \tag{3.20}$$

g is the gravitational acceleration constant, t is the time after engine failure, and τ is the time constant represented as:

$$\tau = \frac{I_R \Omega_o}{Q_o} \tag{3.21}$$

Ω_o and $Q_o$are the rotation speed and torque just before engine failure respectively. The rotation inertia is given by I_R.

$$I_R = \sum_{i=1}^{NS} m_i {r_i}^2 \tag{3.22}$$

The rotation inertia is defined as the summation of the mass m of segment proportional to the square of its radial location, with NS being the number of segments of the blade.

$$b_i = 1 - \frac{I_R}{I_{R_{min}}} \leq 0 \tag{3.23}$$

In forward flight, the rotating blade on the advancing side will consume power due to the relative incoming flow. The opposite occurs on the retreating side which supplies power to the rotor. A large inertia is necessary to maintain a sufficient rotation speed to maintain lift during unpowered decent.

The first performance constraint is the power available in forward flight. The rotor power must not exceed the available power from the engines.

$$b_i = \frac{P_{req}}{P_a} - 1 \leq 0 \tag{3.24}$$

Also the power required to hover will be constrained below the power required to hover for the reference blade.

3.5. Results

This section will present the results for each of the three cases below. Each case will have different objective functions and constraints.

3.5.1.Case 1 –A Comparison Between SQP, GA, and PSO Using a Structural Optimization Example

This purpose of this section is to compare the SQP, GA, and PSO results for a simple cantilever beam with multiple cross sections experiencing similar loading conditions as a real rotor blade. The beam is 8 m in length with a height h of 8 cm and a width b of 15cm. The top and side wall thickness t_1 and t_2 respectively along with the non-structural mass (NSM) are the design variables. The beam is divided into 10 segments and has their own separate cross section dimension and nonstructural mass, for a total of 30 design variables.

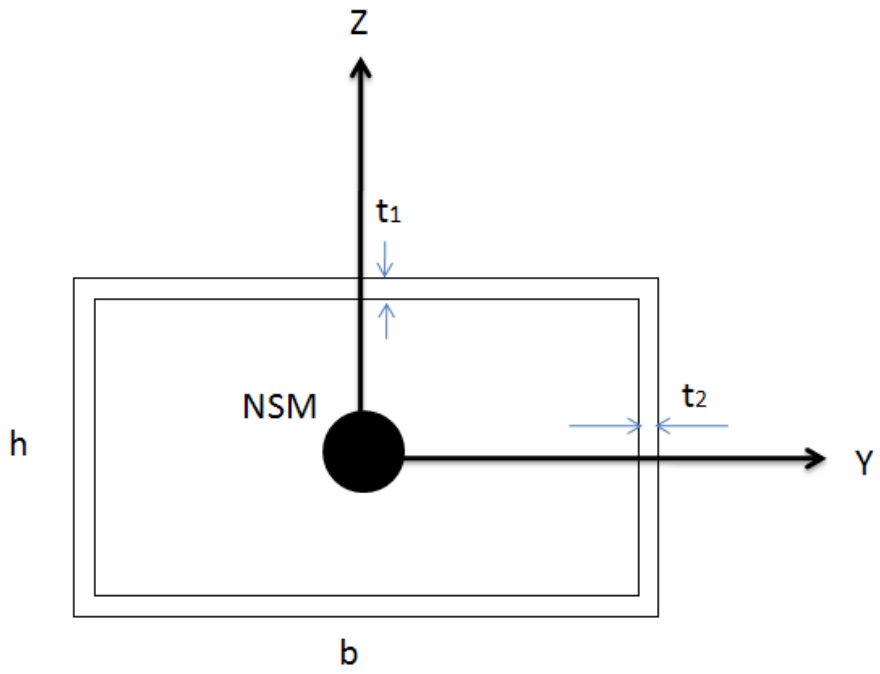

Figure 58 - Cross section profile including non-structural mass

The objective of this optimization is to minimize the mass m_T. The total mass is the summation of each segments structural mass with their respective nonstructural mass.

$$m_T = \sum_{i=1}^{N} (\rho A_i L_i + NSM_i) \tag{3.25}$$

The material density is ρ, the length of the segment is L, and the area of the cross section is A given by:

$$A_i = bh - (b - 2t_2)(h - 2t_1) \tag{3.26}$$

The upper and lower bounds on the design variables are listed in Table 3.

Table 3 - Boundary constraints imposed on design variables

Design Variable	Upper Bound	Lower Bound
NSM (kg)	3	0
t_1 (m)	0.025	0.002
t_2 (m)	0.02	0.002

Constraints were imposed on the first 2 elastic flap frequencies to avoid resonance. The frequency widows are $2.2 < \nu_1 < 2.8$ and $4.2 < \nu_2 < 4.7$. Constraints have also been imposed on the centrifugal stress:

$$\sigma_{k,c} = \frac{\sum_{i=1}^{N} m_i \Omega^2 r_i}{A_k} \tag{3.27}$$

The centrifugal stress at segment k is due to the sum of the centrifugal force outboard of the segment.

$$b_i = \frac{\sigma_{k,c}\mathrm{FS}}{\sigma_{yield}} - 1 \leq 0 \tag{3.28}$$

A factor of safety FS of 3 is being used. Two bending loads have also been applied. A flapping load and a lagging load equal in magnitude. The loads are linearly increasing from 0 N at the root to 600 N at the tip. The resultant normal stress can be represented by:

$$\sigma_{k,b} = \frac{M_f h}{2I_y} + \frac{M_l b}{2I_z} \tag{3.29}$$

M_f and M_l are the moment components for the flap and lag loading respectively. The flapping and lagging area moment of inertia are I_y and I_z respectively.

$$I_y = \frac{1}{12}(bh^3 - (b - 2t_2)(h - 2t_1)^3) \tag{3.30}$$

$$I_z = \frac{1}{12}(hb^3 - (h - 2t_1)(b - 2t_2)^3) \tag{3.31}$$

To achieve the constraint on stress, the area moments of inertia must be increased by using large thicknesses, however this will conflict with the objective to reduce the mass.

$$b_i = \frac{\sigma_{k,b}\mathrm{FS}}{\sigma_{yield}} - 1 \leq 0 \tag{3.32}$$

The final constraint to be implemented is the auto rotation inertia as described previously. The reference blade has a uniform thickness and non-structural mass distribution.

Table 4 - Reference blade cross section dimensions and non-structural mass

Reference Blade	
NSM	1 kg
t1	1.2cm
t2	0.8cm
mass	107.5 kg
AI	2.5e3 kg/m^2
b	15 cm
h	8 cm

Most blades will have a mass which considerably less, for example in ref (52), they investigated parametrically the effect of blade non-structural mass on helicopter fixed-system vibratory loads. The data was obtained with an aeroelastically scaled model rotor blades of the UH-60. Table 11 in the appendix outlines the structural properties of the 1/6th scaled rotor blade. From the table the blade

mass was estimated to be around 75kg for a full sized blade. However for the current work large reference blade mass should be sufficient for comparison of results. For an adequate comparison of the algorithms a design variable sensitivity was performed. For the SQP the optimization was performed five times with different random initial conditions, four times for the GA, and two times for the PSO. The results for the best solutions are summarized in Table 5, including the size of the populations for GA and PSO, number of iterations, and function evaluations.

Table 5 - Comparison of results for SQP, GA, and PSO

Method	Optimized Result	Size	Iteration	Function Evaluations
SQP	75.45	-	35	2260
GA	87.1	80	52	4300
PSO	79.2	200	1000 (max)	150000

The SQP algorithm gives a superior result compared to the other two. It gave the lowest mass with the fewest iterations and function evaluations. The design variable for the best SQP solution is given in Figure 59. Active constraints are in abundance for the non-structural mass and vertical wall thickness. This was to be expected since the objective is to reduced the blade mass. The non-structural mass is a dead weight used to tune the dynamics of the blade, and to increase the autorotation inertia. For the present problem, the non-structural mass not only increases the autorotation inertia but it also increases the centrifugal stress. To compensate for this increase in stress there must be an increase in the section area, therefore the thicknesses must increase. This increase will create a heavier section which will help to improve the autorotation inertia. This is evident at the radial locations 0.4, 0.7 and at the tip. Where there is an increase in non-structural mass there is also an increase in the horizontal wall thickness (this is also true for the vertical wall thickness at 0.7). The vertical wall thickness fluctuates for the majority of the middle of the blade with a slight increase at the root to meet the bending stress constraint. The beam base is almost twice the length of the beam's height thus the area moment of inertia will be considerably larger, therefore the influence of the vertical wall in the middle segment is minimal where the moment will be small compared to the root. (Figure 59 next page)

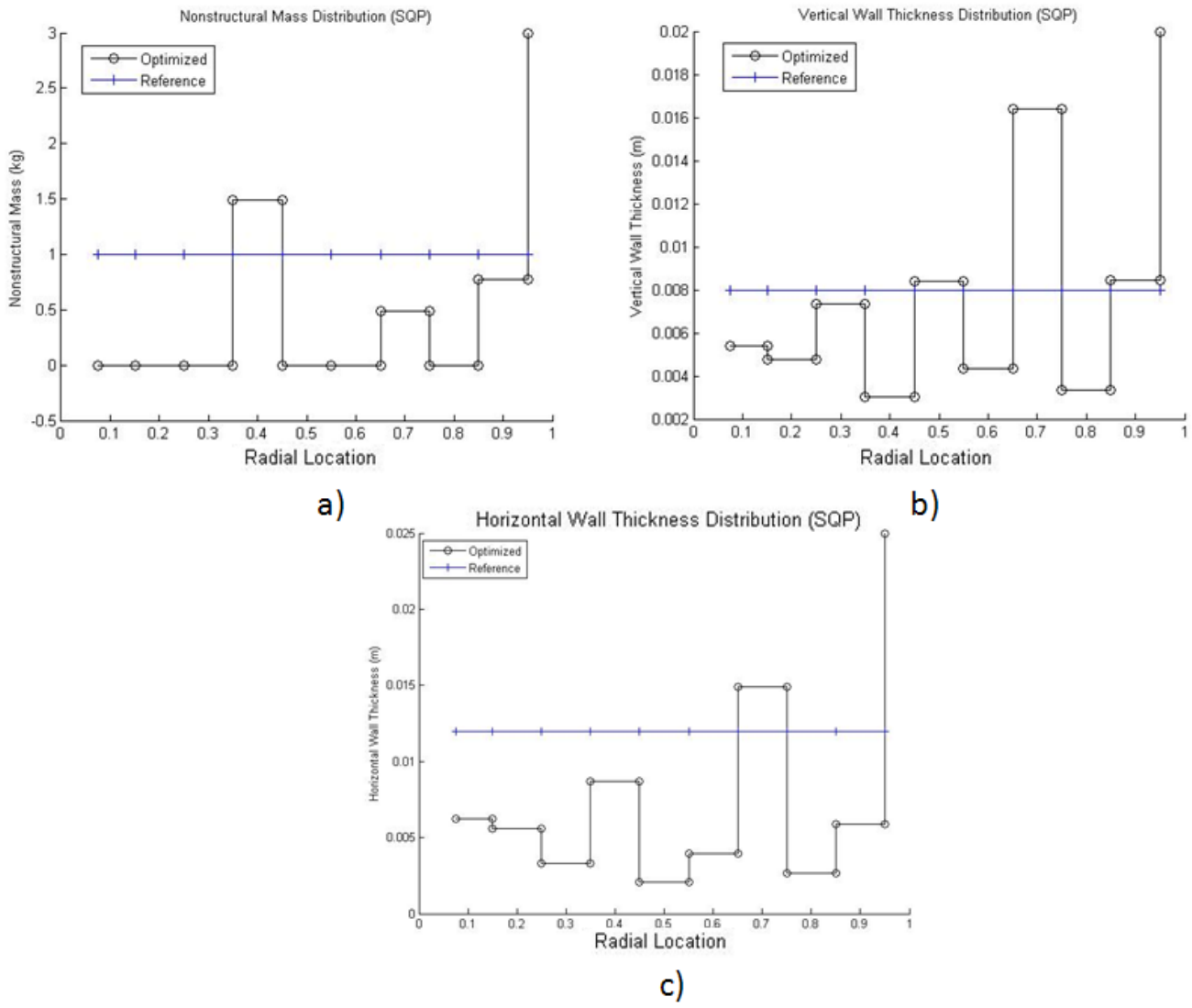

Figure 59 – SQP Spanwise distribution of a) non-structural mass b) vertical wall thickness c) horizontal wall thickness

The results for each of the cases for the SQP are in Table 12 in the appendix. The results were quite interesting. For each case the final optimum mass was the same within a few digits, with the average being 75.45. A close inspection of the design variables show that there is an inconsistency, which would suggest a local minimum. The final values for the design variables for the first two segments were the same for each case; the same was true for the tip. The middle segments had design variable values that varied. For a global minimum one should expect the design variables to be the same within a certain tolerance, but this is clearly not the case.

The results for the GA are presented in Figure 60. The GA produced the worst results of the three algorithms tested. This could be rectified by increasing the population size and reducing the design variable bounds. The results are similar to the SQP; the blade tip has the largest non-structural mass with thick walls for the structure. This is necessary to satisfy the autorotation constraint. The most obvious difference between the two results is the distribution of the non-structural mass between the root and 0.5 radial location, and the large vertical wall thickness at the root for the GA. The walls are thick to help satisfy the autorotation inertia. By shifting the majority of the total mass of the blade inboard the centrifugal stress at the inboard sections will be reduced. Between 0.3 and 0.7 the horizontal thickness is relatively thick with the exception of 0.5. This is necessary to satisfy the bending stress, and with the low horizontal thickness at 0.5, there is a sudden increase in the vertical thickness at 0.5. The large surface area at 0.7 is essential to reduce the centrifugal stress caused by the very heavy blade tip.

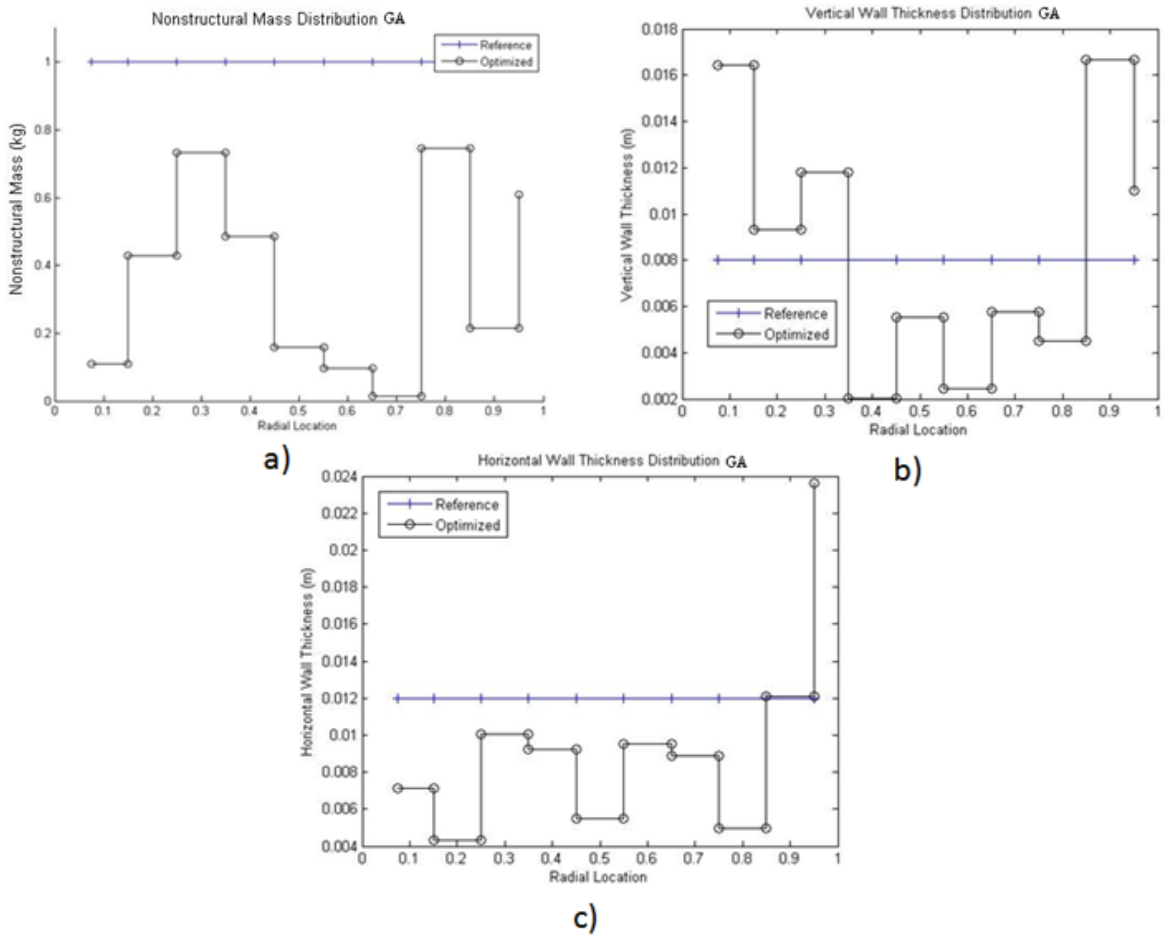

Figure 60 - GA Spanwise distribution of a) non-structural mass b) vertical wall thickness c) horizontal wall thickness

The results for the PSO algorithm are shown in Figure 61. The horizontal and vertical wall thicknesses exhibit similar trends; the horizontal thicknesses are greatest at the middle segments of the blade with lower vertical thicknesses, and the tips receive the greatest thickness. Also it is important to note that where there is a drop in the horizontal wall thickness, there is a peak in vertical wall thickness to satisfy stress constraints. A similar pattern emerges when there is a drop in vertical thickness as well. The non-structural mass has a different pattern compared to the other to algorithms. There is zero mass at the root section and then there is a gradual increase up to the tip. The non-structural mass drops when there is an increase in vertical thickness.

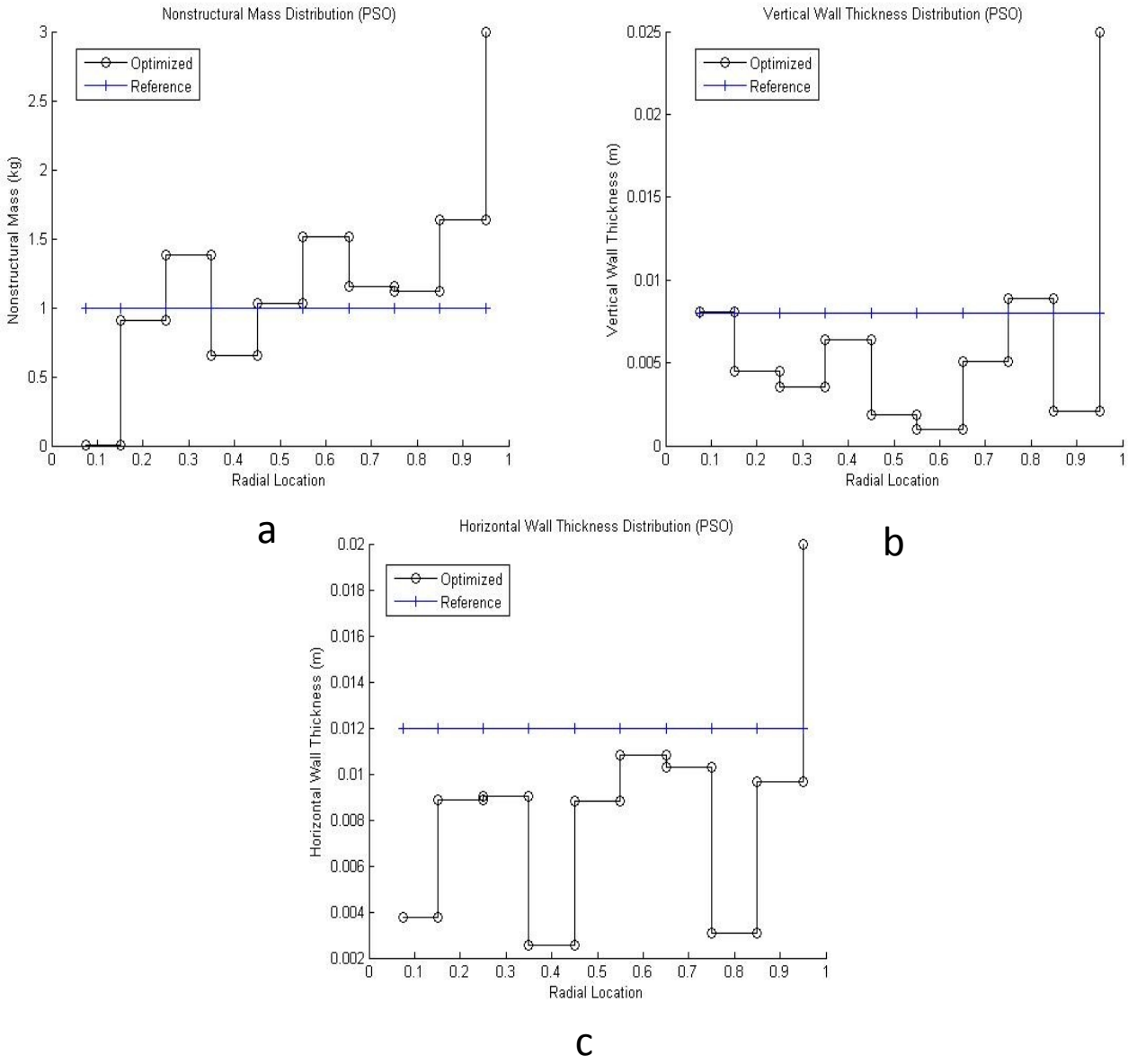

Figure 61 - PSO Spanwise distribution of a) non-structural mass b) vertical wall thickness c) horizontal wall thickness

The above results are decent but improvements can be made to the SQP results. It was pointed out that the design may have reached a local minimum. There are two possible methods to improve the results: use a hybrid approach or a multi-objective optimization routine. The hybrid approach will be used for the current work. A common hybrid method uses an evolutionary algorithm to solve for an optimal design which is then followed by a gradient optimizer to refine the results. For this example the opposite approach will be used. The results from the SQP method were the reference point to create new upper and lower bounds for the design variables. A +/- 50% was applied to the optimal SQP design. Using this approach the mass was reduced from 77.45 to 73.2, which is a substantial improvement. The new mass and thickness distributions are presented in Figure 62. The non-structural mass and horizontal wall thickness shows a decrease in the middle sections. There is a slight increase in horizontal wall thickness at the root to maintain the stress constraints, also at 0.3 and 0.5 there is a large increase in the vertical wall thickness to improve the centrifugal stress constraint.

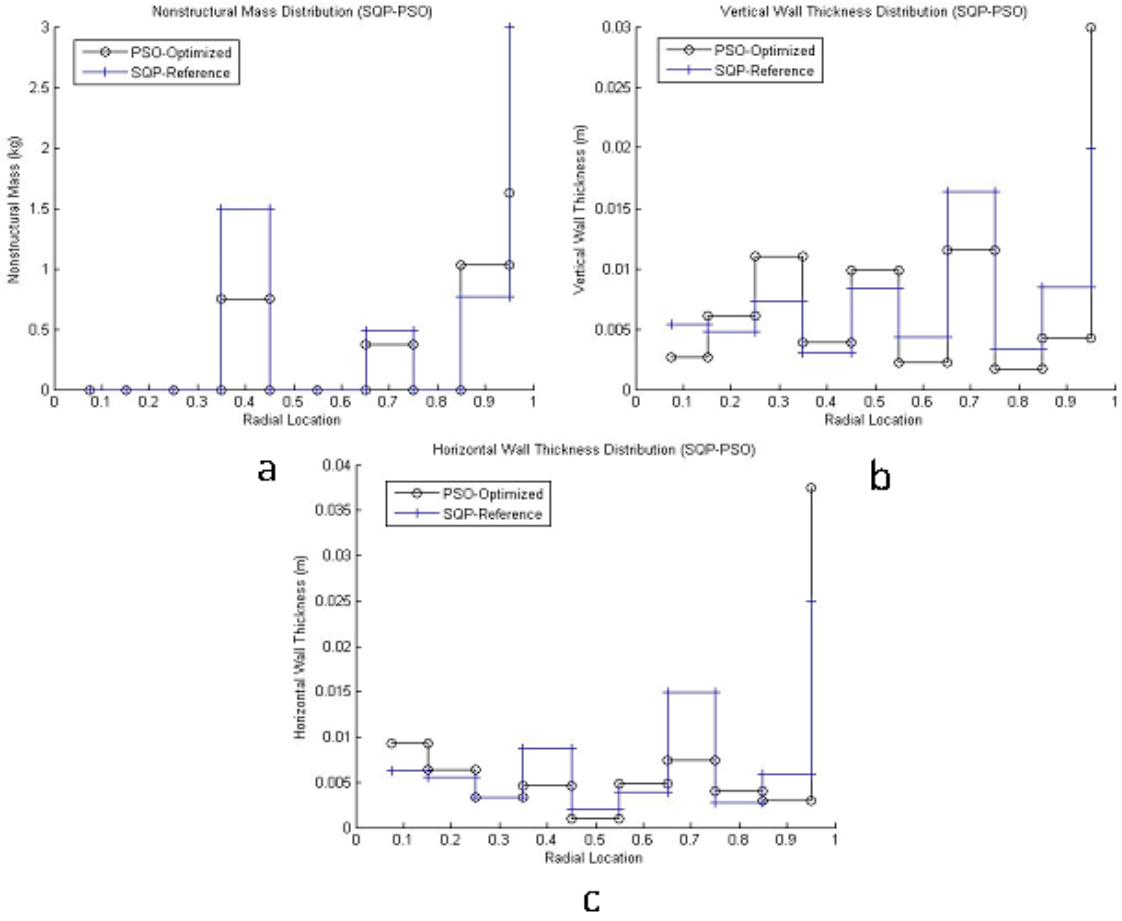

Figure 62 - Combined SQP-PSO Spanwise distribution of a) non-structural mass b) vertical wall thickness c) horizontal wall thickness

It is important to note that for each case the autorotation constraint was active. This was expected since the objective was to reduce blade mass. The objective and constraint are conflicting and trade offs will be required during the optimization to achieve an optimum solution. The example analyzed here was a simplification of a rotor blade. Simple linear beam theory was used to calculate stress on a hollowed rectangular beam. The objective was to reduce the blade mass using the SQP, GA, and PSO algorithms.

3.5.2.Case 2 – Minimization of Hub Vertical Shear

For this case a coupled aerodynamic and dynamic optimization will be employed to minimize the hub vertical shear for an articulated rotor. The vertical shear is a strong contributor to vibrations. The analysis was performed using an SQP algorithm. The PSO and GA were omitted since from the previous case, it showed to be time consuming. Table 6 below lists the fixed parameters for the rotor geometry and flight conditions. The blade radius, shaft angle and number of blades are the same values used for the UH-60. The weight coefficient that was used for trim validation was also kept constant. The advance ratio of 0.25 was selected. From the validation of the power coefficient, an advance ratio of 0.25 was the closest to the published results. The non-structural mass and the mid-span cross section dimensions were removed since from the previous case proved to be difficult for a gradient based algorithm. The spar width and height percentage of chord at the root were also kept constant.

Table 6 - Fixed parameters for rotor geometry and flight condition

Fixed Parameters			
Rotor Geometry		**Flight Conditions**	
Blade Radius	8.18 m	Flight Path Angle	4 deg
Shaft Angle	3 deg	Advance Ratio	0.25
Number of Blades	4	Weight Coefficient	0.0065
Hinge Offset	0.05	Sea Level Density	1.225 kg/m^3
Spar Width	33 %chord		
Spar Height	9.5 %chord		
NSM	0		

The design variables include the section centre of gravity, blade twist, chord length, cross section thicknesses at the root and tip. To incorporate a taper into the structure the base and height of

the blade tip were included as design variables (The aerodynamic loads were calculated assuming a rectangular balde). Table 7 lists the upper and lower bounds place on the design variables.

Table 7 - Upper and lower bounds placed on design variables

Design Variable	Upper Bound	Lower Bound
Section Centre of Gravity (%chord)	0.1	-0.2
Twist (deg/m)	-10	-18
Chord (m)	0.65	0.3
Root Thickness (t_1) (m)	0.025	0.001
Root Thickness (t_2) (m)	0.025	0.001
Tip Thickness (t_1) (m)	0.025	0.001
Tip Thickness (t_2) (m)	0.025	0.001
Tip Base (%chord)	33.33	20
Tip Height (%chord)	9.5	5

Constraints were imposed on the first two elastic flap rotating natural frequencies, the autorotation inertia, the power required for forward flight must not exceed the power available, the power required to hover must not exceed the power required from the reference blade, and there was a constraint placed on centrifugal stress. The centrifugal stress constraint is the same as the first case presented earlier, with one exception. Only the centrifugal stress at the root will be determined since the section geometry is just a linear taper. Since the rotor blade is articulated there will be no bending moment at the root, hence no bending stress. Constraints were also imposed on the blade tip cross-section dimensions to avoid a negative area.

The objective function is a function of azimuth angle. To create a singular objective it was necessary to sum the vertical shear over the azimuth:

$$f(x) = \frac{sum(S_z)}{sum(S_{z,ref})} \tag{3.33}$$

The optimization process was performed using an SQP algorithm, and a 33.6% reduction in the objective function was obtained. Table 8 lists the results of both the reference and optimal blade. (Table 8 next page)

Table 8 - Comparison between reference blade and optimal

Design Variables	Reference Blade	Optimized Blade	% Change
Twist	-16	-17.5	9.37
Chord (m)	0.527	0.606	15
Section Centre of Gravity (%chord)	-0.05	-0.1089	117.8
Root Thickness (t_1) (m)	0.02	0.0181	-9.5
Root Thickness (t_2) (m)	0.02	0.005	-75
Tip Thickness (t_1) (m)	0.01	0.0115	15
Tip Thickness (t_2) (m)	0.01	0.0249	149
Tip Base (%chord)	0.25	0.0249	29.9
Tip Height (%chord)	0.08	0.0943	17.88
Other Performance Measures			
Blade Centre of Gravity (m)	3.7126	4.1674	12.25
Autorotation Inertia (kgm^2)	1.973e6	3.273e6	65.7
Hover Power (W)	1.2715e6	1.2606e6	-0.86
Forward Power (W)	1.755e6	1.4322e6	-18.4
Rigid Flap Frequency /rev	1.0602	1.067	0.64
First Flexible Flap Frequency /rev	2.3725	2.641	11.3
Second Flexible Flap Frequency /rev	4.386	3.914 (infeasible)	12.04
Mass (kg)	106.83	146.19	36.84
Centrifugal Stress	4.268e7	6.469e7	51.57
Vertical Shear (N)	***5.2248e3***	***3.468e3***	***-33.6***

The blade twist was increased and in order to satisfy the hovering power constraint. A high twist will improve the hovering efficiency; however the larger chord, hence larger solidity, would decrease hover performance. This larger solidity is required to decrease the forward flight power. The autorotation inertia has a substantial increase due to the very large increase in blade mass. The blade centre of gravity shifts outward which creates in combination with the greater mass, a higher centrifugal stress. However the stress is well below the yield limit. A plot of the azimuthal variation of the vertical shear at the hub is shown Figure 63.

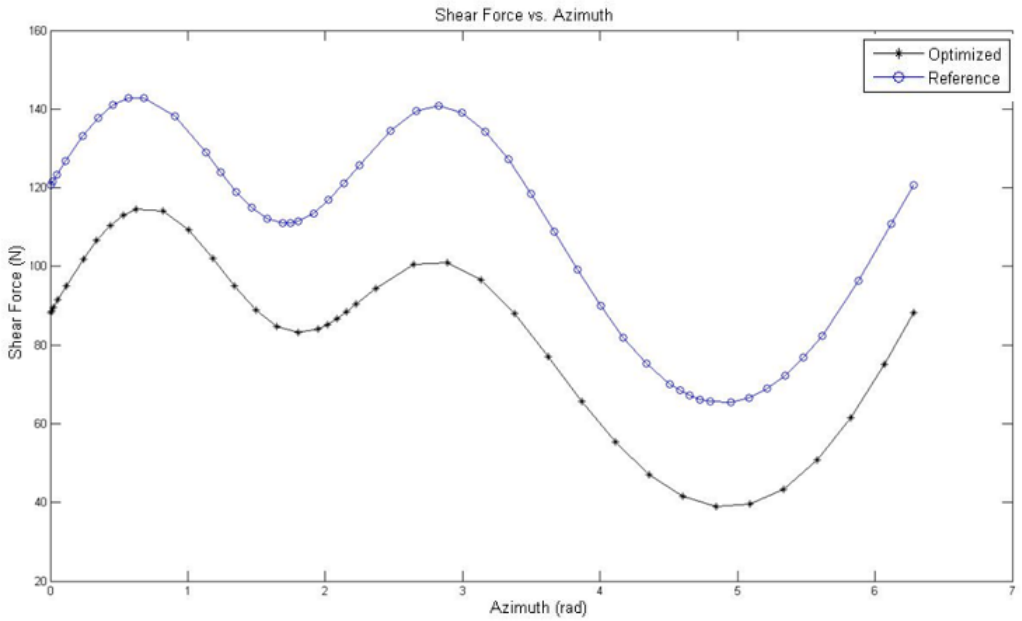

Figure 63 - 4/rev vertical shear for both the reference and optimal blades

The plot of the shear force against the azimuth angle shows a substantial reduction in the shear for each azimuth station. The large mass increases the blade inertia which reduces the net loading along the blade. A contour plot of both the optimized and reference blade is presented in Figure 77 and Figure 78 respectively in the appendix. This high mass is also evident in the flap response:

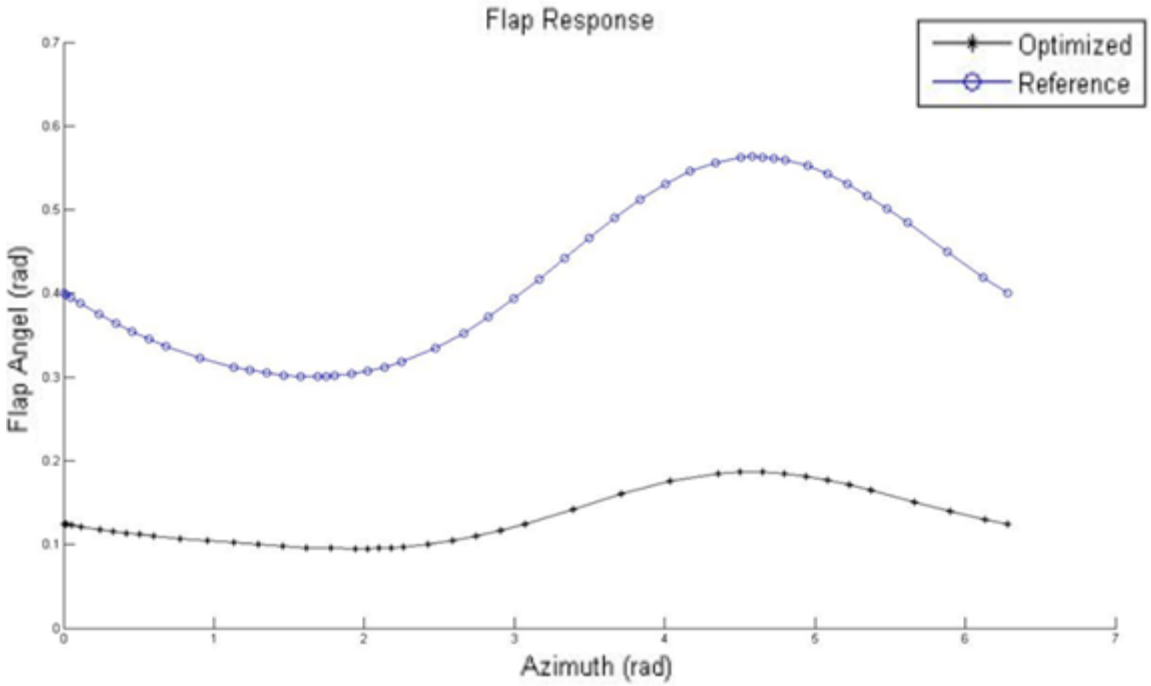

Figure 64 - Flap response for both optimized and reference blade

There is significant reduction in the flap angle. Also to further decrease the flap response the section centre of gravity was moved closer towards the leading edge of the blade. This decrease in flap response also translates to the flapping rate:

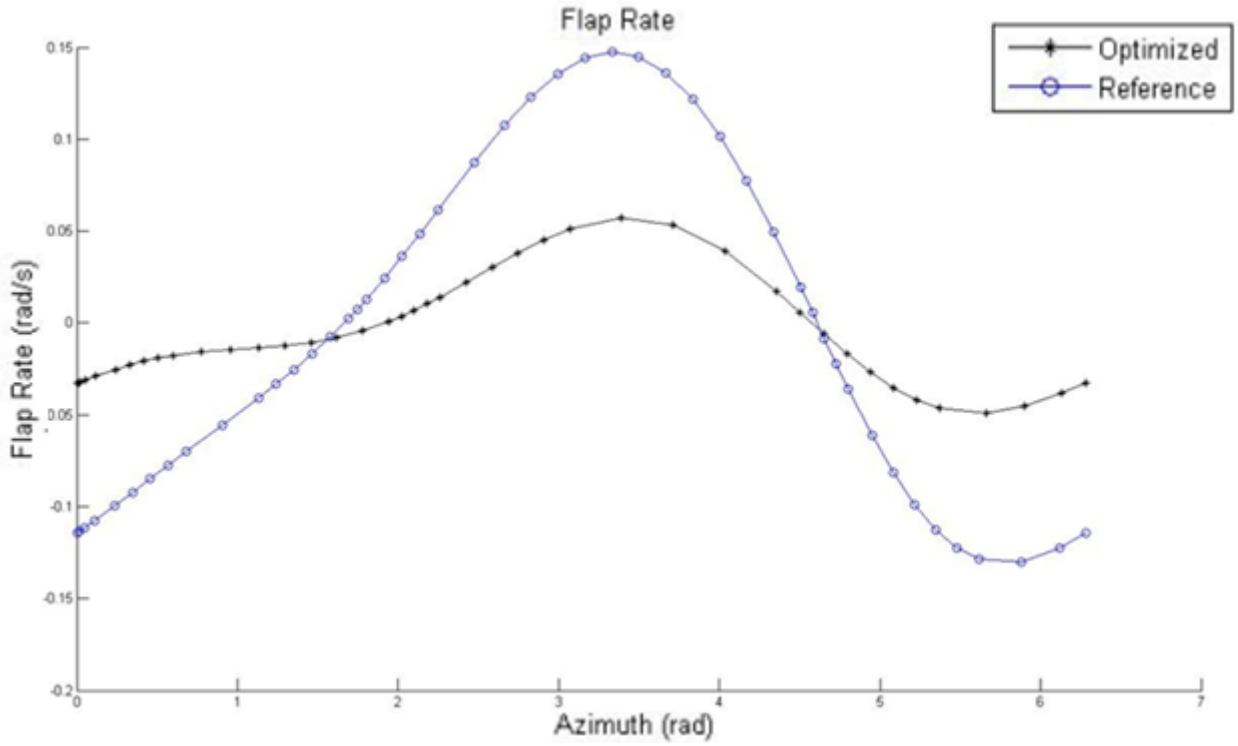

Figure 65 - Flap rate for both optimized and reference blade

There is a reduction in the flap rate, which will reduce the perpendicular velocity, hence induced angle of attack. This smaller induced angle will influence the effective angle of attack, hence the blade aerodynamic loading. The mass distribution is presented in Figure 66. The mass at the root is increased compared to the reference slightly and the tip received the largest increase.

(Figure 66 next page)

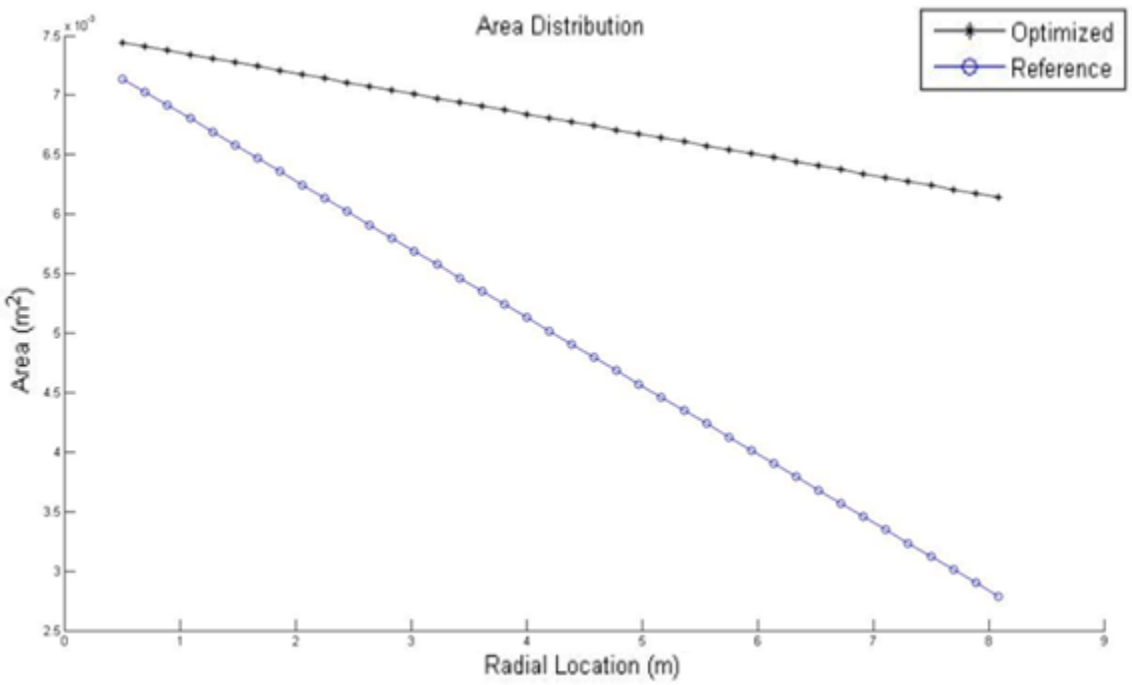

Figure 66 - Mass distribution for both the optimized and reference blade

This increase at the tip can be examined by comparing the optimized blade and reference blade cross section geometry in Figure 81 and Figure 82 respectively in the appendix. Both the height and base lengths increased as well as the thickness of the horizontal and vertical wall. This increase at the tip was necessary to improve the objective function as well as to satisfy the autorotation inertia constraint. The root cross sections are presented in Figure 79 and Figure 80 for the optimized and reference blade respectively. The base and height both increase due to the larger chord length, but the thicknesses decrease. Even with the decrease in thickness there is an increase in area which contributes to the reduction of centrifugal stress. The objective function was reduced primarily because of the large increase in mass. This was due to the insufficient constraints placed on the blade mass. The hub vertical shear and autorotation inertia forced the optimizer to create a heavier structure near the blade tip. The centrifugal stress was a weak constraint since the reference blade satisfied the constraint very well. Even with an increase in stress of 51%, the constraint was still satisfied. If a constraint had been placed on the blade mass, by trying to keep it below the reference blade, it is highly likely that the constraint would be active. Thus forcing the aerodynamic design variable to decrease the aerodynamic loading. For an improved optimization result more constraints would be needed. This will be addressed in case 3.

3.5.3.Case 3 – Minimization of Hub Vertical and Radial Shear

The final optimization case will improve on the results from case 2 by incorporating the radial shear into the objective function. This is necessary since case 2 was biased towards the mass of the blade. From the radial shear equation, a large mass will increase the shear at the hub:

$$S_r = \int_0^R \left(F_r + m\Omega^2 r - 2\Omega\eta_\xi \dot{\xi} m\right) dr \tag{3.34}$$

The lag rate $\dot{\xi}$ of the blade also contributes to the radial shear, but for the current work only the flap motion was considered, so the lag rate was set to zero. The objective function is formulated as follows:

$$f(x) = \frac{sum(S_z)}{sum(S_{z,ref})} + \frac{sum(S_r)}{sum(S_{r,ref})} \tag{3.35}$$

It is the summation of the two objectives. Table 9 lists the comparison between the current optimized blade to that of the case 2 and the reference blade. The incorporation of the radial shear into the objective function made a significant change to the design of case 2.

Table 9 - Comparison between results from Case 3 to Case 2 and Reference blade designs

Design Variables	Optimized Blade	% Change (Case 2)	% Change (Ref)
Twist	-18 (active)	2.85	12.5
Chord (m)	0.3883	-35.92	-26.3
Section Centre of Gravity (%chord)	-0.0742	-31.8	48.4
Root Thickness (t_1) (m)	0.0099	-45.3	-50.5
Root Thickness (t_2) (m)	0.025 (active)	400	25
Tip Thickness (t_1) (m)	0.0145	26.08	45
Tip Thickness (t_2) (m)	0.025 (active)	0.4	150
Tip Base (%chord)	0.333 (active)	2.6	33.3
Tip Height (%chord)	0.0902	-4.3	12.75
Other Performance Measures			

Blade Centre of Gravity (m)	4.406	5.27	18.7
Autorotation Inertia (kgm^2)	1.9872e3	-39.3	0.68
Hover Power (W)	1.2715e6 (active)	0.86	0
Forward Power (W)	1.3981e6	-2.4	-20.3
Rigid Flap Frequency /rev	1.07	0.28	0.92
First Flexible Flap Frequency /rev	2.769	4.8	16.7
Second Flexible Flap Frequency /rev	4.6217	5.4	18
Mass (kg)	81.33	-44.3	-23.86
Centrifugal Stress	8.384e7	29.6	96.4
Vertical Shear (N)	***3.445e3***	***-0.66***	***-34.06***
Radial Shear (N)	***2.385e3***	***-38.5***	***-17.87***

The introduction of the radial shear was able to improve the design significantly. There was an improvement in both the vertical and radial shear compared to the reference and case 2 blades.

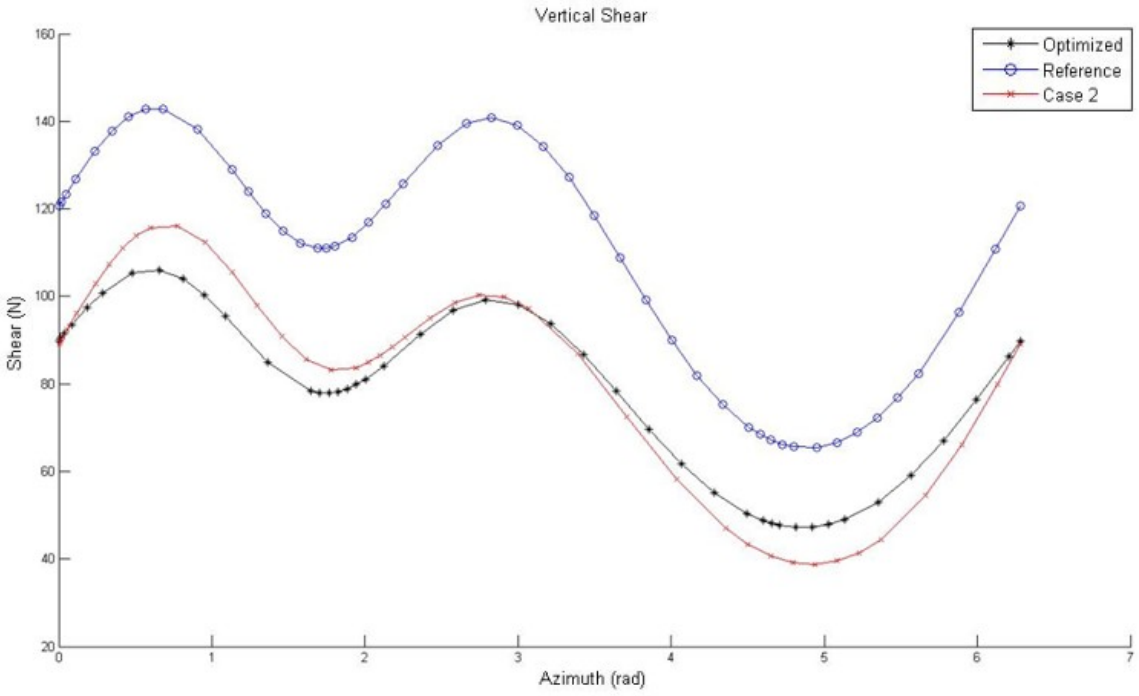

Figure 67 - Vertical Shear for optimized, reference, and case 2 blades

There is a decrease in the shear on the advancing side of the disk but there is slight increase in vertical shear on the retreating side compared to case2. The sum total of the vertical shear for the current case

was only 0.66% smaller compared to case 2 and can be considered to be negligible. The radial shear was constant for each azimuth station:

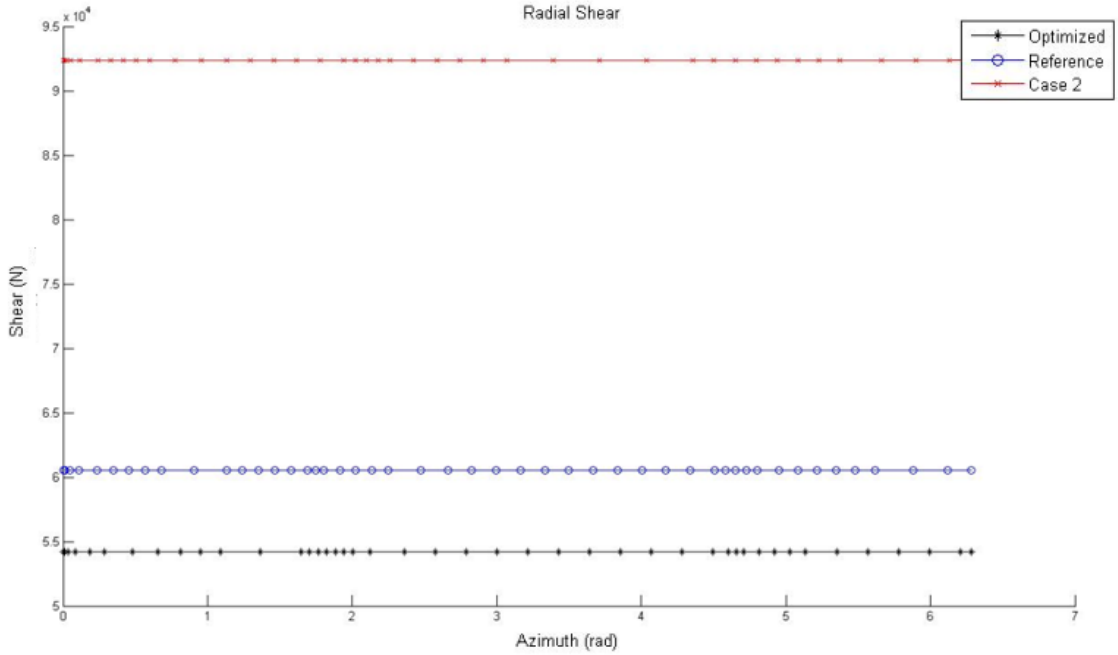

Figure 68 - Radial shear for optimized, reference, and case 2 blades

The radial shear equation is a summation of the normal force radial component and centrifugal force. The normal force component is much smaller than the centrifugal, and with a constant rotation speed the centrifugal force also remains constant. The blade mass distribution exhibited a different trend compared to the other two designs.

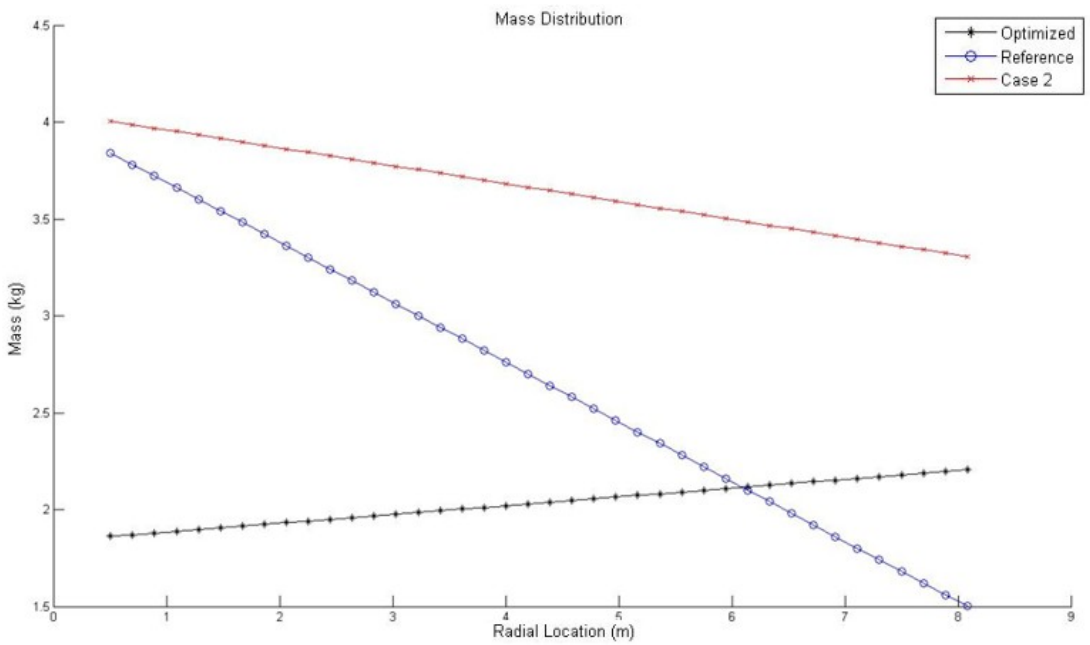

Figure 69 - Mass distribution for the optimized, reference, and case 2 blades

The mass linearly increase from the root to the tip. This was required to satisfy the autorotation inertia. This does force the centre of gravity to be shifted outward and thus increases the centrifugal stress. However the stress is well below the yield limit with a factor of safety. The vertical thicknesses for both the tip and the root were active with the upper bound. The cross sectional dimensions are important for several reasons: the area is directly related to the mass of the segment, a larger area will reduce the blade stress, and the area moment of inertia. The area moment is plotted in Figure 70.

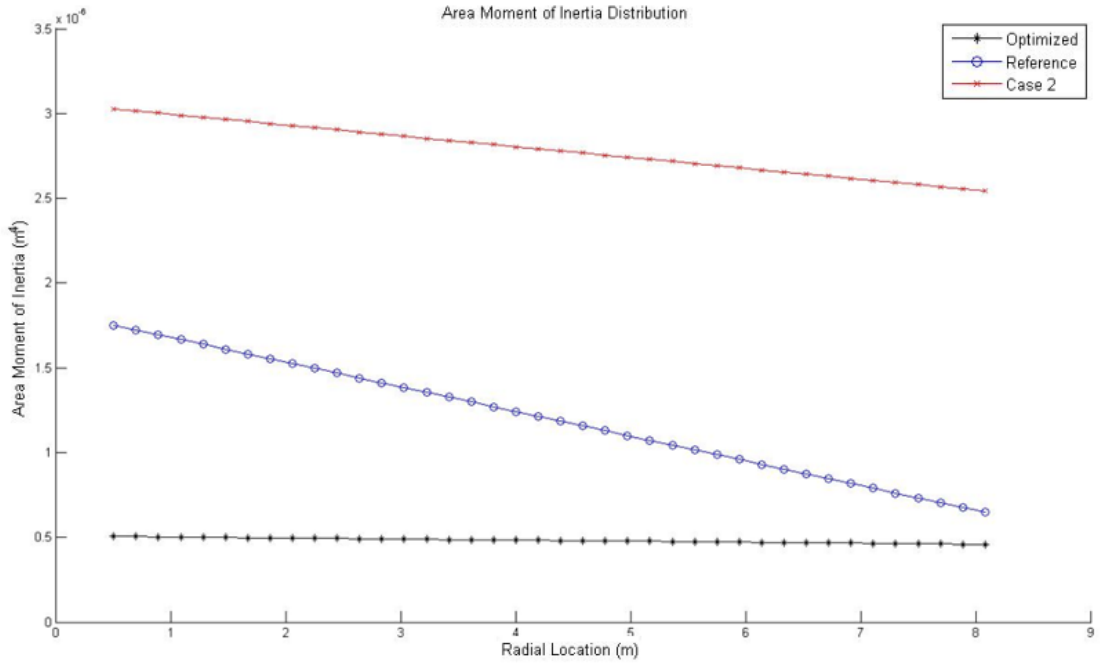

Figure 70 - Area moment of inertia distribution

For the optimized blade the inertia distribution is almost constant. The blade base and height is almost constant along the span, with the only variation in the cross section being the thicknesses. The flap response is presented in Figure 71.

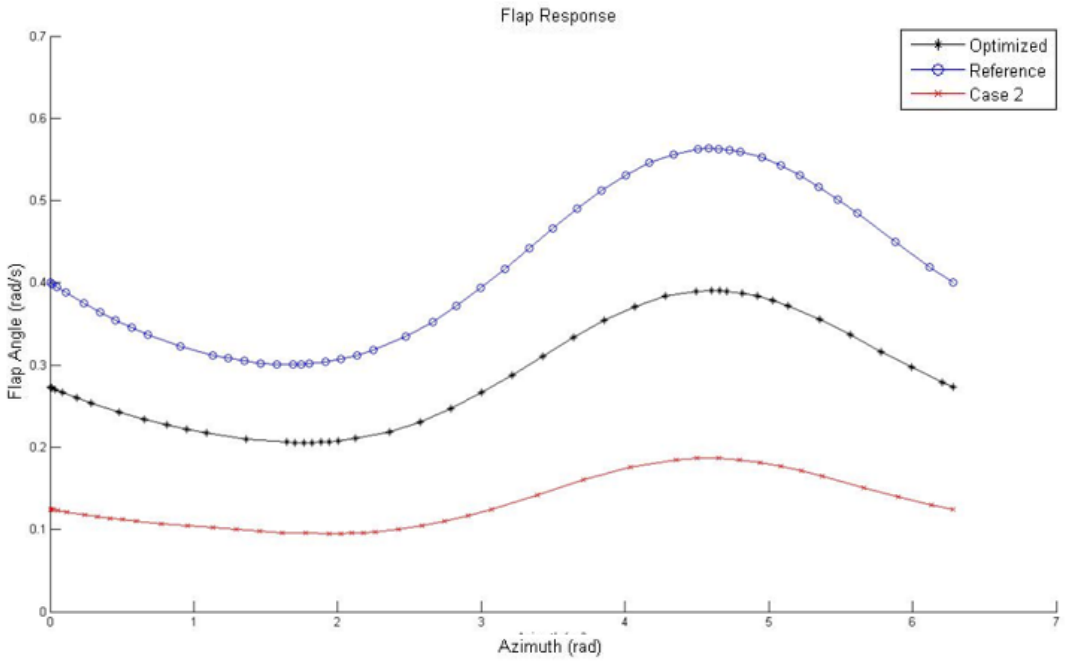

Figure 71 - Flap response for the optimized, reference, and case 2 blades

The optimized blade has a reduction in the flap response compared to the reference, but there is an increase compared to case 2. This was expected since; with a lighter blade the flap angle would be greater, a smaller chord would produce a lower lift and result in a lower flap angle, and the centre of gravity being shifted only 18.7% towards the leading edge would increase the flap angle compared to case 2. The combination of both the vertical and radial shear force, forces a compromise between the two objectives. The radial force requires a smaller section mass where the vertical shear requires a larger one. With this conflict the aerodynamic design variables will contribute more towards the solution since the aerodynamic loading must be reduced to improve the vertical shear, hence the smaller chord and larger twist rate. In summary the third case was an improvement over the second due to the addition of the radial shear to the objective function.

Chapter Four - Conclusion and Recommendations

The helicopter rotor is highly a multidisciplinary engineering problem with its coupling between aerodynamics, dynamics, and structures. For the current work three cases were examined to optimize a rotor blade with increasing complexity. The first case was the simplest. It was a structural design optimization of a cantilever beam using an SQP, GA, and PSO algorithm. The beam was subjected to a static centrifugal load, and a linearly increasing flap and lag bending load. The cross sectional thicknesses and non-structural mass at ten spanwise locations were the design variables. Constraints were imposed on the rotating natural frequencies, and centrifugal and bending stress, and autorotation inertia. The SQP algorithm resulted in the superior design but a local minimum was present. An improvement in the objective was achieved by introducing a hybrid approach where the optimal SQP solution was used as a stating boundary for a PSO. The second case was performed to introduce the multidisciplinary nature of the helicopter rotor into the design optimization process by including aerodynamics and dynamics. The objective was to reduce the hub vertical shear. The non-structural masses and mid-span cross sectional dimensions were removed as design variables. Only the root and tip thicknesses were kept. The GA and PSO from the first case proved to be time consuming so only the SQP algorithm was used. The objective was reduced significantly due to the large increase in blade mass. Due to the insufficient constraints placed on the blade mass. The third case was created to address the issue with the blade mass from case 2 by introducing the radial shear force into the objective function. With the same constraints and design variables the design was improved significantly. There was a decrease in the vertical and radial shear. There was a substantial decrease in the blade mass which forced the aerodynamic design variables to influence the design more, compared to the second case. Also the power required in forward flight decreased.

The analysis was performed with the tool boxes available from MATLAB. The accuracy of the model is as only as accurate as the computer model being used. A rigid body flap with linear inflow was used to model the dynamics and aerodynamics. This is a simple model and it requires improvement. A more accurate model will be required which can take into account the flexible flap-lag-torsion dynamics, unsteady aerodynamics, and a wake model that can determine the nonlinearities of the wake induced field. Such a model will be more computationally demanding and if performing an optimization routine

one must be prepared to wait several days or even weeks to get a result if using a multiprocessor desktop computer.

With regards to the algorithms, the SQP method is by far the fastest for execution, however local minimums will likely occur for nonconvex problems. The GA required fewer iterations than the PSO, but it is highly sensitive to the initial diversity of the problem. It is recommended that the GA be used when the designer knows where the optimal design variables will most likely be in the design space, hence smaller side constraints on the design variables. The PSO is a relatively new algorithm. When it comes to calculating the new population (swarm) for the next iteration, it is much faster than the GA, but it would require more iterations to converge and possible larger population size. With discipline codes that can take several hours or minutes to compute, a PSO might not be the best algorithm to use, if time is of importance. The PSO is still in development and perhaps in the future better searching of the design space may be possible.

References

1. **Leishman, J Gordon.** *Principles of Helicopter Aerodynamics 2nd ed.* New York, NY : Cambridge University Press, 2006.

2. *Static Thrust Analysis of the Lifting Airscrew.* **Knight, Montgomery and Hefner, Ralph A.** 1937, NACA TN 626.

3. **Johnson, Wayne.** *Helicopter Theory.* New York : Dover Publications, Inc, 1994.

4. *The Fluid Dynamics of Rotor Wakes: Theory, Computation and Experiment (Invited).* **Conlisk, A T.** AIAA 99-3421.

5. *The Wake Geometry of a Hovering Rotor and Its Influence on Rotor Performance.* **Landgrebe, A. J.** 4, 1972, Journal of the American Helicopter Society, Vol. 17, pp. 3-15.

6. *A Prescribed Wake Lifting Surface Hover Performance Analysis.* **Kocurek, J. David and Tangier, James L.** 1, 1977, Journal of the American Helicopter Society, Vol. 22, pp. 24-35.

7. *Application of Modern Hydrodynamics to Aeronautics.* **Prandtl, Ludwig.** s.l. : NACA Technical Report 116, 1921.

8. **Anderson, Jr, John D.** *Fundamentals of Aerodynamics 3rd ed.* New York, NY : McGraw-Hill, 2001. 0-07-237335-0.

9. *A Semi-Empirical Model for Dynamic Stall.* **Leishman, J G and Beddoes, T S.** 1989, Journal of the American Helicopter Scociety.

10. **Watkinson, John.** *The Art of the Helicopter.* Linacre House, Jordan Hill, Oxford OX2 8DP : Elsevier Butterworth-Heinemann, 2004.

11. *Structural Behavior of Thin and Thick Walled Composite Blades with Multi-Cell Sections.* **Sung Nam Jung, V.T. Nagaraj.** 2002, AIAA.

12. *Rotary-Wing Aeroelasticity: Current Status and Furture Trends.* **Friedmann, Peretz P.** 10, 2004, AIAA, Vol. 42.

13. *Survey of Recent Devlopments in Rotorcraft Design Optimization.* **Ganguli, Ranjan.** 3, 2004, Journal of Aircraft, Vol. 41.

14. *A Theory of Airflow Through Rotors and Its Application to Some Helicopter Problems.* **Drees, J M.** 2, July-Sept. 1949, J. of the Helicopter Association of Great Britain, Vol. 3, pp. 79-104.

15. **Glauert, H.** A General Theory of the Autogiro. s.l. : ARC R&M 1111, 1926.

16. *A Critical Assesment of the UH-60 main Rotor Blade Airfoil Data.* **Totah, Joesph.** 1993, AIAA.

17. *A Critical Assessment of Wind Tunnel Results for the NACA0012 Airfoil.* **McCroskey, W. J.** October 1987, NASA TM 1000 19.

18. *Closed-Form Equations for the Lift, Drag, and Pitching-Moment Coefficients of Airfoil Sections in Subsonic Flow.* **Smith, R. L.** 1978, NASA TM-78492.

19. *Aerodynamic Characteristics of Three Helicopter Rotor Airfoil Sections atReynolds Numbers From Model to Full Scale at Mach nhmbers From 0.35 to 0.90.* **Noonan, Kevin W. and Dingham, Gene J.** 1980, NASA TP-1701.

20. *Effect of Helicopter Blade Dynamics on Blade Aerodynamic and Structural Loads.* **Heffernan, Ruth M.** 1987, Presented at the AIAA Dynamics Specialists Conference held in Monterey, Calif.

21. *Flap-Lag-Torsion Stability in Forward Flight.* **Panda, Brahmananda and Chopra, Inderjit.** Moffet, Calif : Presented at the Second Decennial Specialists' Meeting on Rotorcraft Dynamics, NASA Ames Research Centre, 1984.

22. **Mathworks.** *Matlab's User Manual R2010a.*

23. *Performance Analysis of a Utility Helicopter with Standard and Advanced Rotors.* **Hyeonsoo, Yeo, Bousman, William G. and Johnson, Wayne.** San Francisco, CA : Presented at the American Helicopter Society Aerodynamics, Acoustics,and Test and Evaluation Technical Specialist Meeting, 2002.

24. *A Mathematical Model of the UH-60 Helicopter.* **Hilbert, Kathryn B.** s.l. : NASA Technical Memorandum , 1984. 85890.

25. *Aerodynamic Characteristics of SC1095 and SC1094 R8 Airfoils.* **Bousman, William G.** s.l. : NASA/TP–2003-212265, AFDD/TR-04-003, 2003.

26. *Rotorcraft Aerodynamics Models for a Comprehensive Analysis.* **Johnson, W.** Washington DC. : American Helicopter Scociety 54th Annual Forum Proceedings, 1998.

27. *Flight Testing of the UH-60A Airloads Aircraft.* **Kufeld, R. M., et al., et al.** Washington DC : American Helicopter Society 50th Annual Forum Proceedings, 1994.

28. *The Free Wake Analysis-A Method for the Prediction of Helicopter Rotor Hovering Performance.* **Clark, David R. and Leiper, Albert C.** s.l. : Presented at the 25th National Forum of the American Helicopter Scociety, 1969.

29. *A Comprehensive Analytical Model of Rotorcraft Aerodynamics and Dynamics.* **Johnson, W.** 1980, NASA TM 81183.

30. *Multidisciplinary Design Optimization: An Emerging New Engineering Discipline, in Advances in Structural Optimization.* **Sobieszczanski-Sobieski, J.** 1995, J. Herskovits (Ed.), KLUWER A.P., Dordrecht,, pp. 483-496.

31. *Minimum Weight Design for RotorCraft Blades with Multiple Frequency and Stress Constraints.* **Chattopadhyay, Aditi and Walsh, Joanne L.** 1988, Technical Memorandum 100569.

32. *Structural Optimization of Rotor Blades with Integrated Dynamics and Aerodynamics.* **Chattopadhyay, Aditi and Walsh, Joanne L.** 1989, NASA Technical Memorandum 101512.

33. *Optimum Design of Helicopter Rotor Blades with Multidisciplinary Couplings.* **Chattopadhyay, Aditi and McCarthy, Thomas R.** 1992, AIAA.

34. *Application of Design Optimization Techniques to Rotor Dynamics Problems.* **Davis, Mark W. and Weller, William H.** Washington, DC : s.n., 1986. Presented at the 42nd Annual Forum of The American Helicopter Society.

35. *Multidisciplinary Optimization of Helicopter Rotor Blades Including Design Variable Sensitivity.* **McCarthy, Thomas R. and Chattopadhyay, Aditi.** Cleveland, OH : s.n., 1992. Fourth AIAA/USAF/NASA/OAI Symposium on Multidisciplinary Analysis and Optimization.

36. *Systemic Control Design by Optimizing a Performance Index.* **Kreisselmeier, G and Steinhauser, R.** 1979. Proceedings of Internationa Federation of Active Controls Symposium on Computer Aided Design of Control Systems. pp. 113-117.

37. *Optimization of Rotor Blades for Combined Structural, Dynamic, and Aerodynamic Properties.* **He, C. and Peters, D. A.** San Francisco, CA : s.n., 1990. Proc., Third Air Force/NASA Symposium on Recent Advances in Multidisciplinary Analysis and Optimizatio.

38. *Fully Integrated Aerodynamic/Dynamic Optimization of Helicopter Rotor Blades.* **Walsh, Joanne L., LaMarsh II, William J. and Sdelman, Howard M.** Dallas, Texas : s.n., 1992. Presented at 33rd AIAA/ASME/ASCE/AHS/ASC Structures, Structural Dynamics & Materials Conference.

39. *CONMIN - A Fortrain Program for Constrained Function Minimization. User's Manual.* **Vanderplaats, G. N.** 1973, NASA TMX-62282.

40. *Parallel Genetic Algorithm Implementation in Multidisciplinary Rotor Blade Design.* **Lee, J. and Hajela, P.** 1996, Journal of Aircraft, pp. 962-969.

41. *Aerodynamic Shape Design for Rotor Airfoils via Genetic Algorithm.* **Fanjoy, D. W. and Crossley, W. A.** 3, 1998, Journal of the American Helicopter Society, Vol. 43, pp. 263-270.

42. *Particle Swarm Optimization.* **Kennedy, J. and Eberhart, R. C.** Perth, Australia : s.n., Proceedings of the 1995 IEEE International Conference on Neural Networks. Vol. IV, pp. 1942-1948.

43. **Eberhart, R. C. and Shi, Y.** *Comparison Between genetic algorithms and particle swarm optimization.* [ed.] W. Potor, et al., et al. Berlin : Springer, 1998. pp. 611-616.

44. *A modified particle swarm optimizer.* **Shi, Y. and Eberhart, R. C.** Anchorage : Proceedings of the 1998 IEEE International Conference on Evolutionary Computation, 1998a.

45. **Shi, Y. and Eberhart, R. C.** Parameter selection in particle swarm optimization. *Lecture Notes in Computer Science.* London : Springer, 1998b.

46. **Parsopoulos, Konstantinos E. and Vrahatis, Michael N.** *Particle Swarm Optimization and Intelligence: Advances and Applications.* Hershey, PA : Information Science Reference, 2010. 978-1-61520-666-7.

47. *Self-Adaptive Penalties for GA-based Optimization.* **Coello, C. and Coello, A.** Washington DC : Proceedings of the 1999 IEEE Congress on Evolutionary Computation (CEC'99), 1999.

48. *Evaluation of Multidisciplinary Optimization Approaches for Aircraft Conceptual Design.* **Perez, R. E., Liu, H. H. T. and Behdinan, K.** Albany, New York : Proceedings Tenth AIAA/ISSMO Symposium On Multidisciplinary Analysis and Optimization, 2004. AIAA Paper 2004-4537.

49. *Effect of Twist on Helicopter Performance and Vibratory Loads.* **Keys, C., Tarzanin, F. and McHugh, F.** Arles, France : 13th European Rotorcraft Forum, 1987.

50. *Integrated Aerodynamic/Dynamic Optimization of Helicopter Rotors.* **Chattopadhyay, Aditi, Walsh, Joanne L. and Riley, Michael F.** Mobile, Alabama : Proc. AIAA/ASME/ASCE/AHS 30th Structures, Structural Dynamics and Materials Conference, 1989.

51. *An Enhanced Integrated Aerodynamic Load/Dynamic Optimization Procedure for Helicopter Rotor Blades.* **Chattopadhyay, Aditi and Chiu, Y. D.** s.l. : NASA CR-4326, 1990.

52. *Wind-Tunnel Evaluation of the Effect of Blade Nonstructural Mass Distribution on Helicopter Fixed-System Loads.* **Wilbur, Matthew L., et al., et al.** s.l. : NASA/TM-1998-206281, 1998.

53. *A collection of test problems for constrained global optimization algorithms.* **Floudas, C A and Paradalos, P. M.** Berlin, Germany : Springer, 1990.

Appendix

A.1.Sample Constrained Optimization UPSO vs. GA

This section will present the results for a simple constrained optimization from both USPO and GA algorithms. The function (53)to be minimized is:

$$f(x) = (x_1 - 10)^3 + (x_2 - 20)^3 \quad \text{A.1.}$$

With the following inequality nonlinear constraints:

$$100 - (x_1 - 5)^2 - (x_2 - 5)^2 \leq 0, (x_1 - 6)^2 + (x_2 - 5)^2 - 82.81 \leq 0 \quad \text{A.2.}$$

The side constraints on the design variables were:

$$13 < x_1 < 100, 0 < x_2 < 100 \quad \text{A.3.}$$

The current example is an excellent test for constrained optimization due to its very large design space. The global minimum is -6961with x_1=14.095 and x_2=0.84365. Note the upper bound is extremely high. The results of the two optimization routines are listed in Table 10.

Table 10 - Comparison of results for UPSO and GA

Algorithm	Size	Success Rate %	Mean Iteration	Iteration Standard Deviation	Mean Function Evaluations	Function Evaluations Standard Deviation	Success Tolerance
UPSO	200	99.5	146	18.85	29398	3796	1e-3
GA	200	91.5	96.05	38.8	19410.05	7675.51	10

Each algorithm was run 200 times with different random initial populations. For both the GA and UPSO a population size of 200 was used. The UPSO required the most number of iterations and

function evaluations. However it had the highest success rate with the lowest success tolerance. The GA has a success tolerance of 10 because with a tolerance equal of 1e-3, it was found that the GA had a difficult time matching the success condition. It is because of this, the UPSO algorithm can be considered the better choice. For a GA the population evolves to an optimum solution using crossover and recombination of the design variables. It is limited by the diversity of the initial population. With such a large side constraint on the design variables, the initial range of the problem provided too much diversity to the problem. For the UPSO a large diversity allows for more exploration of the design space, thus allowing the particles to find the best solution. The main disadvantage of the UPSO is the number of function evaluations. For design problems with discipline codes that are computationally intensive, this could be a time consuming algorithm.

A.2. Validation Extras

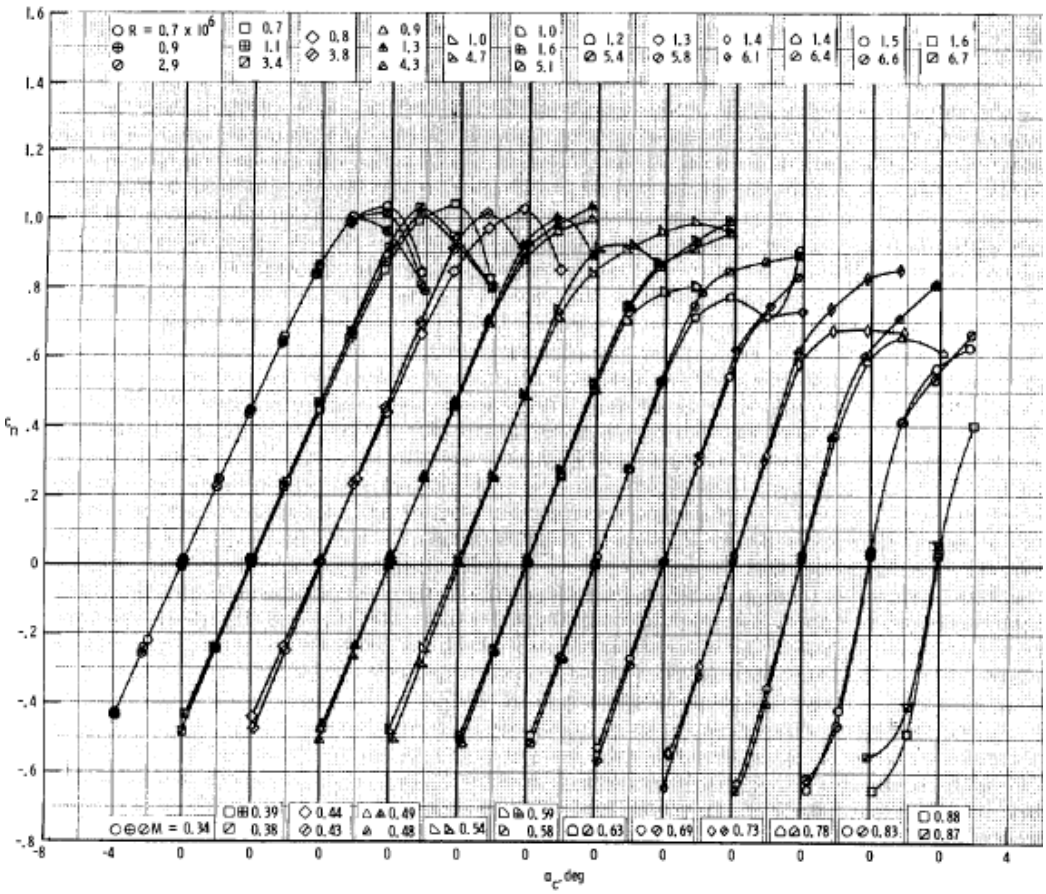

Figure 72 - Lift Curves for several Mach numbers (19)

Table 11 - Rotor Blade structural properties (52)

Radial station, r/R	Mass, slugs/ft	Stiffness, lb-ft^2 for—			Torsional inertia, lb-sec^2
		Flap	Chord	Torsion	
0.1222	0.0280	329.9	7000.0	267.4	0.000242
0.14	0.0280	329.9	7000.0	267.4	0.000242
0.16	0.0280	329.9	6250.0	267.4	0.000242
0.18	0.0280	329.9	6250.0	267.4	0.000251
0.20	0.0280	305.5	6250.0	267.4	0.000251
0.22	0.0278	284.7	6250.0	267.4	0.000275
0.24	0.0272	270.8	6250.0	267.4	0.000331
0.26	0.0272	243.1	6250.0	267.4	0.000359
0.28	0.0272	243.1	6250.0	267.4	0.000359
0.30	0.0236	243.1	6250.0	256.9	0.000359
↓	↓	↓	↓	↓	↓
0.48	0.0236	243.1	6250.0	256.9	0.000359
0.50	0.0236	250.0	6250.0	229.2	0.000359
↓	↓	↓	↓	↓	↓
0.54	0.0236	250.0	6250.0	229.2	0.000359
0.56	0.0240	250.0	6250.0	229.2	0.000359
0.58	0.0240	262.5	6250.0	229.2	0.000359
0.60	0.0240	270.8	6250.0	243.0	0.000359
0.62	0.0240	281.3	6250.0	256.9	0.000359
0.64	0.0240	281.3	6250.0	263.9	0.000359
0.66	0.0246	277.8	6250.0	263.9	0.000359
0.68	0.0259	269.1	6250.0	263.9	0.000359
0.70	0.0312	269.1	6250.0	263.9	0.000359
0.72	0.0312	269.1	6250.0	253.5	0.000359
0.74	0.0312	244.8	6250.0	256.9	0.000359
0.76	0.0312	217.0	6250.0	277.8	0.000359
0.78	0.0304	208.3	6250.0	281.3	0.000359
0.80	0.0291	208.3	6250.0	253.5	0.000359
0.82	0.0282	208.3	5555.5	225.7	0.000359
0.84	0.0268	187.5	4650.0	180.6	0.000359
0.86	0.0271	154.5	3470.0	156.3	0.000359
0.88	0.0209	125.0	2290.0	111.1	0.000359
0.90	0.0200	69.4	1944.0	83.3	0.000349
0.92	0.0191	52.1	1389.0	62.5	0.000328
0.94	0.0140	31.9	900.0	48.6	0.000290
0.96	0.0115	20.8	590.0	34.7	0.000200
0.98	0.0099	13.9	382.0	20.8	0.000099
1.00	0.0092	13.2	278.0	13.9	0.000053

(52)

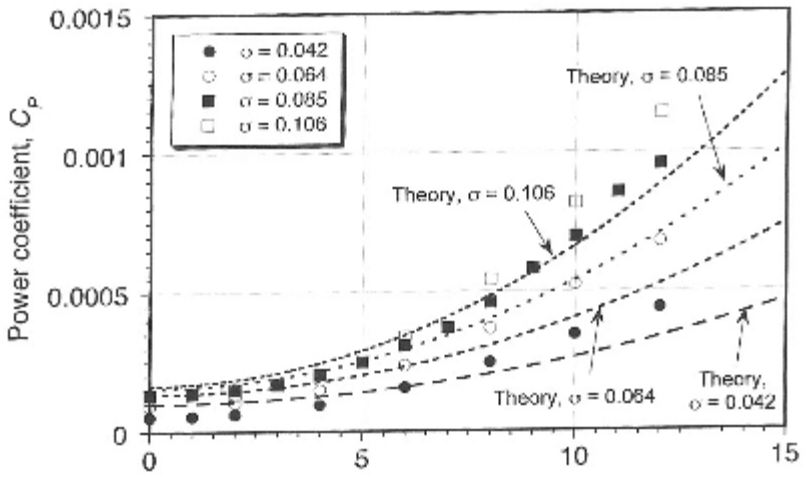

Figure 73 - Power coefficient in hover vs. collective pitch angle for different solidities (1), data source (2)

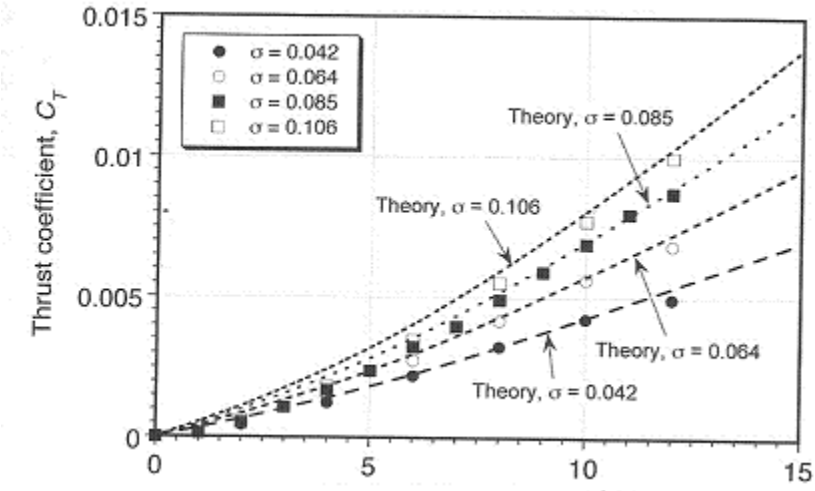

Figure 74 - Thrust coefficient in hover vs. collective pitch angle for different solidities (1), data source (2)

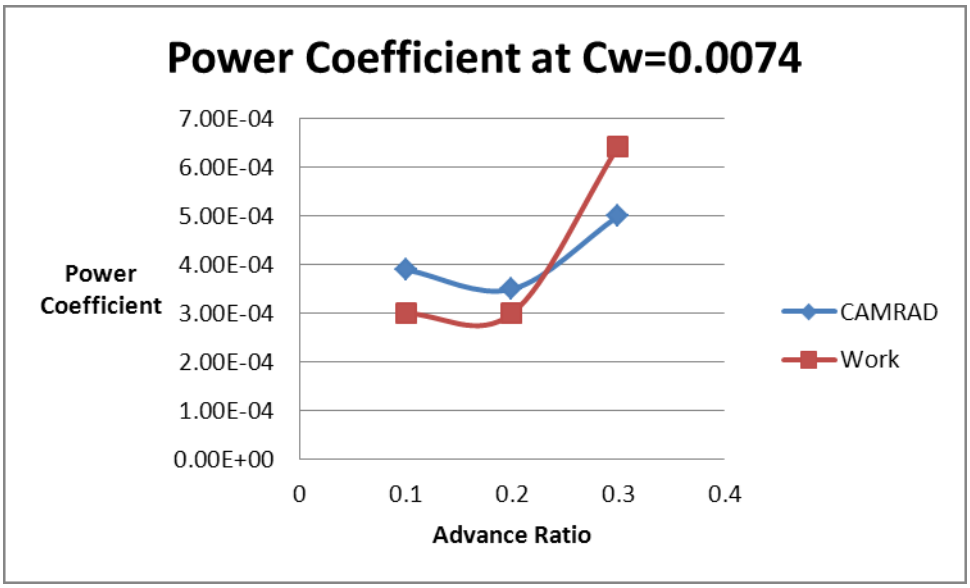

Figure 75 - Power coefficient for low-medium trust at different advance ratios

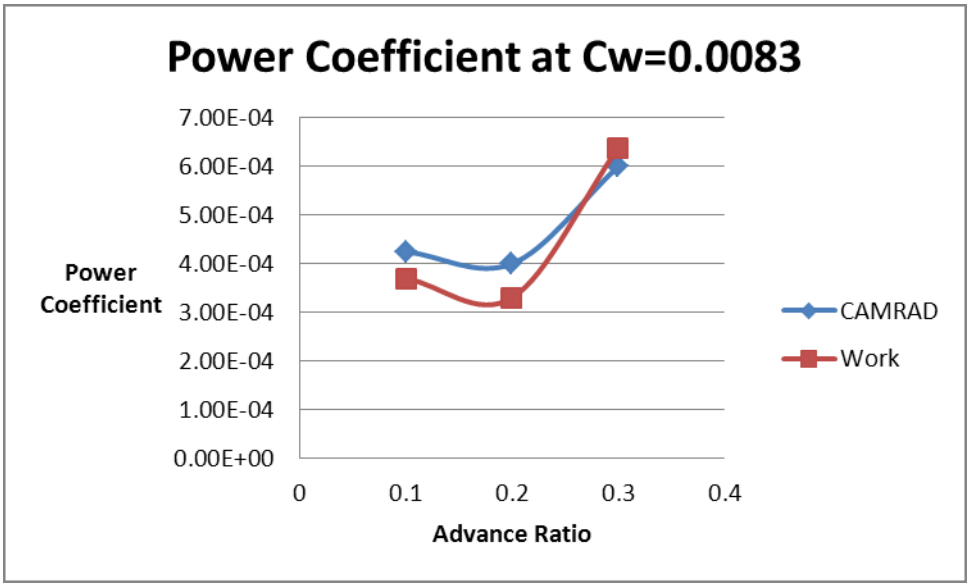

Figure 76 - Power coefficient for medium thrust at different advance ratios

A.3.SQP-Case 1

Table 12 – Optimized design variables for structural optimization

Number	Horizontal Wall Thickness									
1	0.0062	0.0056	0.0033	0.0087	0.0021	0.0039	0.0149	0.0027	0.0059	0.025
2	0.0062	0.0056	0.0038	0.0023	0.0054	0.0044	0.0126	0.0023	0.0055	0.025
3	0.0062	0.0056	0.0038	0.0038	0.0054	0.005	0.0195	0.0032	0.0024	0.025
4	0.0062	0.0056	0.0053	0.01	0.0036	0.0031	0.018	0.0026	0.0076	0.025
5	0.0062	0.0056	0.006	0.0097	0.0054	0.0051	0.018	0.0033	0.0023	0.025
	Vertical Wall Thickness									
1	0.0054	0.0048	0.0073	0.003	0.0084	0.0043	0.0164	0.0034	0.0085	0.02
2	0.0054	0.0048	0.0064	0.0185	0.002	0.0034	0.0194	0.004	0.006	0.02
3	0.0054	0.0048	0.0064	0.0126	0.002	0.0022	0.0026	0.0023	0.0165	0.02
4	0.0054	0.0048	0.0035	0.0027	0.0055	0.0059	0.0097	0.0036	0.0046	0.02
5	0.0054	0.0048	0.0021	0.002	0.002	0.002	0.002	0.0021	0.0133	0.02
	NSM									
1	0	0	0	1.4919	0	0	0.4912	0	0.7715	3
2	0	0	0	0.3635	0	0	0.9798	0	1.762	3
3	0	0	0	1.5812	0	0	0.6003	0	0.1477	3
4	0	0	0	0.7538	0	0	0.1567	0	0.8875	3
5	0	0	0	1.1387	0	0	1.6995	0	1.2549	3

Table 13 - SQP frequency constraints (Bold Italic are active)

Number	Lower 1st Flap Bound	Upper 1st Flap Bound	Lower 2nd Flap Bound	Upper 2nd Flap Bound
1	-0.2727	***-1.76946E-07***	-0.119047714	***8.46892E-08***
2	-0.2727	***5.55745E-08***	-0.119047678	***5.27641E-08***
3	-0.2727	***1.64833E-07***	-0.119047648	***2.62294E-08***
4	-0.2727	***-3.47122E-12***	-0.119047619	***8.39377E-11***
5	-0.2727	***-7.93025E-09***	-0.119047605	***-1.23231E-08***

Table 14 - SQP stress and autorotation constraints

Segment	1	2	3	4	5	6	7	8	9	10
Number	Centrifugal Stress									
1	-0.1852	-0.0977	***9E-07***	-0.3248	***-9E-06***	***-1E-05***	-0.7198	***-1E-05***	-0.5851	-0.8922

2	-0.1852	-0.0977	***2E-07***	-0.4205	***-4E-07***	***-9E-07***	-0.7096	***-3E-06***	-0.5126	-0.8922
3	-0.1852	-0.0977	***6E-07***	-0.3159	***8E-07***	***7E-07***	-0.7176	***-2E-05***	-0.6206	-0.8922
4	-0.1852	-0.0977	***1E-09***	-0.3906	***-2E-09***	***-8E-09***	-0.7263	***-2E-08***	-0.5777	-0.8922
5	-0.1852	-0.0977	***-3E-07***	-0.358	***1E-09***	***1E-09***	-0.6932	***-2E-08***	-0.5526	-0.8922
	Bending Stress									
1	***2E-10***	***2E-12***	-0.0548	-0.4773	-0.3581	-0.589	-0.9046	-0.8201	-0.9698	
2	***2E-11***	***2E-11***	-0.0766	-0.4525	-0.4209	-0.5903	-0.9017	-0.8167	-0.9656	
3	***3E-11***	***7E-10***	-0.0756	-0.4357	-0.4214	-0.5849	-0.8995	-0.8214	-0.9668	
4	***3E-11***	***8E-12***	-0.0955	-0.516	-0.4222	-0.5765	-0.905	-0.8191	-0.9696	
5	***6E-09***	***3E-08***	-0.0774	-0.4894	-0.4209	-0.5831	-0.8935	-0.821	-0.9625	

Number	**AI**
1	***-1E-06***
2	***-3E-07***
3	***-9E-07***
4	***-1E-09***
5	***-4E-09***

A.4.Case2 Extras

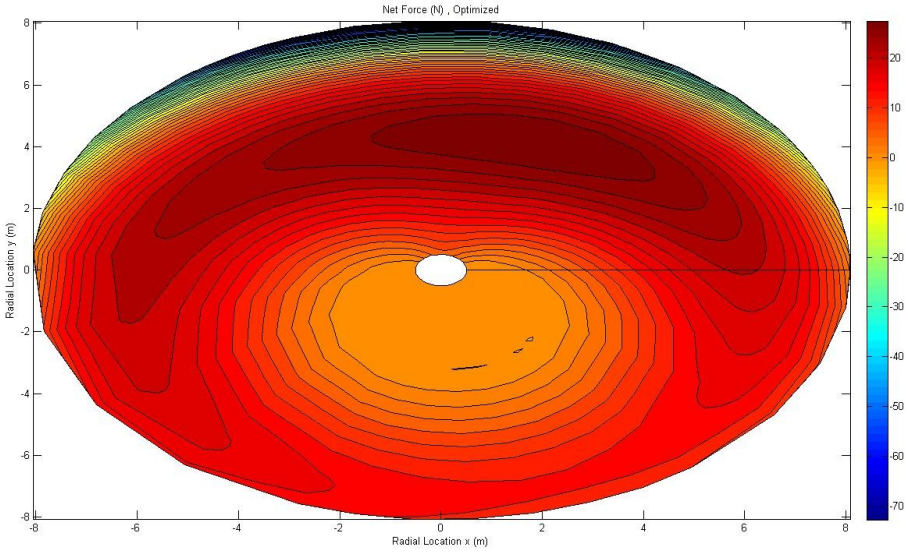

Figure 77 - Net force between aerodynamic and inertial loads for optimized blade

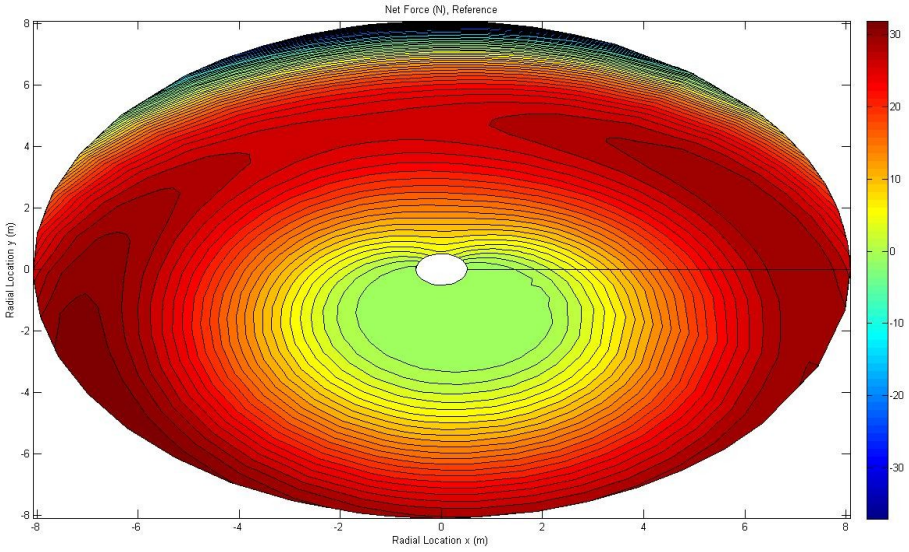

Figure 78 - Net force between aerodynamic and inertial loads for reference blade

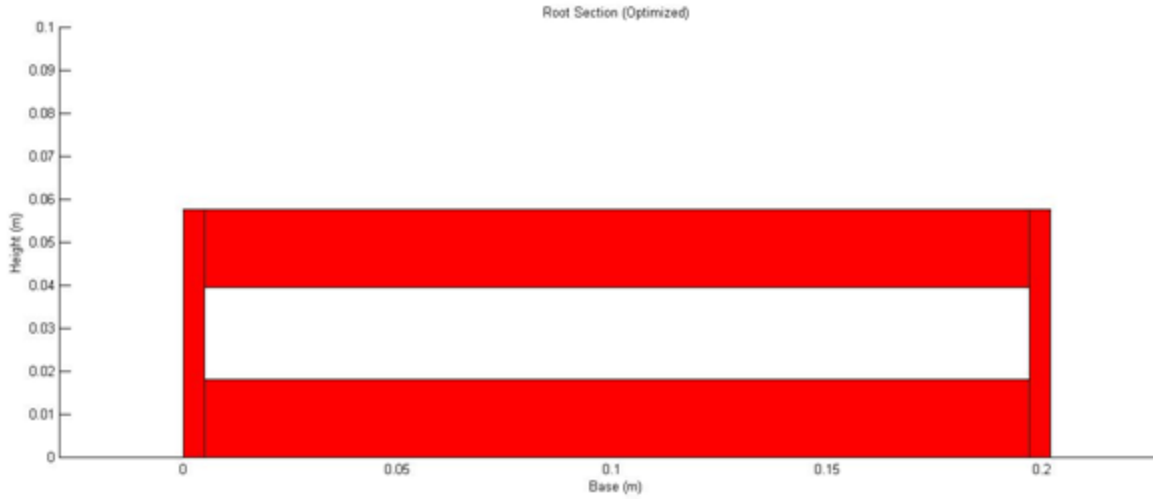

Figure 79 - Root cross section (optimized)

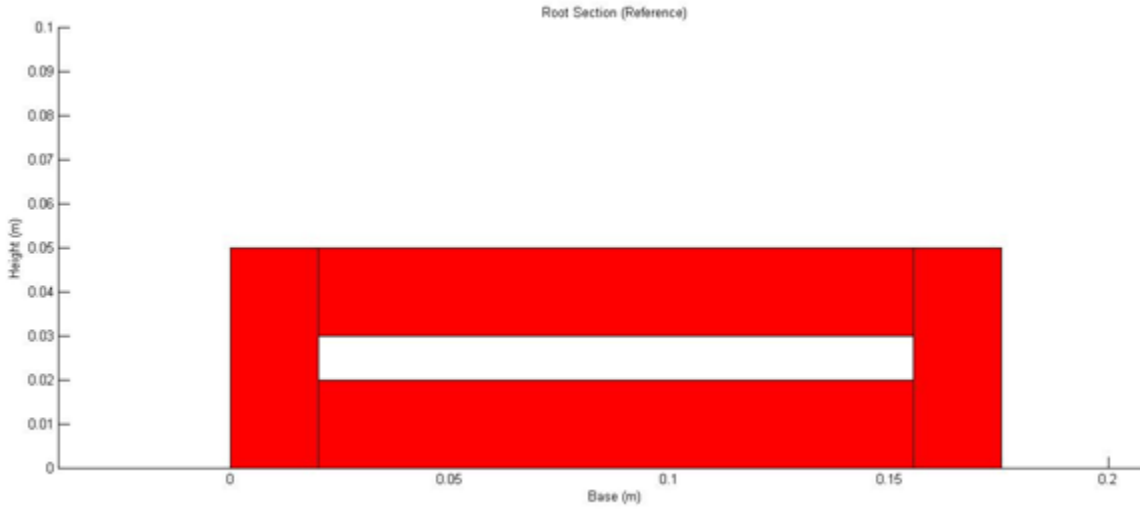

Figure 80 - Root cross section (Reference)

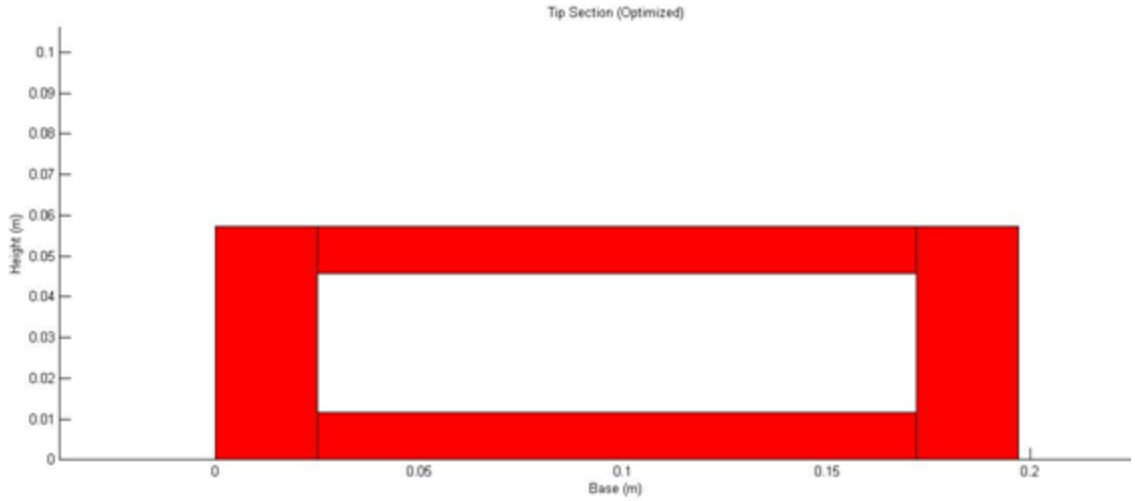

Figure 81 - Tip section (Optimized)

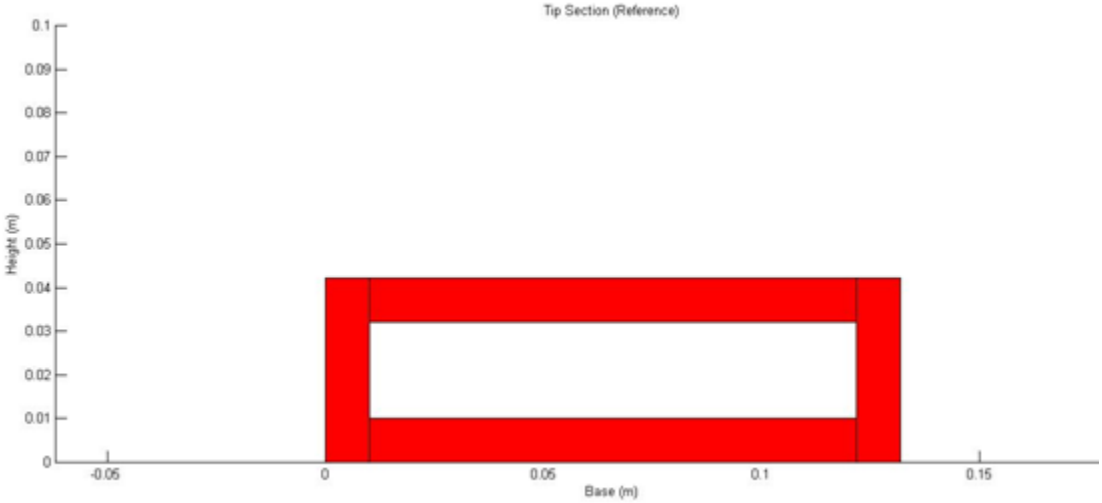

Figure 82 - Tip section (Reference)